Synthesis and Biological Applications of Phosphorescent Ir(III) Complex-Based Probes with Arginine Peptide

Mami YASUKAGAWA

Gunma University

2021

Acknowledgments

I would like to express my sincere gratitude to **Associate Professor Toshitada Yoshihara** for his insightful direction, valuable suggestions and discussions throughout this study. I wish to thank **Professor Seiji Tobita** for his valuable advice and discussions.

I am also sincerely grateful to **Professor Motoko Asano**, **Professor Masashi Sonoyama**, **Professor Masafumi Unno**, and **Associate Professor Tomohisa Moriguchi** for their valuable comments and kind advice on this thesis.

I would like to express my graduate to **Associate Professor Keiichi Yamada** for his valuable discussion for the peptide synthesis. I would like to express my thanks to **Dr. Shuichi Shiozaki** for his medical expertise and guidance for animal experiments.

I would like to thank all laboratory members for a precious time spent together in the laboratory.

Finally, I would like to express my deep gratitude to my family for their encouragement and support all through my studies.

Mami Yasukagawa

Contents

Chapter 1

General Introduction

1-1 Fluorescence and phosphorescence for biological applications

Detection and imaging of biological species using luminescent molecules have become an important technology for biological and medical research [1,2]. Many chemical and biochemical analytes can be detected by optical sensing: ions (K^+, Ca^{2+}, halide ions, phosphates), neutral molecules (glucose, lipid), gases (O_2, CO_2, NO), and biological macromolecules (DNA, protein). The development of fluorescent Ca^{2+} probes was pioneered by Roger Tsien and coworkers in the early 1980s [3,4]. The fluorescent Ca^{2+} probe Fluo-3 consists of a fluorescein unit and the ionophore moiety, and display significant fluorescence enhancement upon binding Ca^{2+} (Figure 1-1). Thus, the change of intracellular Ca^{2+} levels can be detected and imaged by measuring the fluorescence intensity of the probes. Although the cell-penetration ability of Fluo-3 is very low due to the carboxylic moieties, loading can be achieved by modification of acetoxymethyl ester units. When the modified Fluo-3 is taken up into the cell, the ester bonds are cleaved by a non-specific esterase, and the produced Fluo-3 is effectively accumulated in the cell.

During the past several decades numerous fluorescent probes have been designed and synthesized based on fluorescent organic compounds, for example, coumarin, fluorescein, rhodamine, BODIPY, and cyanine. Combining fluorescent probes with microscopy techniques enabled the visualization of the localization and quantity of analytes in living cells and tissues. In recent years, optical probes have been increasingly applied for *in vivo* imaging because the near-infrared emissive compounds or a two-photon microscope enable imaging in deep tissues. Thus, bioimaging technology has been progressed with the development of both probe molecules and optical microscopy techniques. These intracellular and *in vivo* imaging probes have been based on fluorescent molecules

because organic compounds typically exhibit fluorescence, which occurs from the lowest excited singlet (S_1) state (Figure 1-2).

In contrast, the emission from the lowest excited triplet (T_1) states (Figure 1-2), called phosphorescence, has attracted attention for bioimaging and sensing. Phosphorescence has a large Stokes shift relative to fluorescence, which is defined as the wavelength difference between absorption and emission peak. This feature is advantageous because the excitation light can be easily removed using a filter when observing a fluorescence microscopic image. Moreover, phosphorescence lifetime (μs–s) is usually much longer than fluorescence lifetimes (ns) because phosphorescence is a spin-forbidden emission. The longer lifetime is therefore an advantage for intracellular and *in vivo* imaging, which allows discrimination from autofluorescence derived from cells or tissues. Since the lifetime of autofluorescence is very short (typically less than 10 ns), only the phosphorescence signal from the probes can be easily detected by using a pulsed excitation light source and a time-gated measurement system. In addition, phosphorescence is easily quenched by molecular oxygen (O_2) because energy transfer reaction from triplet excited molecule to ground state oxygen ($^3\Sigma_g^-$) occurs efficiently through bimolecular collisions (Figure 1-2). The use of phosphorescence quenching phenomenon is extremely effective in the detection and imaging of O_2 levels in living cells and tissues.

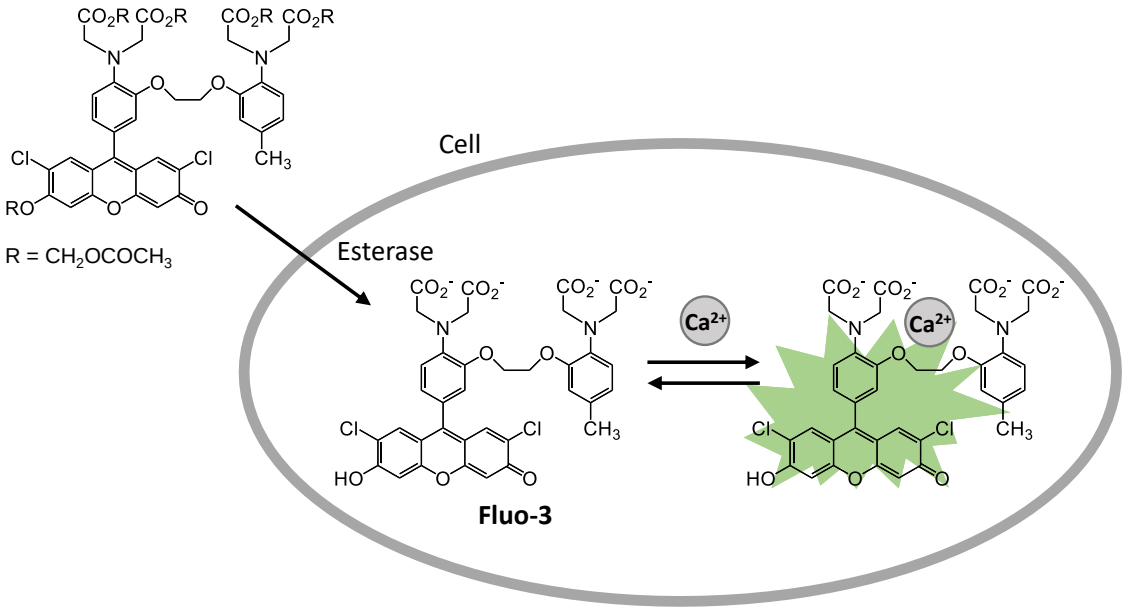

Figure 1-1. Illustration of the intracellular Ca^{2+} sensing by Fluo-3.

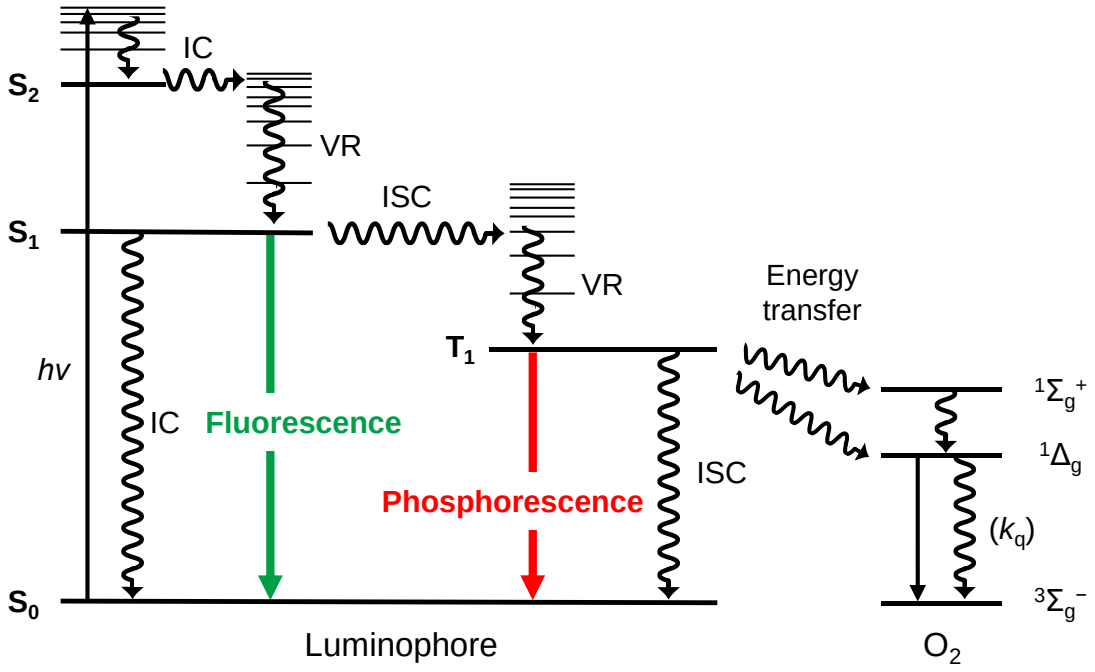

S_1 and S_0: the lowest excited singlet state and ground state

T_1: the lowest excited triplet state

IC: internal conversion, ISC: intersystem crossing

VR: Vibrational relaxation

Figure 1-2. Jablonski diagram for generic luminophore involving phosphorescence quenching by molecular oxygen.

1-2 O_2 probes based on phosphorescence molecules

In recent years, various phosphorescent probe molecules have been developed for the measurement of O_2 levels in living cells and tissues [5–7]. One of the properties required for the phosphorescent probe is to provide a strong phosphorescence at room temperature. It is known that the heavy-metal complexes such as Ru(II) complexes, Pt(II)- and Pd(II)-porphyrins, and Ir(III) complexes emit a strong room-temperature phosphorescence under the absence of oxygen because of accelerated spin-forbidden transition by the spin-orbit coupling associated with central heavy-metal ion.

Ru(II) complexes have been widely used for intracellular O_2 sensing because their cell permeability is relatively high [8–10]. However, the oxygen response of these complexes is low due to their short emission lifetime (< 1 μs). Pt(II)- and Pd(II)-porphyrins display significantly longer phosphorescence lifetimes (50 ~ 1000 μs). However, their cell permeability is low due to their high lipophilicity. Therefore, various chemical modifications have been made to increase the cellular uptake efficiency of these porphyrins. Papkovsky and coworkers have designed and synthesized intracellular O_2 probes based on Pt(II)-coproporphyrin conjugated with cell-penetrating peptides such as the transactivator of transcription (TAT) peptide or oligoarginine derivatives, which are known to facilitate penetration into cells across a membrane (Figure 1-3) [11]. The conjugates of perfluorophenyl-substituted Pt(II)-porphyrin PtTFPP with monosaccharide substituents such as glucose and galactose were recently developed for intracellular O_2 imaging in three-dimensional tissue models (Figure 1-3) [12]. Moreover, Evans and coworkers developed a click-assembled oxygen sensing nanoconjugate, in which in which dendritic Pd(II)-benzoporphyrin probe was decorated with ploy(amidoamine) units, giving it with a cationic character at physiological pH conditions [13].

Recently, Ir(III) complexes used as a phosphorescent material for organic light emitting diodes (OLEDs) have been attracting attention as optical probes for visualizing the O_2 levels in living cells and tissues. Red phosphorescent Ir(III) complex BTP (Figure 1-4) was applied to sense O_2 levels in living cells and hypoxic tumor [14]. The advantage of Ir(III) complexes is that the photophysical properties (absorption and emission wavelengths) and intracellular localization can be easily controlled by chemical modification of the ligands. For example, BTPDM1 (Figure 1-4), which has significantly high cellular uptake efficiently compared with BTP, was synthesized by introduction of a cationic dimethylamino group into the acetylacetonato ligand of BTP [15]. Another notable point is that Ir(III) complexes have moderately long phosphorescence lifetime (1 ~ 20 μs), which is effective for sensing the O_2 levels in living cells and tissues.

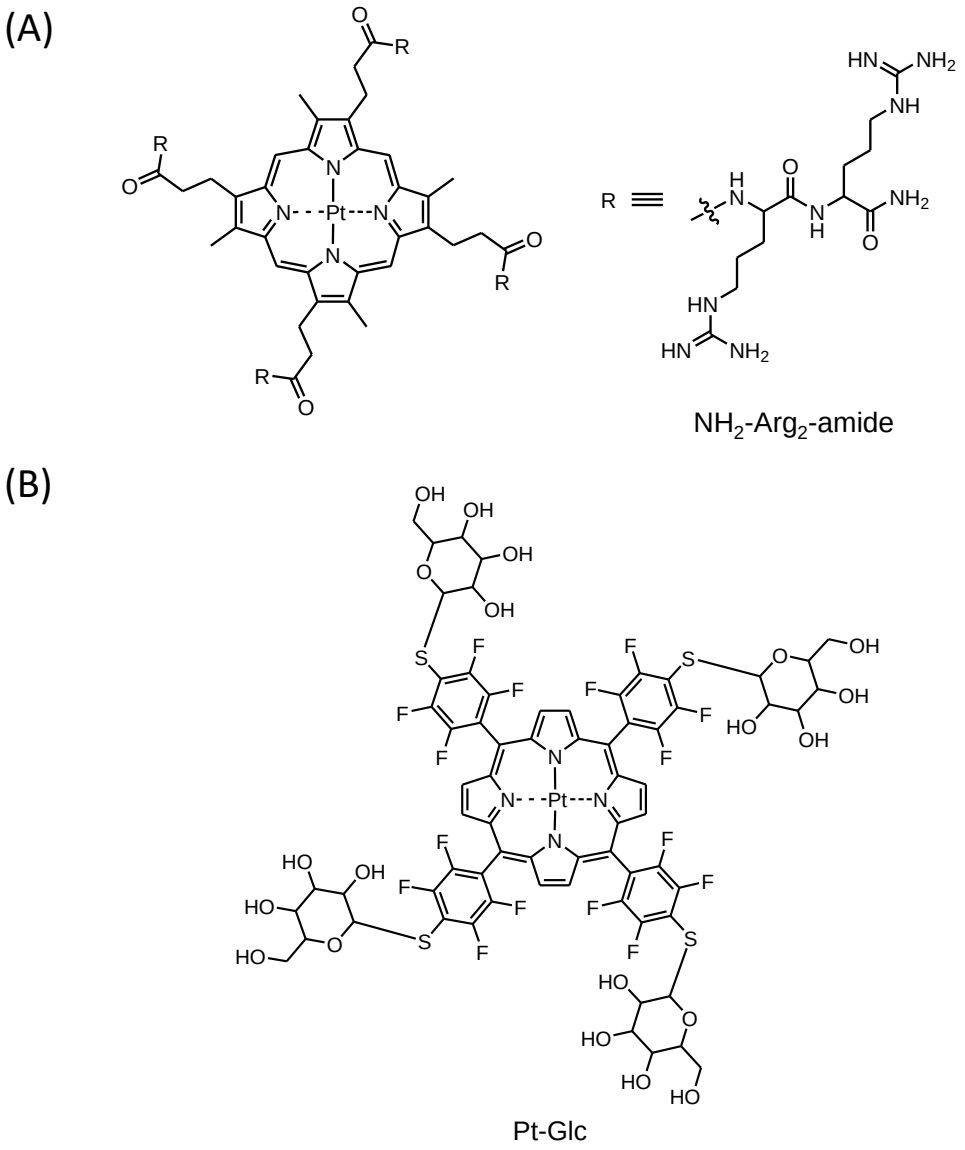

Figure 1-3. Chemical structures of Pt(II)-porphyrins conjugated with oligoarginine (A) and glucose (B).

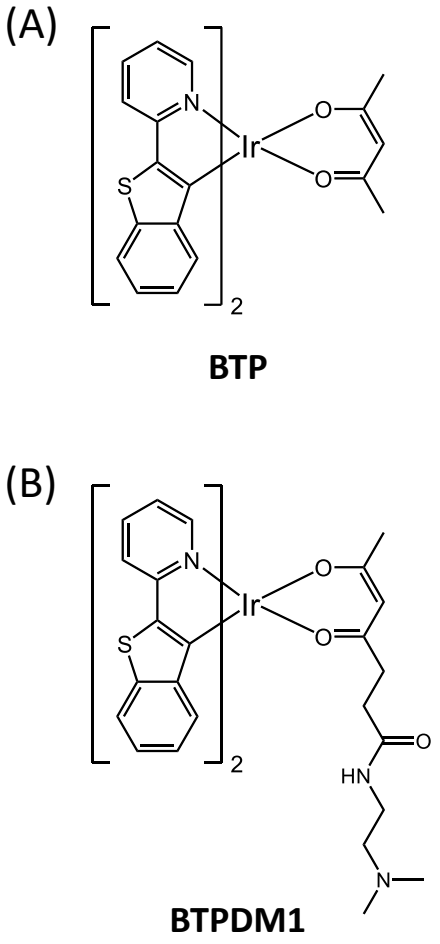

Figure 1-4. Chemical structures of BTP (A) and BTPDM1 (B).

1-3 Ratiometric O_2 probes

The oxygen measurement using a phosphorescent probe is usually performed by measuring the emission intensity or emission lifetime, which changes depending on the O_2 concentration. However, the emission intensity is an ambiguous parameter, which depends on many factors, including the intensity of the excitation light, sensitivity of the detector, and the concentration of probe molecules in cells. In contrast, emission lifetime measurement enables quantitative oxygen sensing but requires a special instrument including a pulsed light source and a time-resolved detection system.

As alternative, the ratiometric method enables quantitative O_2 measurements without special equipment. The ratiometric O_2 probe consists of an oxygen-sensitive phosphor and an oxygen-insensitive fluorophore. The ratiometric measurement is performed by using the emission ratio (R_I) between phosphorescence intensity (I_p) and fluorescence intensity (I_f). Figure 1-5 illustrates the principle of ratiometric O_2 measurements. When the fluorescence quenching by molecular oxygen is negligibly small, the relation between R_I and oxygen partial pressure (pO_2) can be derived based on the Stern-Volmer equation:

$$\frac{R_I^0}{R_I} = \frac{I_p^0/I_f^0}{I_p/I_f} = 1 + K_{SV}\, pO_2 \qquad (1\text{-}1)$$

where R_I^0 (= I_p^0/I_f^0) is the ratio in the absence of oxygen, and K_{sv} is the Stern-Volmer constant. By using the K_{sv} value, ratiometric measurements allow the estimation of the oxygen partial pressure.

Kopelman's group reported the first nanoparticle-based ratiometric O_2 probe (Figure 1-6A), in which Oregon Green 488-dextran and Ru(II) complex were encapsulated in

silica particle with polyethylene glycol layer [16]. These nanoparticles need to be introduced into cells using a gene gun infection due to their low cellular permeability.

Papkovsky and coworkers developed MitoImage-MM2 probe, consisting of Pt(II)-porphyrin and fluorescent polymer poly(9,9-dioctylfluorene) embedded in a cationic polymer [17]. The dual emissions of MM2 probe were measured after cultured cells were incubated with the probes for 16 h. Although three-dimensional oxygen images showed a hypoxic core in the spheroids stained with MM2 by using a two-photon microscope, the distribution of MM2 in the spheroids was not uniform. The same group further designed nanoparticle probes that consist of a polyfluorene with covalently bound Pt(II)-porphyrin, and grafted with charged groups for improving cell permeability [18]. The advantages of nanoparticle-based probes are high brightness and photochemical stability. However, these probes need a relatively long incubation time because of low cellular uptake.

On the other hand, small-molecule probes in which a fluorophore and phosphor are connected with a peptide linker have been developed (Figure 1-6B) [19,20]. This type of probes has the advantages of affinity to living cells. Moreover, chemical modification of the linker can be easily performed to control water solubility, cellular uptake efficiency, and subcellular localization.

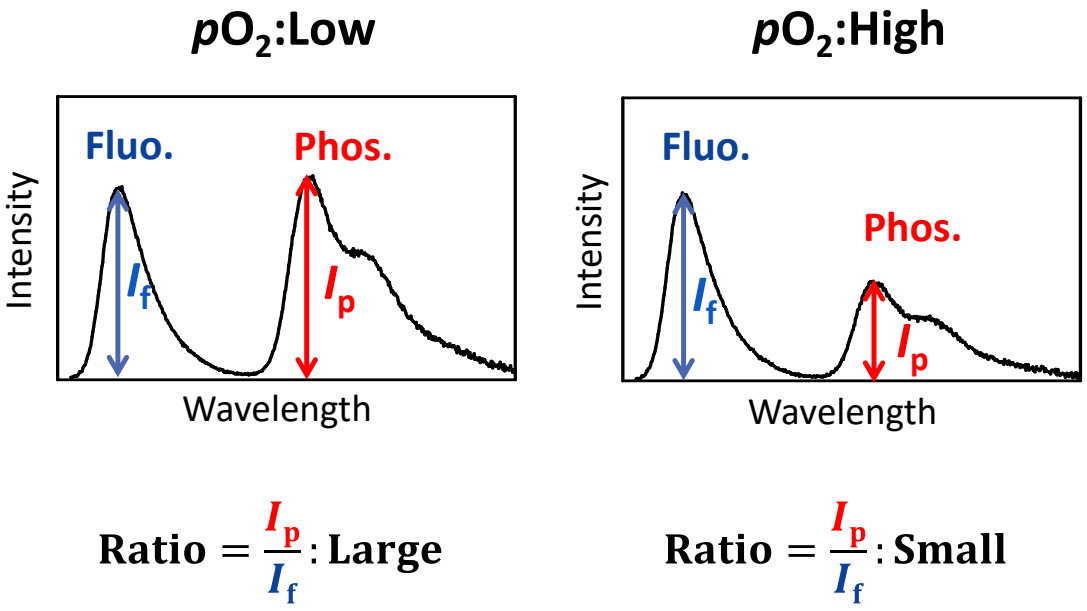

Figure 1-5. Principle of ratiometric O_2 measurements.

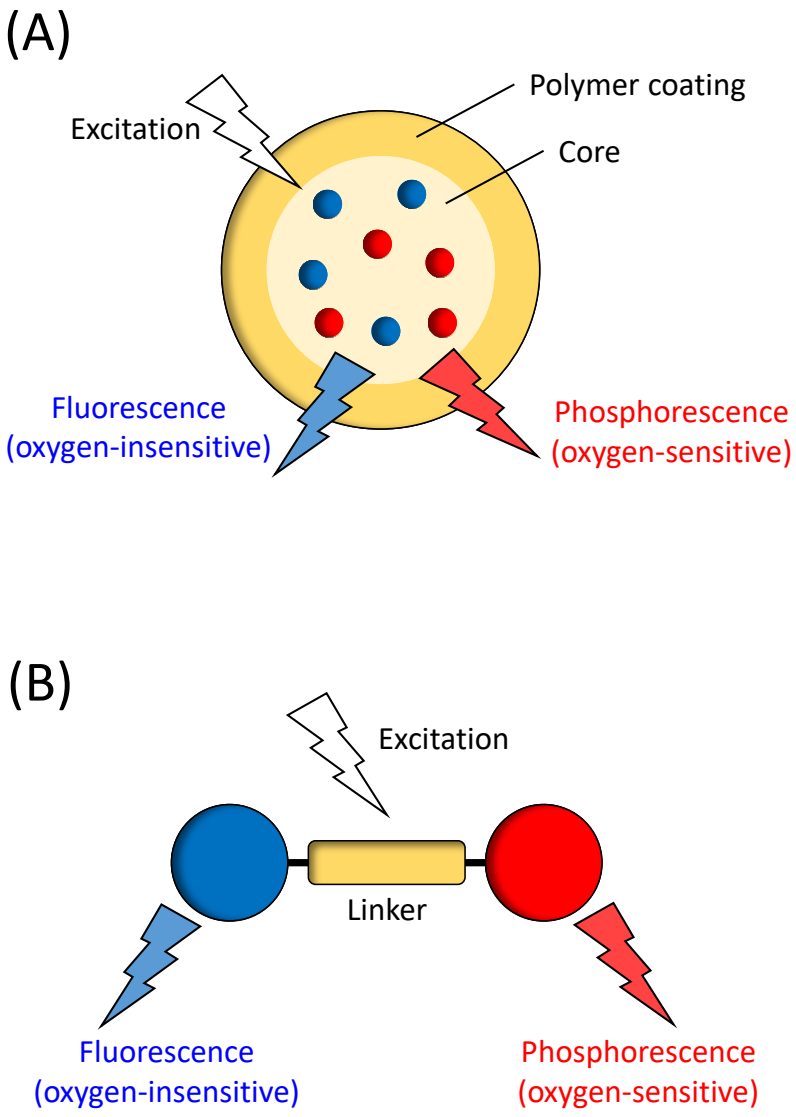

Figure 1-6. Design concept of two different types of ratiometric O_2 probes: nanoparticle-based probe (A) and small-molecule-based probe (B).

1-4 *In vivo* imaging using phosphorescent probes

Phosphorescence probes present advantages such as large stokes shift, long luminescent lifetime and thus the application of phosphorescence imaging has been extended for *in vivo* imaging. Since the oxygen supply from blood and cellular utilization have an important role in maintaining tissue functions, there is a need to develop both intracellular and extracellular (intravascular) probes. Moreover, disruption of the vascular system is closely associated with various diseases such as cancer, diabetic retinopathy. Therefore, imaging the vascular structures is extremely important for assessing pathological conditions.

Vinogradov and coworkers have designed and synthesized dendric phosphorescent probes Oxyphor R4 and G4, in which Pd(II)-porphyrin was encapsulated into second generation poly(aryglycine) dendrons coated with polyethylene glycol, to image intravascular O_2 levels [21]. These probes have polyethylene glycol (PEG) layer, which significantly improves water solubility and prevents aggregation and interaction with serum albumin in the blood. Recently, the hydrophilic Ir(III) complexes derivatized with PEG chains were synthesized [22]. Oxygen levels of the peritubular capillaries were measured using these complexes and a confocal microscope equipped with the lifetime measurement system. However, these probes that circulate in bloodstream are not suitable for long-term imaging. In case of longer observation, vascular imaging probes that paint blood vessel walls are required. It is found that Ir(III) complex incorporating oligoarginine peptides administered intravenously to mice selectively stain the vascular endothelium cells. Arginine-rich peptide is widely used as a cell-penetrating peptide [23], but its behavior in small animals has not been elucidated in detail. Thus, it is necessary to examine the usefulness of the Ir(III) complex for *in vivo* vascular imaging.

1-5 Purpose of this study

Phosphorescence-based probes have been developed as powerful tools for investigating the real-time behavior of biological analytes, especially oxygen, in living cells and animals. Depending on the ligand modification, phosphorescent metal complexes show different localization, which allows intracellular or intravascular imaging. In this study, phosphorescent Ir(III) complexes with cell-penetrating peptides were applied to intracellular oxygen probes and *in vivo* imaging probes.

Aiming to improve cellular uptake of the probe, the ratiometric O_2 probes with a cell-penetrating peptide were designed and synthesized. Their spectral and photophysical properties in solutions and biological model membranes, and cellular uptake efficiency were investigated compared with reported ratiometric O_2 probe. Furthermore, the oxygen levels in cultured cells could be visualized by using these ratiometric O_2 probes and a fluorescence microscope.

The deep-red phosphorescent Ir(III) complexes conjugated with oligoarginine peptides were synthesized for *in vivo* vascular imaging. The usefulness of these complexes as *in vivo* vascular imaging probes was demonstrated by comparing them with FITC-tomato lectin, which is used as a vascular endothelial imaging reagent. In addition, the differences between vascular structures of a normal and pathological mouse could be imaged by using these complexes and a confocal fluorescence microscope.

References

[1] J. R. Lakowicz, *Principles of Fluorescence Spectroscopy*, THIRD EDITION Springer, New York, 2006.

[2] B. Valeur, *Molecular fluorescence*, SECOND EDITION, Wiley-VCH, 2012.

[3] R. Y. Tsien, *Biochemistry*, **1980**, *19*, 2396–2404.

[4] A. Minta, J. P. Y. Kao and R. Y. Tsien, *J. Biol. Chem.*, **1989**, *264*, 8171–8178.

[5] X. Wang and O. S. Wolfbeis, *Chem. Soc. Rev.*, **2014**, *43*, 3666–3761.

[6] R. I. Dmitriev and D. B. Papkovsky, *Methods Appl. Fluoresc.*, **2015**, *3*, 34001.

[7] T. Yoshihara, Y. Hirakawa, M. Hosaka, M. Nangaku and S. Tobita, *J. Photochem. Photobiol. C Photochem. Rev.*, **2017**, *30*, 71–95.

[8] H. Komatsu, K. Yoshihara, H. Yamada, Y. Kimura, A. Son, S. I. Nishimoto and K. Tanabe, *Chem. Eur. J.*, **2013**, *19*, 1971–1977.

[9] D. Hara, H. Komatsu, A. Son, S. I. Nishimoto and K. Tanabe, *Bioconjug. Chem.*, **2015**, *26*, 645–649.

[10] A. Son, A. Kawasaki, D. Hara, T. Ito and K. Tanabe, *Chem. Eur. J.*, **2015**, *21*, 2527–2536.

[11] R. I. Dmitriev, H. M. Ropiak, G. V. Ponomarev, D. V. Yashunsky and D. B. Papkovsky, *Bioconjug. Chem.*, **2011**, *22*, 2507–2518.

[12] R. I. Dmitriev, A. V. Kondrashina, K. Koren, I. Klimant, A. V. Zhdanov, J. M. P. Pakan, K. W. McDermott and D. B. Papkovsky, *Biomater. Sci.*, **2014**, *2*, 853–866.

[13] A. J. Nichols, E. Roussakis, O. J. Klein and C. L. Evans, *Angew. Chem. Int. Ed.*, **2014**, *53*, 3671–3674.

[14] S. Zhang, M. Hosaka, T. Yoshihara, K. Negishi, Y. Iida, S. Tobita and T. Takeuchi, *Cancer Res.*, **2010**, *70*, 4490–4498.

[15] T. Yoshihara, M. Hosaka, M. Terata, K. Ichikawa, S. Murayama, A. Tanaka, M. Mori, H. Itabashi, T. Takeuchi and S. Tobita, *Anal. Chem.*, **2015**, *87*, 2710–2717.

[16] Y. E. L. Koo, Y. Cao, R. Kopelman, S. M. Koo, M. Brasuel and M. A. Philbert, *Anal. Chem.*, **2004**, *76*, 2498–2505.

[17] A. V. Kondrashina, R. I. Dmitriev, S. M. Borisov, I. Klimant, I. O'Brien, Y. M. Nolan, A. V. Zhdanov and D. B. Papkovsky, *Adv. Funct. Mater.*, **2012**, *22*, 4931–4939.

[18] R. I. Dmitriev, S. M. Borisov, H. Düssmann, S. Sun, B. J. Müller, J. Prehn, V. P. Baklaushev, I. Klimant and D. B. Papkovsky, *ACS Nano*, **2015**, *9*, 5275–5288.

[19] T. Yoshihara, Y. Yamaguchi, M. Hosaka, T. Takeuchi and S. Tobita, *Angew. Chemie. Int. Ed.*, **2012**, *51*, 4148–4151.

[20] T. Yoshihara, S. Murayama and S. Tobita, *Sensors*, **2015**, *15*, 13503–13521.

[21] T. V. Esipova, A. Karagodov, J. Miller, D. F. Wilson, T. M. Busch and S. A. Vinogradov, *Anal. Chem.*, 2011, **83**, 8756–8765.

[22] T. Yoshihara, Y. Hirakawa, M. Nangaku and S. Tobita, Hydrophilic Ir(III) complexes for in vitro and in vivo oxygen imaging. In *RSC Detection Science: Quenched-Phosphorescence Detection of Molecular Oxygen: Applications in Life Sciences, Chap.4*, Royal Society of Chemistry, 2018, pp. 71–90.

[23] S. Futaki, T. Suzuki, W. Ohashi, T. Yagami, S. Tanaka, K. Ueda and Y. Sugiura, *J. Biol. Chem.*, **2001**, *276*, 5836–5840.

Chapter 2

Intracellular Ratiometric Oxygen Probes with Cell Penetrating Peptide

2-1 Introduction

Molecular oxygen plays important roles in various cell functions such as cellular differentiation, proliferation, and metabolism. To synthesize ATP, aerobic organisms use oxygen, the final electron acceptor in the electron transport chain [1]. Lack of oxygen (hypoxia) in living tissues is linked to the pathology of various diseases, including cancer, cerebral infarction, chronic kidney disease, and diabetic retinopathy [2–4]. The quantitative detection of O_2 levels in living cells and tissues is therefore of great importance in elucidating hypoxia-related diseases.

Much attention has been paid in recent years to high sensitivity, low invasiveness optical O_2 detection method based on phosphorescence quenching that uses oxygen probes [5–12]. However, although the phosphorescence intensity can be easily measured, it cannot be used for quantitative O_2 measurements in living cells or tissues because the emission intensity depends on the distribution of the probe concentration and on the excitation light intensity. In contrast, the phosphorescence lifetime is essentially unaffected by these factors. Oxygen tension in living cells and tissues has thus been quantified using phosphorescence lifetime measurements by employing phosphorescent molecules such as Pt(II)- or Pd(II)-porphyrins [5,6,13–15], Ru(II) complexes [16,17], and Ir(III) complexes [18–22] as O_2 probes. However, although such lifetime-based measurements are useful for the quantitative detection of O_2 levels, they require a pulsed excitation light source and a time-resolved measurement system.

Unlike lifetime measurements, the ratiometric measurements do not require specialized equipment to quantify O_2 levels. Two different types of probes have been developed for ratiometric O_2 measurements: nanoparticle-based probes and small-molecule-based probes. In nanoparticle-based ratiometric O_2 probes [23–31], an oxygen-insensitive

fluorescent unit and an oxygen-sensitive phosphorescent unit are incorporated in organic or inorganic nanoparticles. Covalent immobilization is preferred to prevent leaching of the sensor units. For intracellular O_2 measurements, nanoparticle-based probes have the advantage that the sensor dyes are shielded from intravital compounds. However, these dyes usually require relatively long incubation times with the samples to obtain a sufficiently strong emission signal, probably because cellular uptake of the dyes is mainly through endocytosis.

The chemical structures of small-molecule-based probes [32–36], on the other hand, can be easily modified to improve cellular uptake efficiency. Small-molecule ratiometric O_2 probes usually have a fluorescent unit (functioning as an internal standard) and a phosphorescent unit (functioning as an O_2 sensor dye), and these units are linked through an oligopeptide linker [32]. The ratiometric O_2 probe C343-Pro$_4$-BTP consists of a blue fluorescent coumarin dye (C343) unit and a red phosphorescent iridium complex (BTP) connected by a tetraproline linker (Figure 2-1). C343-Pro$_4$-BTP acts as a ratiometric O_2 probe in solution and in lipid membranes, allowing detection of changes in the O_2 levels of cultured cells. However, C343-Pro$_4$-BTP cannot quantify O_2 distribution in cells due to its low cellular uptake. To improve cellular uptake, C343-Pro$_8$-BTQphen (Figure 2-1) were designed and synthesized, bearing a cationic iridium complex (BTQphen) [33]. Although C343-Pro$_8$-BTQphen was taken up by cells more efficiently than C343-Pro$_4$-BTP, uptake was still insufficient for quantitative O_2 measurements in living cells.

In this chapter, new ratiometric O_2 probes were designed and synthesized, in which containing an arginine peptide as a linker. Arginine-rich peptides are cationic and can penetrate cells, and are widely used to promote the intracellular delivery of molecules with low plasma membrane permeability [37]. The C343 fluorophore with 7-

diethylaminocoumarin (7DEAC) in the ratiometric probe was replaced because of improvement of stability to acid during synthesis. Figure 2-2 shows the chemical structures of 7DEAC-R_8-BTQphen (**R8**) and 7DEAC-R_{12}-BTQphen (**R12**), in which 7DEAC and BTQphen are connected with arginine peptide linkers of different lengths. The practical application of small-molecule-based O_2 probes to intracellular O_2 measurements requires an understanding of the relaxation processes in the excited states. Thus, the photophysical properties of **R8** and **R12** in solution were revealed by comparing these reference compounds. The O_2 response of these ratiometric probes were investigated in solutions, in lipid bilayer membranes, and in living cells.

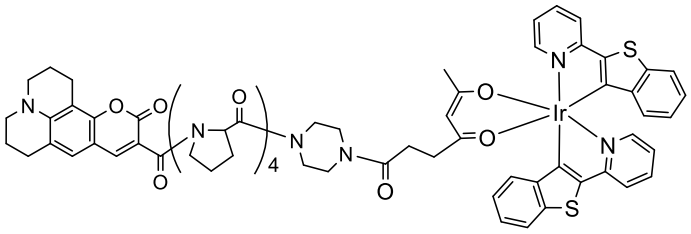

C343-Pro$_4$-BTP

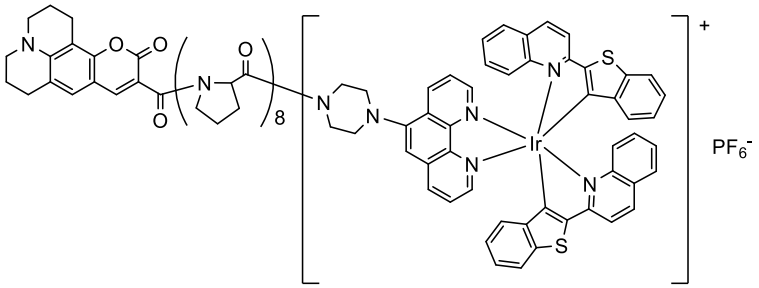

C343-Pro$_8$-BTQphen

Figure 2-1. Chemical structures of the previous ratiometric probes C343-Pro$_4$-BTP and C343-Pro$_8$-BTQphen.

Ratiometric probes

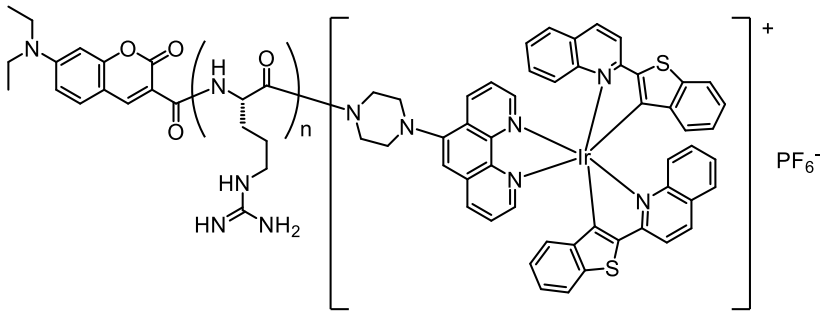

7DEAC-R_n-BTQphen (n = 8, 12)

Reference compounds

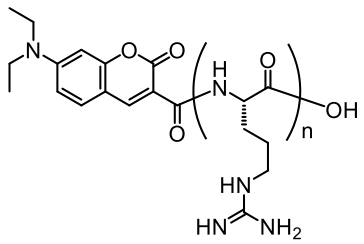

7DEAC-R_n-OH (n = 8, 12)

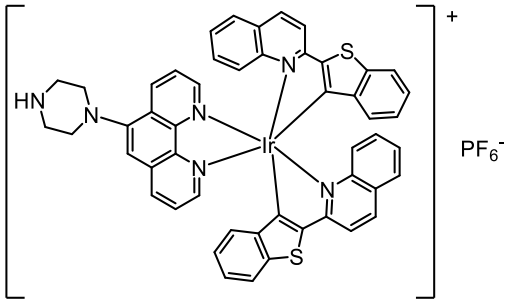

BTQphen

Figure 2-2. Chemical structures of ratiometric probes 7DEAC-R_8-BTQphen (**R8**), 7DEAC-R_{12}-BTQphen (**R12**) and their reference compounds (7DEAC-R_8-OH, 7DEAC-R_{12}-OH, and BTQphen).

2-2 Experimental Section

2-2-1 Materials

The ratiometric probes (**R8** and **R12**) and their reference compounds were synthesized and characterized as described in section 2-5. All reagents and solvents used in syntheses were purchased from BeadTech, Watanabe Chemical Industries, Peptide Institute, Tokyo Chemical Industries, Wako Pure Chemical Industries, or Kanto Chemical, and were used without further purification. ^{1}H-NMR spectra were recorded with a JNM-ECS300 (JEOL) at 300 MHz or a JNM-ECS400 (JEOL) at 400 MHz. ^{1}H-NMR chemical shifts were referenced to tetramethylsilane. ESI-MS and MALDI-TOF-MS measurements were carried out on an API 2000 (Applied Biosystems) and an AXIMA performance (Shimadzu) mass spectrophotometers.

A stock solution of each probe (1 mM) for cellular experiments was prepared by dissolving in dimethyl sulfoxide (DMSO, spectrophotometric grade, Kanto Chemical). Acetonitrile (MeCN, spectrophotometric grade, Kanto Chemical) was used as received.

2-2-2 Absorption and emission spectra

Absorption and emission spectra were recorded on a UV-Vis spectrophotometer (Ubest V-550, JASCO) and a photonic multichannel analyzer PMA-12 (C11027-01, Hamamatsu Photonics) equipped with a monochromatized Xe arc lamp, respectively. The emission spectra of 7DEAC in MeOH:EtOH (1:1 v/v) at 77 K were measured with a spectrofluorometer (F-7000, Hitachi). The emission spectrum was corrected for spectral sensitivity.

2-2-3 Fluorescence and phosphorescence lifetimes

Phosphorescence lifetimes were measured with a time-correlated single-photon counting fluorimeter (Quantaurus-Tau C11367G, Hamamatsu). A laser diode (M12488-29, Hamamatsu Photonics; 405 nm, pulse width 49 ps) was used as the excitation light source (Figure 2-3). Picosecond fluorescence lifetime measurements were made using a femtosecond laser system based on a mode-locked Ti:sapphire laser (Tsunami; center wavelength 800 nm, pulse width ~70 fs repetition rate 82 MHz) pumped by a CW green laser (Spectra-Physics, Millenia V; 532 nm, 4.5W) [38]. The block diagram of this system is shown in Figure 2-4. The repetition frequency was reduced to 4 MHz by using a pulse picker (model 3980, Spectra-Physics), and the third harmonic (266 nm, FWHM ~250 fs) was used as the excitation source. The monitoring system consisted of a microchannel plate photomultiplier tube (MCP-PMT; Hamamatsu, R3809U-51) cooled to −20 °C and a single-photon counting module (SPC-530, Becker and Hickl). The fluorescence photon signal detected by the MCP-PMT and the photon signal of the second harmonic (400 nm) of the Ti:sapphire laser was used for the start and stop pulses of the time-to-amplitude converter in this system. The instrument response function had a half-width of about 25 ps. The fluorescence lifetime profiles were analyzed by deconvolution using the instrument response function.

2-2-4 Fluorescence and phosphorescence quantum yields

Fluorescence and phosphorescence quantum yields were determined on an absolute photoluminescence quantum yield measurement system (C9920-02, Hamamatsu Photonics) consisting of a Xe arc lamp, a monochromator, an integrating sphere, and a multichannel detector [39] (Figure 2-5).

2-2-5 Liposome experiments

Lipid membranes of *L*-α-dimyristoyl-phosphatidylcholine (DMPC; Sigma) containing 20 mol% cholesterol (Chol; Sigma) were generated as small unilamellar vesicles prepared by the ethanol injection method [40]. An ethanolic solution of DMPC (24 mM) and Chol (6 mM), and a DMSO stock solution of each probe (600 μM) were injected rapidly into Tris/HCl buffer (pH 7.0). The final concentration of DMPC/Chol and the probe was 0.8 mM/0.2 mM and 10 μM, respectively.

2-2-6 Cell culture and imaging

HeLa cells were cultured in Dulbecco's modified Eagle's medium (DMEM, Gibco) with 10% fetal bovine serum, penicillin (50 units/mL), and streptomycin (50 μg/mL). All cells were grown at 37 °C under a 5% CO_2 atmosphere. HeLa cells were seeded into glass bottom imaging dishes (Greiner) and allowed to adhere for 24 h. The cells were incubated with the probes (2 μM) for 2 h, washed 3 times with DMEM, and then the medium was replaced with DMEM (FluoroBrite, Gibco) without fetal bovine serum. Emission imaging experiments with these HeLa cells were performed on an inverted microscope (IX71, Olympus) equipped with an O_2 concentration-changeable multigas incubator (INUBONICS-F1-H2, GM-8000, TOKAI HIT), a 10× or 40× oil-immersion objective lens (UPLSAPO 10×, UPLFLN40×O, Olympus), and an electron multiplying CCD camera (Evolve 512, PHOTOMETRICS) driven by MetaMorph software to obtain luminescence microscopic images. A dual view simultaneous-imaging system (DV2, PHOTOMETRICS) was used for ratiometric imaging (Figure 2-6). Samples were excited using a 150 W mercury lamp.

2-2-7 Cell viability assay

HeLa cells (5×10^3 cells/well) were seeded into a 96-well flat bottom plate (Greiner) and allowed to adhere for 12 h. The stock solution of Ir(III) complex (1 mM) was diluted with DMEM containing 10% fetal bovine serum, penicillin (50 units/mL), and streptomycin (50 μg/mL). The cells were incubated with the probe for 2 h at 37 °C under a 5% CO_2 atmosphere. The medium was removed and the cells were washed gently with DMEM without phenol red. Cell counting kit-8 reagent (CCK-8, Dojindo) was added to each well and incubation was continued for 2 h. The absorbance at 450 nm of each well referenced at 650 nm was recorded using a microplate reader (Infinite 200 PRO, TECAN). Cell viability (% of control) was evaluated as $(A_{sample} - A_{blank}) / (A_{control} - A_{blank}) \times 100$, where A_{sample} is the absorbance of cells exposed to the probe, $A_{control}$ is the absorbance of cells without probe, and A_{blank} is the absorbance of wells without cells.

2-2-8 Emission spectra in living cells

HeLa cells (5.0×10^4 cells/well) were seeded into a 96-well flat bottom plate (Greiner) and allowed to adhere for 5 h. The emission signals of the probe were measured using a microplate reader (Infinite 200 PRO, Tecan) equipped with a gas control module (GCM, Tecan).

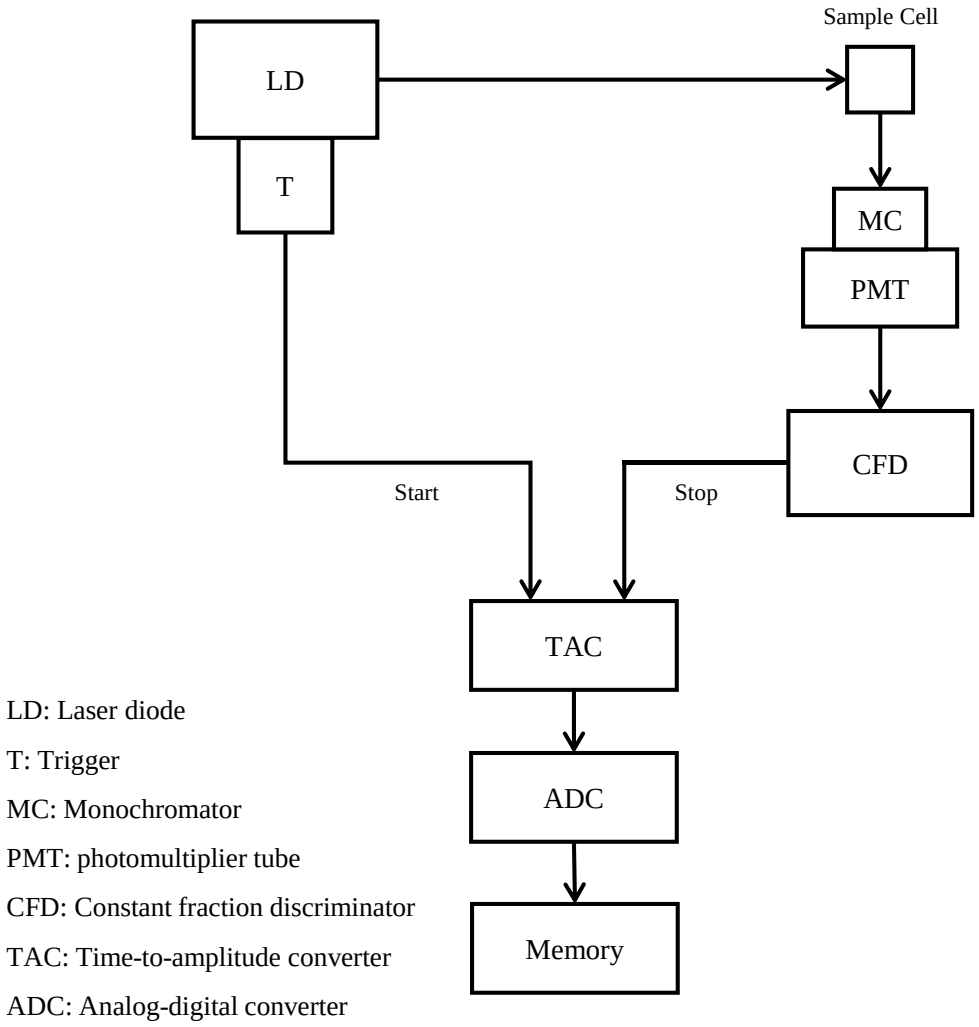

Figure 2-3. Schematic diagram of the multiplexed time-correlated single photon counting instrument (C11367G).

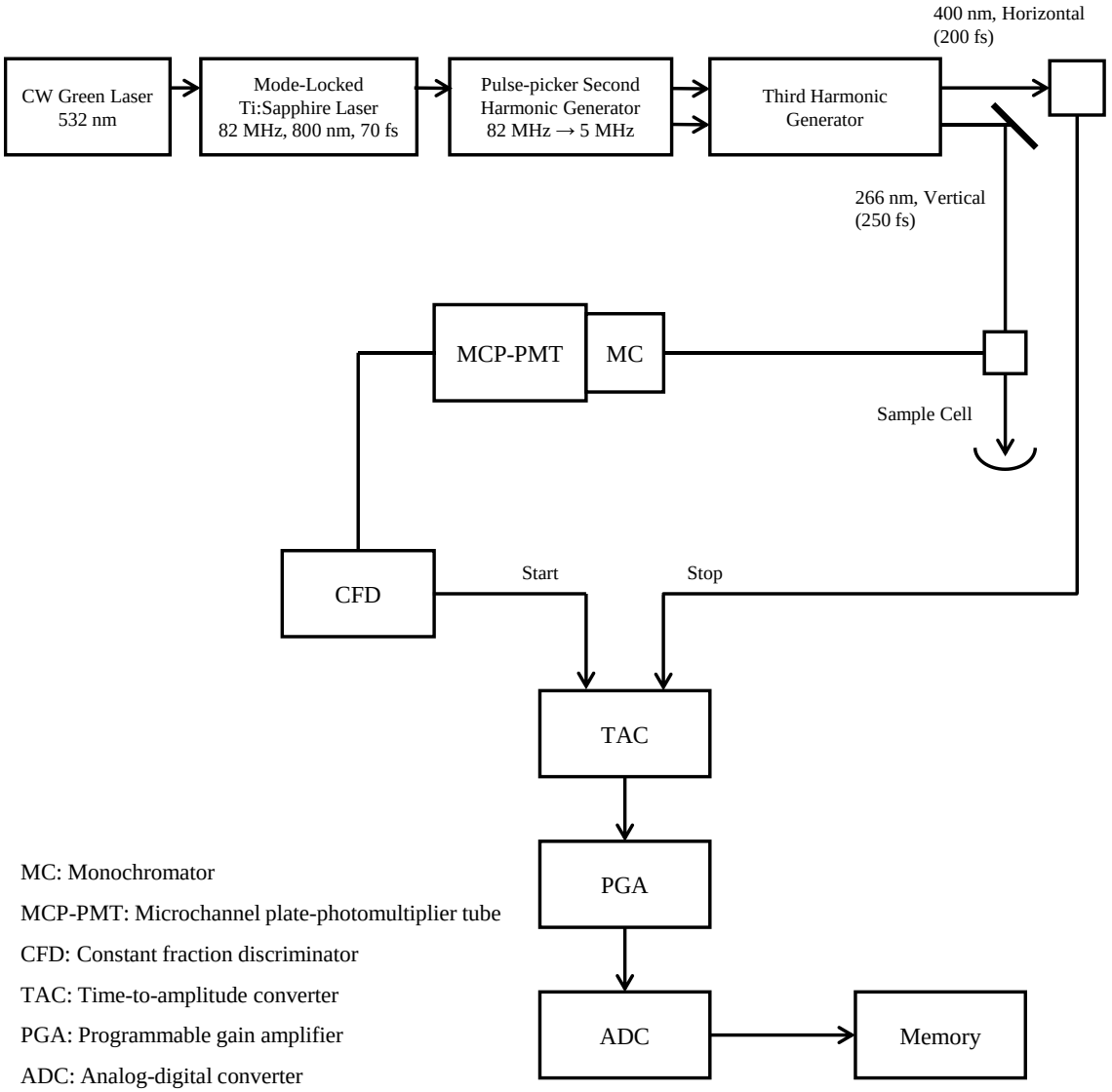

Figure 2-4. Experimental set up for picosecond fluorescence lifetime measurements based on the time-correlated single-photon counting method.

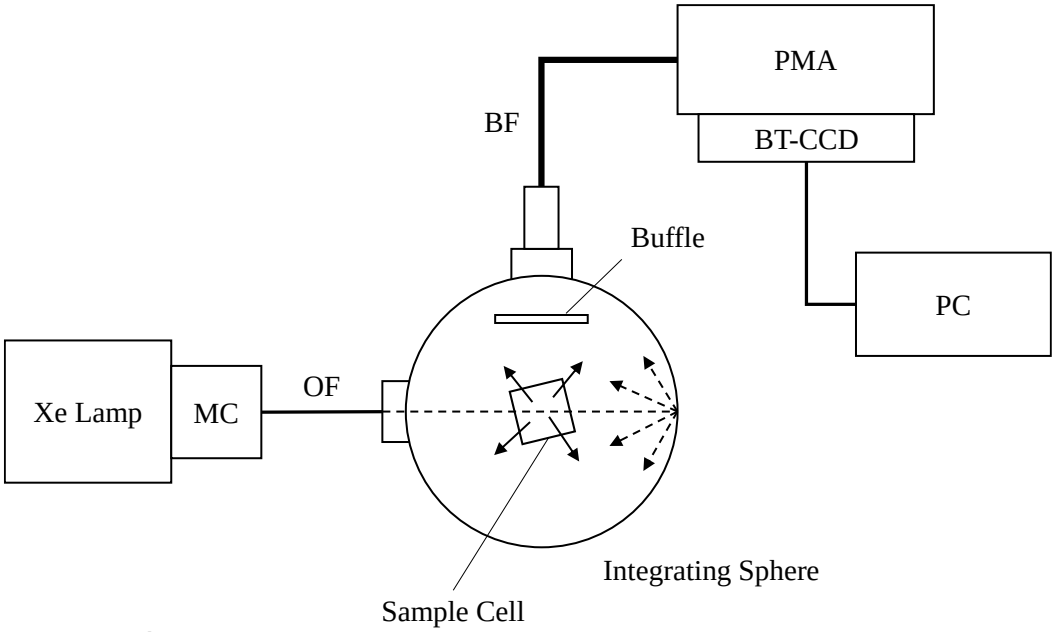

MC: Monochromator

OF: Optical fiber

BF: Bundle fiber

PMA: Photonic Multichannel Analyzer

BT-CCD: Back-thinned CCD

PC: personal computer

Figure 2-5. Schematic diagram of the absolute photoluminescence quantum yield measurement system.

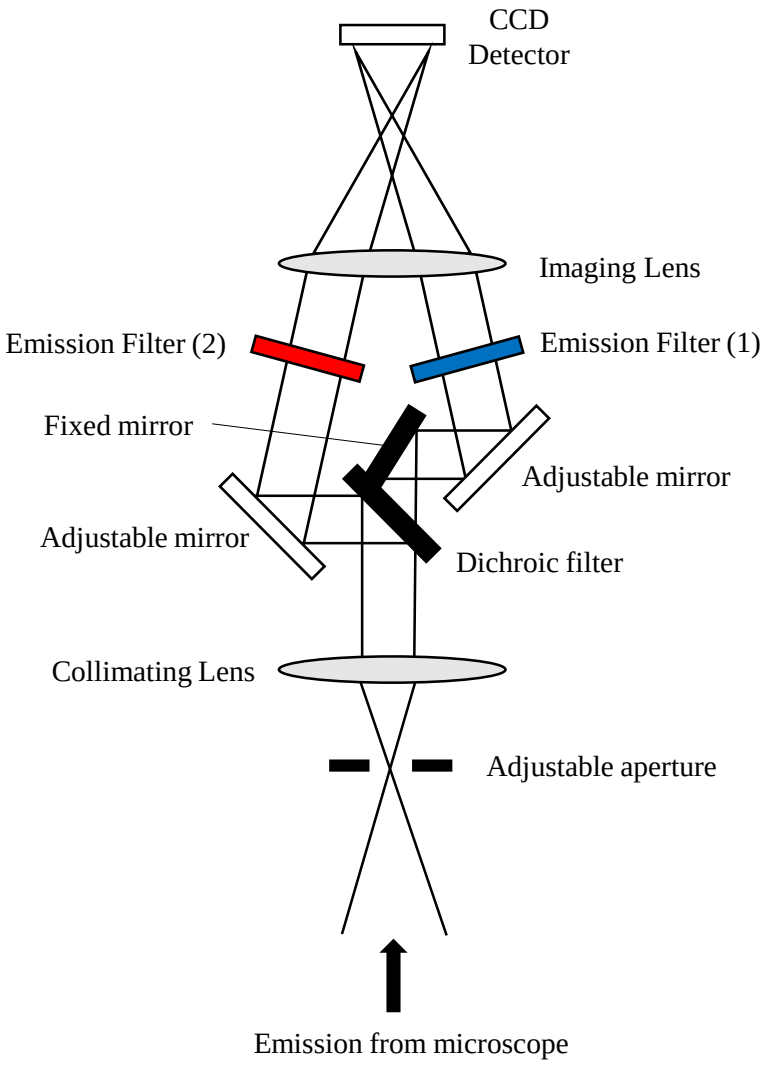

Figure 2-6. Schematic diagram of the emission pathways of the DV2.

2-3 Results and Discussion

2-3-1 Photophysical properties of the probes in solution

The relaxation processes of **R8** and **R12** were clarified in the excited state by first examining their spectral and photophysical properties in solution. The absorption spectra of **R8** and **R12** in MeCN (Figure 2-7A) show very similar spectral shapes, giving two absorption bands with maxima at around 500 and 425 nm. By comparing the absorption spectra of these ratiometric probes with those of the reference compounds (7DEAC-R_8-OH, 7DEAC-R_{12}-OH and BTQphen) (Figure 2-8A), the first absorption band at around 500 nm was assigned to the singlet metal-to-ligand charge transfer (^{1}MLCT) transition of the BTQphen moiety [41] and the second absorption band at around 425 nm was assigned to the π,π^* transition due to the 7DEAC chromophore. The latter absorption band has a much larger molar absorption coefficient (ε_{R8}^{425} = 49,000 dm^3 mol^{-1} cm^{-1}, ε_{R12}^{425} = 44,000 dm^3 mol^{-1} cm^{-1}) than the former. These ε values were determined by assuming that all guanidino units in **R8** and **R12** were bound to trifluoroacetic acid which was used for deprotection of protecting group. Figure 2-7B shows the emission spectra of **R8** and **R12** in MeCN upon excitation at 405 nm under different O_2 partial pressures. As described above, the excitation photons at 405 nm are mainly absorbed by the 7DEAC moiety. Comparison of Figure 2-7B and Figure 2-8B allows the **R8** and **R12** emission bands with maxima at 470 and 660 nm to be assigned to the fluorescence of the 7DEAC moiety and the phosphorescence of the BTQphen moiety, respectively. The observed extremely small overlap between the fluorescence and phosphorescence spectra is advantageous for ratiometric measurements. The fluorescence intensities of **R8** and **R12** were essentially constant under different O_2 partial pressures, whereas the phosphorescence intensities

greatly decreased as the O_2 partial pressure increased, indicating that **R8** and **R12** in MeCN are sensitive to O_2 concertation.

The photophysical parameters of **R8**, **R12**, and their reference compounds in MeCN were measured (Table 2-1). The fluorescence quantum yields (Φ_f^0) of **R8** and **R12** (0.008 and 0.012) are significantly smaller those of 7DEAC-R_8-OH and 7DEAC-R_{12}-OH (0.058 and 0.062). The large overlap between the fluorescence spectrum of 7DEAC-R_n-OH (n = 8, 12) and the absorption spectrum of BTQphen (Figure 2-8) suggest the occurrence of energy transfer from 7DEAC to the BTQphen moiety. To ascertain the involvement of intramolecular energy transfer in **R8** and **R12**, the phosphorescence excitation spectra monitored at 660 nm (Figure 2-9) were measured. These spectra showed a band due to absorption by 7DEAC at around 425 nm and a band due to absorption by BTQphen at around 500 nm. These results indicate singlet-singlet energy transfer from 7DEAC to the BTQphen chromophore in **R8** and **R12**.

The efficiency of singlet energy transfer (Φ_{SET}) from 7DEAC to BTQphen can be estimated by measuring the phosphorescence quantum yield using two excitation wavelengths (405 and 500 nm). Excitation of **R8** and **R12** at 405 nm produces either the excited state of 7DEAC or BTQphen, depending on the molar absorption coefficients of the two chromophores ($\varepsilon_{7DEAC}^{405}$ = 29,040 dm^3 mol^{-1} cm^{-1} and $\varepsilon_{BTQphen}^{405}$ = 10,280 dm^3 mol^{-1} cm^{-1}). The phosphorescence quantum yield (Φ_p^{405}) obtained by excitation at 405 nm thus follows Eq. (2-1):

$$\Phi_p^{405} = \frac{\varepsilon_{7DEAC}^{405}}{\varepsilon_{7DEAC}^{405}+\varepsilon_{BTQphen}^{405}} \Phi_{SET}\Phi_p^{500} + \frac{\varepsilon_{BTQphen}^{405}}{\varepsilon_{7DEAC}^{405}+\varepsilon_{BTQphen}^{405}} \Phi_p^{500} \qquad (2\text{-}1)$$

where Φ_p^{500} is the phosphorescence quantum yield measured by excitation at 500 nm, i.e., selective excitation of the BTQphen moiety. From measurements based on Eq. (2-1), the Φ_{SET} values were estimated to be 0.69 and 0.57 for **R8** and **R12**, respectively.

Next, the intramolecular energy transfer efficiencies of **R8** and **R12** were investigated based on fluorescence lifetime measurements. The fluorescence decay curves of **R8** and **R12** and their reference compounds monitored at 470 nm (Figure 2-10) could be fitted to bi-exponential decay functions, expressed by Eq. (2-2):

$$I_p(t) = A_1\exp(-t/\tau_1) + A_2\exp(-t/\tau_2) + B \qquad (2\text{-}2)$$

where A_1 and A_2 are the pre-exponential factors, and B is the baseline of the decay. The obtained fluorescence lifetimes of **R8** and **R12** were τ_1 = 51 ps (A_1 = 0.74) and τ_2 = 148 ps (A_2 = 0.26), and τ_1 = 85 ps (A_1 = 0.81) and τ_2 = 248 ps (A_2 = 0.19), respectively (Table 2-1). The decay curves of the reference compounds 7DEAC-R_8-OH and 7DEAC-R_{12}-OH also followed bi-exponential decay functions, with lifetimes of τ_1 = 168 ps (A_1 = 0.87) and τ_2 = 476 ps (A_2 = 0.13), and τ_1 = 157 ps (A_1 = 0.80) and τ_2 = 441 ps (A_2 = 0.20), respectively. Since the fluorescence lifetimes of the reference compounds could be analyzed using bi-exponential functions, the two-component lifetimes of **R8** and **R12** in MeCN can be ascribed to intramolecular hydrogen-bonding interactions between 7DEAC and the guanidino groups of the oligoarginines.

Assuming that the quenching of DEAC fluorescence is entirely due to intramolecular energy transfer, the efficiency of intramolecular singlet-singlet energy transfer of **R8** and **R12** can be estimated by Eq. (2-3) using the intensity-averaged lifetime ($\langle\tau\rangle_{int}$) shown in Eq. (2-4):

$$\Phi_{SET} = 1 - \frac{\tau_{DA}}{\tau_D} \qquad (2\text{-}3)$$

$$\langle\tau\rangle_{int} = \frac{A_1\tau_1^2+A_2\tau_2^2}{A_1\tau_1+A_2\tau_2} \qquad (2\text{-}4)$$

where τ_{DA} and τ_D are the intensity-averaged fluorescence lifetimes of the ratiometric probes (**R8** and **R12)** and their reference fluorophore compounds, respectively. The obtained Φ_{SET} values were 0.61 for **R8** and 0.45 for **R12.** These values are in good agreement with those (0.69 and 0.57) estimated from Eq. (2-1), indicating that fluorescence quenching in **R8** and **R12** is due predominantly to intramolecular energy transfer. The smaller energy transfer efficiency of **R12** can be ascribed to the longer distance between the 7DEAC and BTQphen chromophores, showing that energy transfer efficiency can be controlled by adjusting the length of the linker between two chromophores. It should be noted in Table 2-1 that the phosphorescence lifetimes (τ_p and τ_p^0) of **R8** and **R12** under aerated and degassed conditions are almost the same as that of the reference compound BTQphen. This indicates that the phosphorescence of **R8** and **R12** is quenched exclusively by oxygen dissolved in MeCN, and the contribution of the other phosphorescence quenching processes, such as reverse energy transfer and electron transfer, are negligible in the excited triplet state.

The spectral and photophysical data allowed derivation of the energy state diagram for **R8** and **R12**, including the relaxation processes, as shown in Figure 2-11. Here, the energy level of the excited triplet state (T_1) of the 7DEAC moiety was estimated from the phosphorescence spectral peaks of 7DEAC-R_8-OH and 7DEAC-R_{12}-OH in a rigid matrix at 77 K (Figure 2-12). Excitation at 405 nm mainly generates the excited singlet state (S_1)

of 7DEAC, along with direct formation of the S_1' state of BTQphen. Singlet-singlet energy transfer to the S_1' state of BTQphen and fluorescence emission competitively proceed from the S_1 state of 7DEAC. The S_1' state of BTQphen undergoes very fast intersystem crossing to produce the excited triplet state (T_1') of BTQphen with an almost unity quantum yield [42]. As can be seen from τ_p and τ_p^0 in Table 2-1, the phosphorescence property and O_2 sensitivity of the phosphor BTQphen are maintained in the ratiometric probes because triplet-triplet energy transfer between BTQphen and 7DEAC is thermodynamically unfavorable, a desirable attribute in a ratiometric O_2 probe.

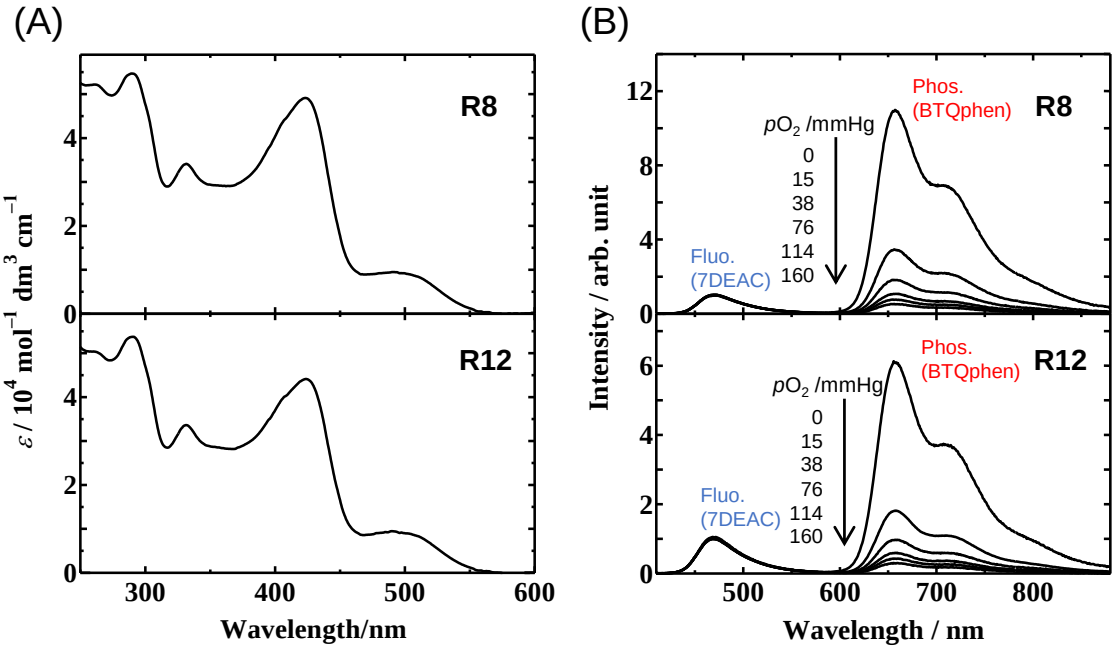

Figure 2-7. (A) Absorption and (B) emission spectra of **R8** and **R12** in acetonitrile under different oxygen partial pressures (pO_2) at room temperature. λ_{ex}: 405 nm

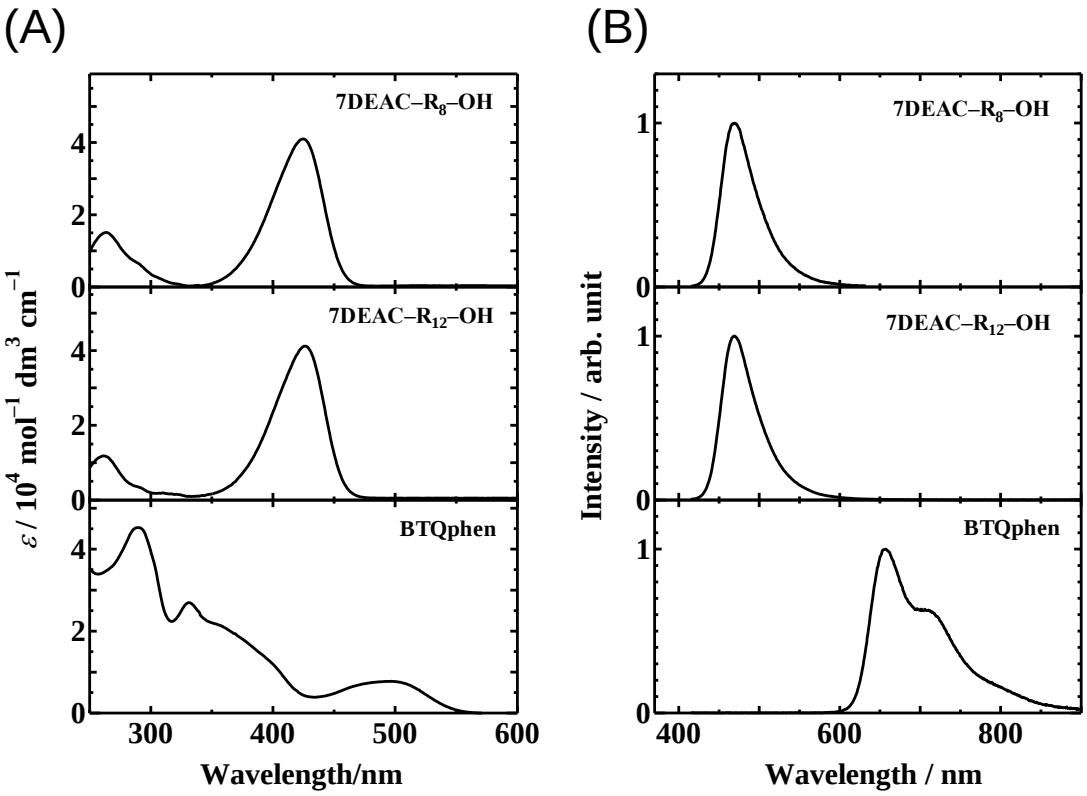

Figure 2-8. (A) Absorption and (B) emission spectra of 7DEAC-R_8-OH, 7DEAC-R_{12}-OH and BTQphen in MeCN. (λ_{ex} = 405 nm).

Table 2-1. Photophysical parameters of the ratiometric probes **R8**, **R12**, and the reference compounds in MeCN (λ_{em} = 405 nm).[1)]

Compound	Φ_f^0	Φ_p^0	Φ_p	τ_f/ps [2)]	$\langle\tau_f\rangle_{int}$/ps	τ_p^0/μs[3)]	τ_p/μs[3)]	Φ_{SET}
R8	0.008	0.23	0.013	51 (74%) [4)] 148 (26%)	100	5.8	0.28	0.69 [5)] (0.61) [6)]
R12	0.012	0.21	0.012	85 (81%) 248 (19%)	151	5.8	0.28	0.57 [5)] (0.45) [6)]
7DEAC-R_8-OH	0.058	-	-	168 (87%) 476 (13%)	260	-	-	-
7DEAC-R_{12}-OH	0.062	-	-	157 (80%) 441 (20%)	274	-	-	-
BTQphen	-	0.01	0.32	-	-	5.7	0.28	-

[1)] Φ_f^0, Φ_p^0, τ_p^0: fluorescence and phosphorescence quantum yields, and phosphorescence lifetime in degassed solution.; Φ_p, τ_f, τ_p: phosphorescence quantum yield, and fluorescence and phosphorescence lifetimes in aerated solution; Φ_{SET}: efficiency of intramolecular singlet-singlet energy transfer; [2)] Excited at 266 nm, monitored at 470 nm; [3)] Excited at 405 nm, monitored at 660 nm; [4)] In parentheses: relative amplitude.; [5)] Estimated from quantum yield measurements; [6)] Estimated from lifetime measurements

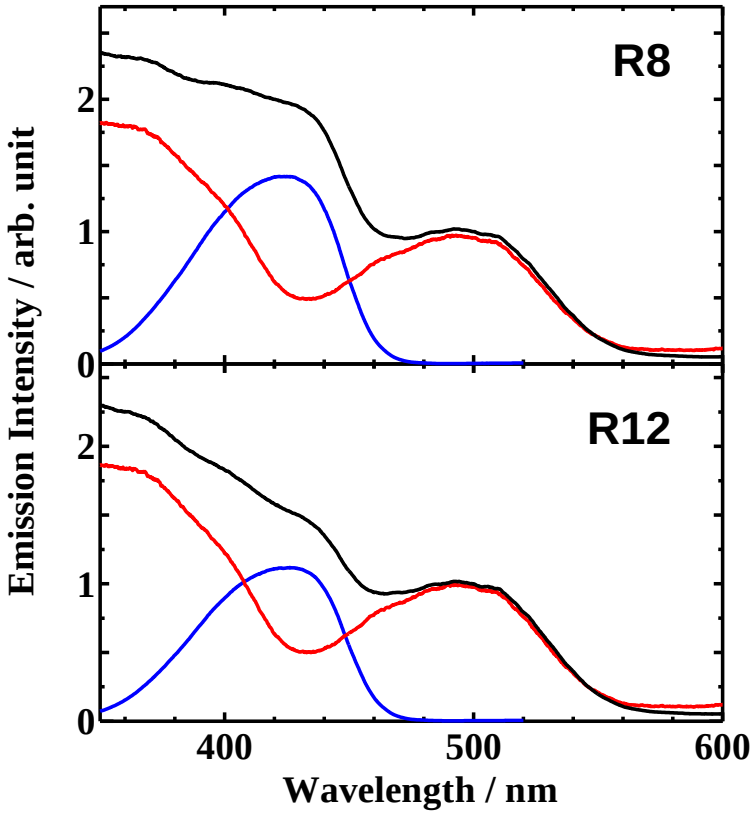

Figure 2-9. Excitation spectrum of ratiometric probes (λ_{em}: 660 nm, black line), and those of reference compounds for fluorophore (λ_{em}: 540 nm, blue line) and phosphor (λ_{em}: 660 nm, red line) in acetonitrile.

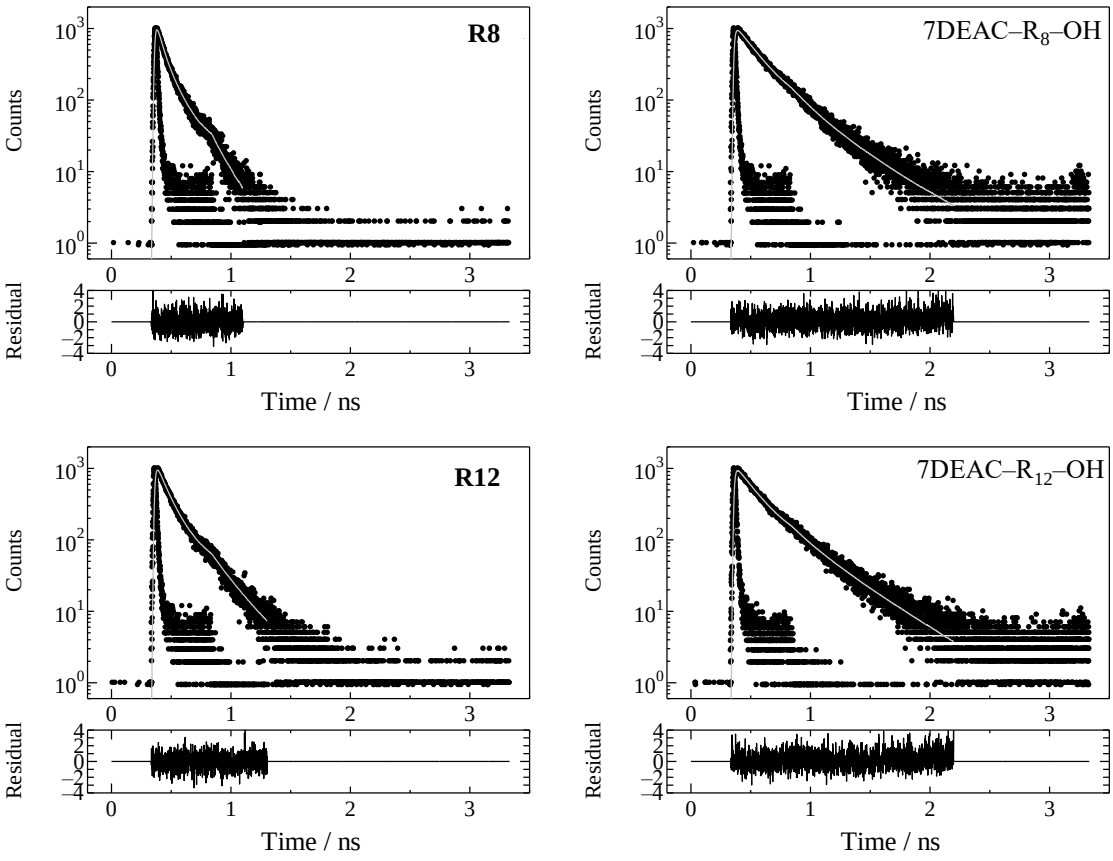

Figure 2-10. Fluorescence decay profiles of the ratiometric probes and the reference compounds for fluorophore in acetonitrile (λ_{ex}: 266 nm, λ_{em}: 470 nm).

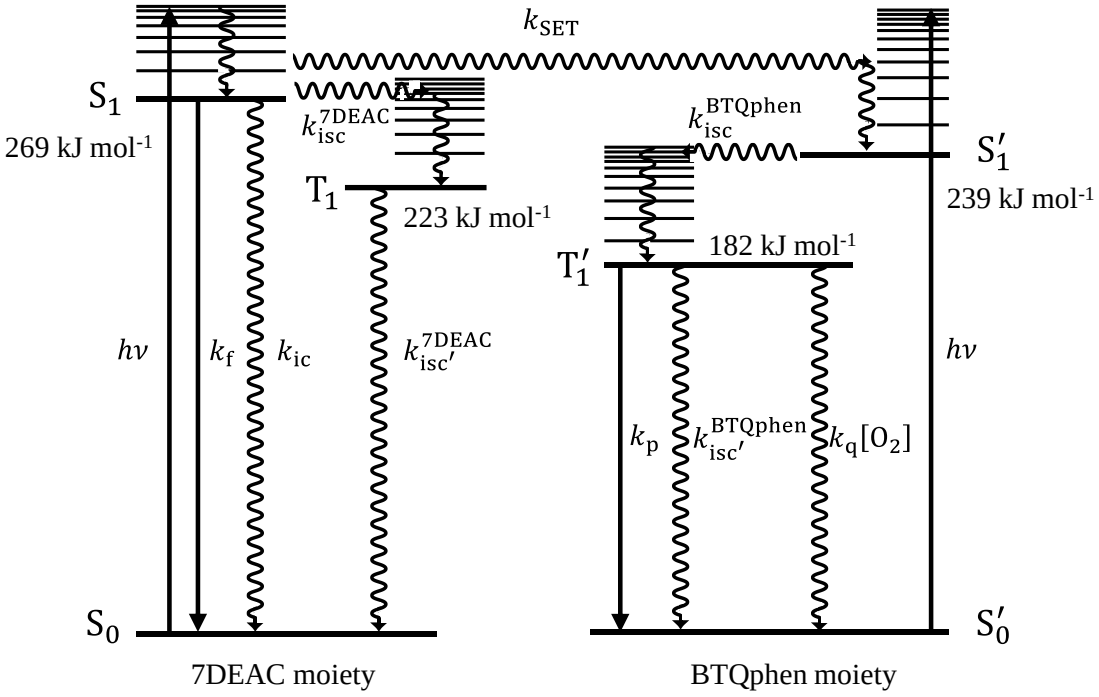

Figure 2-11. Energy state diagram and relaxation processes of the excited singlet (S_1) and triplet (T_1) states of **R8** and **R12**. k_{isc}, k_{isc}', k_f, k_{ic}, k_{SET}, k_p and k_q are the rate constants for $S_1 \rightarrow T_1$ and $T_1 \rightarrow S_0$ intersystem crossing, fluorescence, internal conversion, singlet energy transfer, phosphorescence, and oxygen quenching, respectively.

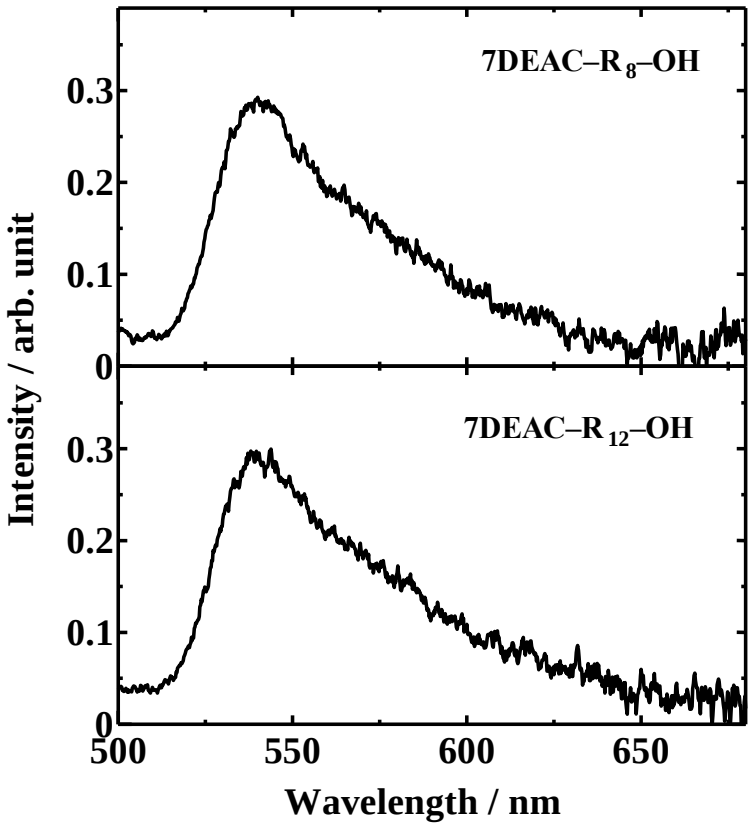

Figure 2-12. Phosphorescence spectra of 7DEAC-R_8-OH and 7DEAC-R_{12}-OH in MeOH:EtOH (1:1 v/v) rigid glass at 77 K (λ_{ex}:450 nm).

2-3-2 Oxygen response in solution and in a lipid bilayer membrane

In ratiometric O_2 measurements, the O_2 concentration is determined by measuring the ratio ($R_I = I_p / I_f$) between the fluorescence intensity (I_f), which is almost independent of the O_2 concentration, and the phosphorescence intensity (I_p), which depends significantly on the O_2 concentration. Assuming that the effects of O_2 concentration ($[O_2]$) or partial pressure (pO_2) on the fluorescence intensity of the probe is negligibly small under the experimental conditions, the following equation can be derived based on the Stern-Volmer equation:

$$\frac{R_I^0}{R_I} = \frac{I_p^0/I_f^0}{I_p/I_f} = 1 + K_{SV}\,[O_2] = 1 + K_{SV}\,pO_2 \qquad (2\text{-}5)$$

where I_p^0 and I_f^0 are the phosphorescence and fluorescence intensities in the absence of O_2, and R_I^0 denotes their ratio. K_{SV} is the Stern-Volmer constant, given by the product of the phosphorescence quenching rate constant (k_q) and the phosphorescence lifetime (τ_p^0) in the absence of O_2. By using the R_I^0 and K_{SV} values determined in advance, ratiometric measurements enable us to quantify the $[O_2]$ or pO_2 of the medium (e.g., cells and tissues) in which the probe is distributed.

In living cells, the ratiometric probes **R8** and **R12** are expected to accumulate in organelle membranes because of their high lipophilicity. The affinities of **R8** and **R12** to a lipid bilayer membrane composed of dimyristoyl-L-α-phosphatidylcholine (DMPC) with 20 mol% cholesterol (Chol) were investigated and measured their O_2 sensitivities in the membrane at 35 °C. Since the phase transition temperature of DMPC membrane is 23 °C, DMPC/Chol membranes would be in the liquid-crystal state at 35 °C. The fluorescence spectra of **R8** and **R12** in Tris-HCl buffer shifted to shorter wavelengths in

the presence of DMPC/Chol membrane (Figure 2-13), demonstrating that **R8** and **R12** are incorporated into the DMPC/Chol membrane [43]. The phosphorescence decay profiles of **R8** and **R12** in the presence of DMPC/Chol vesicles in aerated Tris-HCl buffer (Figure 2-14) could be analyzed by a single exponential function with a lifetime of 1.01 μs and 0.99 μs, respectively. These results show that the ratiometric probes are efficiently incorporated into the liposome membrane.

Next, the oxygen sensitivity of the ratiometric probes was examined in DMPC/Chol membranes. Figure 2-15 shows plots of R_I^0/R_I for **R8** and **R12** against pO_2, derived from the pO_2 dependencies of the fluorescence and phosphorescence intensities in MeCN and in lipid membrane. The slope of the straight line provided K_{SV} values of **R8** in MeCN and in DMPC/Chol membrane of 0.12 $mmHg^{-1}$ and 0.027 $mmHg^{-1}$, respectively. There were no significant differences in the O_2 sensitivities of **R8** and **R12** (Table 2-2). To confirm the reliability of the O_2 levels obtained by ratiometric measurements, the phosphorescence lifetime of **R8** excited at 405 nm and monitored at 660 nm was measured with a time-correlated single-photon counting system. By plotting the τ_p^0/τ_p value against pO_2 according to the Stern-Volmer equation (Figure 2-16), the *K*sv values in MeCN and in DMPC/Chol membrane were determined to be 0.12 $mmHg^{-1}$ and 0.024 $mmHg^{-1}$, respectively. These values are in good agreement with those obtained with the ratiometric measurements (Table 2-2), thus confirming the reliability of our ratiometric O_2 measurements in both lipid membrane and in solution.

The k_q values (5.3×10^3 and 5.1×10^3 $mmHg^{-1}$ s^{-1}) of **R8** and **R12** in DMPC/Chol membrane were significantly smaller than in MeCN (2.1×10^4 $mmHg^{-1}$ s^{-1}). Using the partition coefficient of O_2 to a DMPC/Chol membrane in water [44], the k_q values of **R8** and **R12** in a DMPC/Chol membrane can be expressed in terms of concentration as

8.6×10^{8} and 8.3×10^{8} M^{-1} s^{-1}, respectively. These values are smaller than the value obtained in MeCN (1.8×10^{9} M^{-1} s^{-1}), perhaps due to a decrease in the diffusion rate of O_2 and the probe in the lipid bilayer membrane.

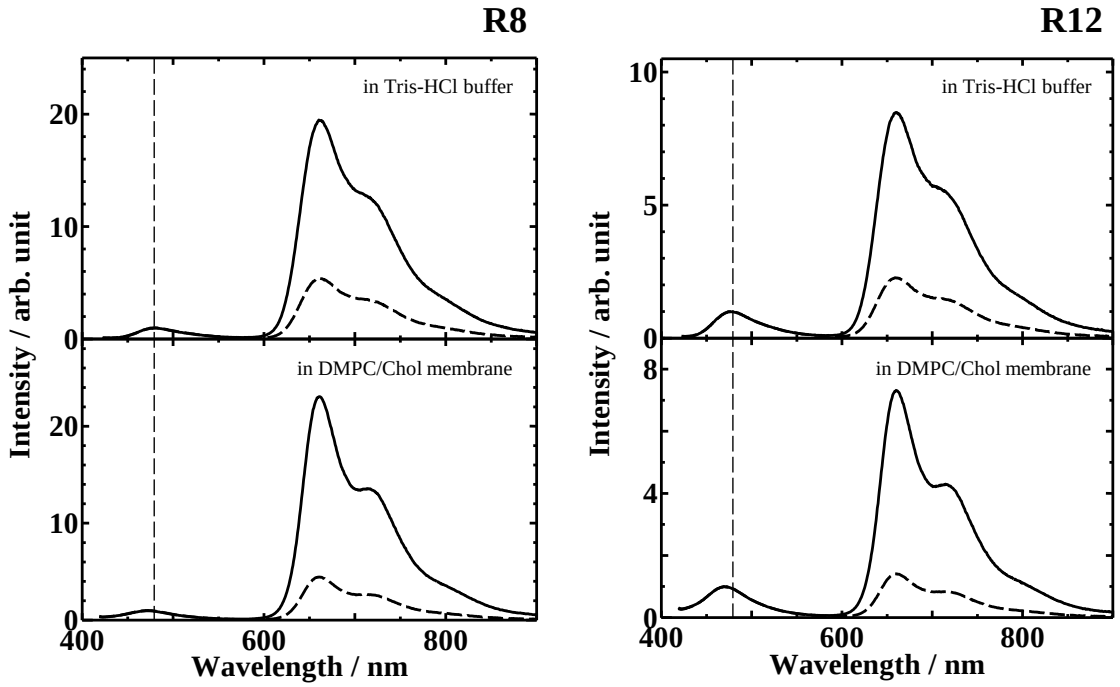

Figure 2-13. Emission spectra of **R8** and **R12** under the absence or presence of unilamellar DMPC/Chol vesicles in Tris-HCl buffer solutions (pH = 7) at 37 °C. Solid line: in N_2 saturated solutions, broken line: in aerated solutions.

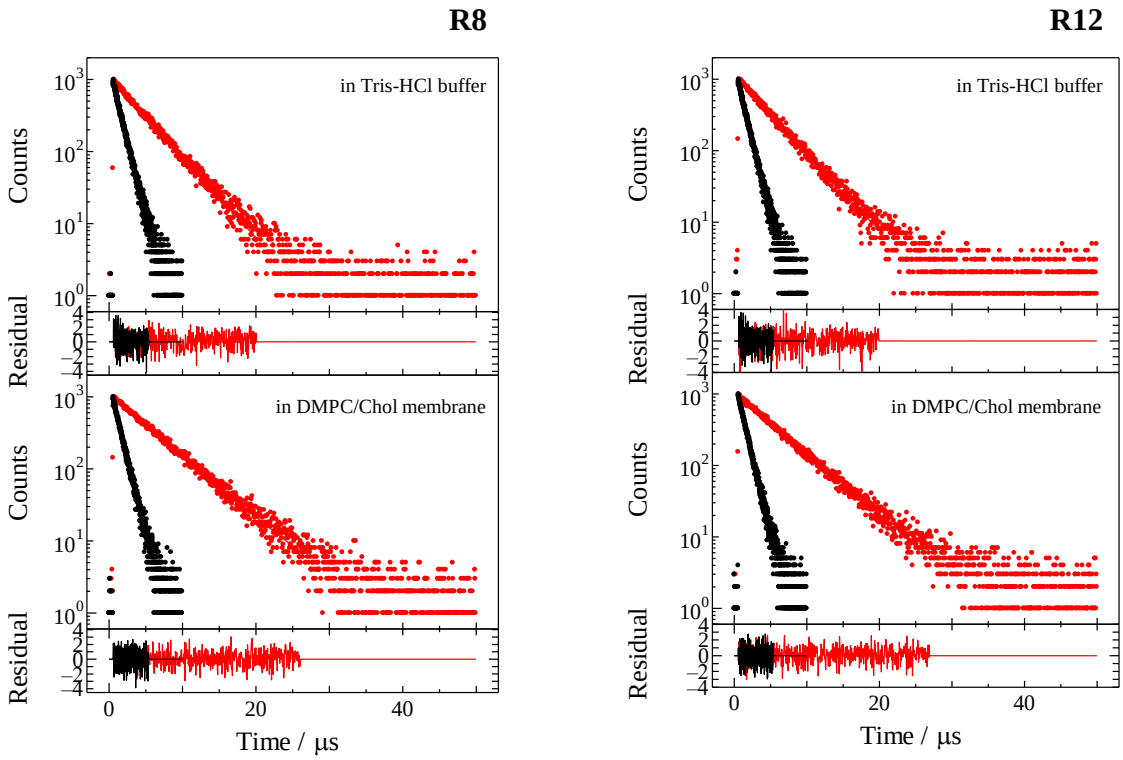

Figure 2-14. Phosphorescence decay curves of **R8** and **R12** in Tris-HCl buffer solutions (pH = 7) under the absence or presence of unilamellar vesicles of DMPC/Chol at 37 °C. Red: in N_2 saturated solutions, black: in aerated solutions.

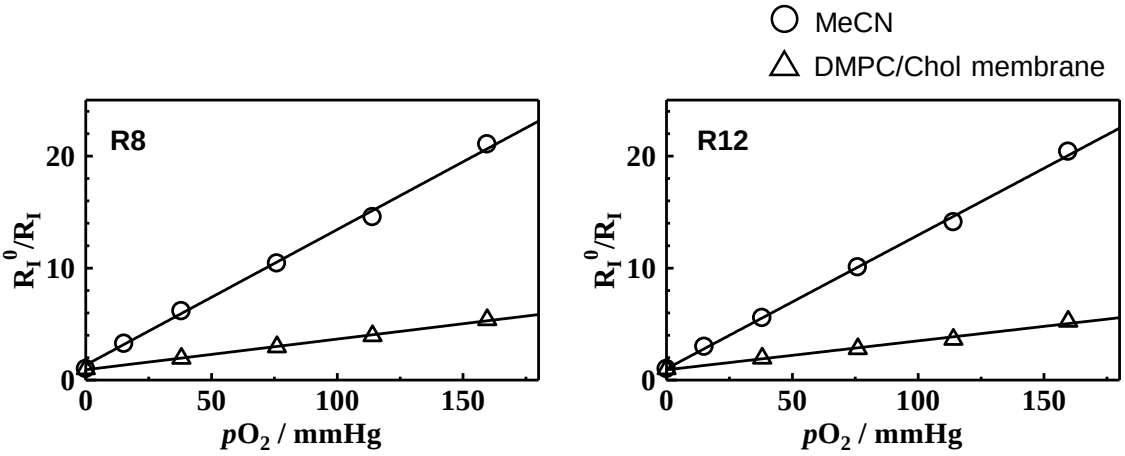

Figure 2-15. Plots of R_I^0/R_I vs. pO_2 for **R8** and **R12** in acetonitrile and in DMPC/Chol membrane at 37 °C.

Table 2-2. Stern-Volmer constant (K_{SV}) and oxygen quenching rate constant (k_q) of **R8** and **R12** in MeCN and in DMPC/Chol membranes.

Compound	Solvent	K_{SV} /mmHg^{-1}	K_{SV} /mM^{-1}	k_q /10^4 mmHg^{-1} s^{-1}	k_q /10^9 M^{-1} s^{-1}	τ_p^0/μs
R8	MeCN	0.12	10.4	2.1	1.8	5.8
	DMPC/Chol	0.027	4.3	0.53	0.86	5.0
R12	MeCN	0.12	10.0	2.1	1.7	5.8
	DMPC/Chol	0.025	4.0	0.51	0.83	4.9

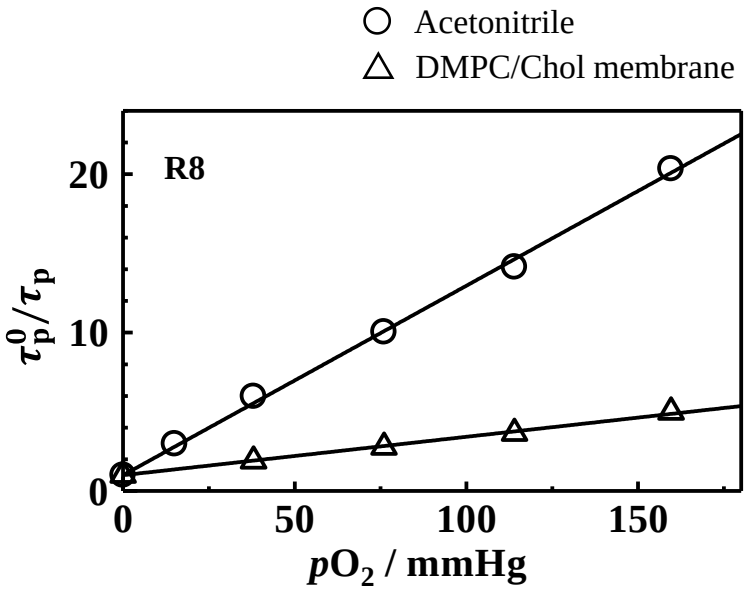

Figure 2-16. Plots of τ_p^0/τ_p vs pO_2 for **R8** in acetonitrile and DMPC/Chol membrane at 37 °C.

2-3-3 Cellular uptake and oxygen response in living cells

The cellular uptake efficiencies of **R8** and **R12** into HeLa cells were examined by obtaining emission images and comparing them with those obtained using C343-Pro_8-BTQphen, previously synthesized by our group [33]. HeLa cells were incubated with **R8** or **R12** (2 μM) for 2 h at 37 °C under 21% O_2 conditions. Figure 2-17A shows the emission microscopic images of HeLa cells obtained by observing the total emission at wavelengths above 455 nm. The emission images of **R8** and **R12** are much brighter than that of C343-Pro_8-BTQphen, suggesting that the cellular uptake efficiencies of **R8** and **R12** are greatly enhanced by introducing the oligoarginine linkers [37,45,46].

The cellular uptake efficiencies of the ratiometric probes were quantitatively compared by using a microplate reader to measure the emission intensities of the probes incorporated into HeLa cells. **R8**, **R12** and C343-Pro_8-BTQphen all contain the phosphor BTQphen, allowing to evaluate the probe concentration in cells by comparing the phosphorescence intensities of BTQphen monitored at 660 nm upon excitation at 500 nm, i.e., direct excitation of BTQphen. Figure 2-17B shows the emission intensities of HeLa cells incubated with each ratiometric probe (2 μM) for 2 h at 37 °C under an atmosphere of 21% O_2: the phosphorescence intensities of **R8** and **R12** are 5.5 and 7.2 times higher than that of C343-P_8-BTQphen, respectively. These results demonstrate that introduction of an oligoarginine peptide can significantly improve the cellular uptake efficiency of ratiometric probes.

Then, the intracellular localization of **R12** and **R8** in HeLa cells was examined by comparing the emission images of the ratiometric probes with those of organelle-specific trackers (Figure 2-18). Similar localization patterns were seen for the two probes. Here, HeLa cells were coincubated with **R8** or **R12** (1 μM) and a green-emitting mitochondria-

specific probe (MitoTracker Green, 0.1 μM) or lysosome-specific probe (LysoTracker Green, 0.1 μM) for 2 h. The merged images in Figure 2-18 show that the intracellular localization of **R8** and **R12** is distinct from both organelle-specific markers. Since lipophilic iridium(III) complexes with delocalized cationic charge are known to preferentially accumulate in mitochondria in response to negative intra-transmembrane potentials [47,48], the above results suggest that the intracellular localization of **R8** and **R12** is governed mainly by the oligoarginine linker rather than the 7DEAC and BTQphen moieties. Several small molecules bearing arginine-rich peptides are known to be taken up into endosomes in cells by direct penetration or endocytosis [45,49,50], suggesting the endosomal localization of **R8** and **R12**.

To reveal the accumulation process of **R12** to endosomes, the emission images of HeLa cells incubated with 2 μM **R12** were taken for different staining times (Figure 2-19). The emission image at 15 min exhibits notable emission from cell outlines, showing that the probe molecules are taken up into plasma membrane within 15 min. At 30 min, **R12** are partially internalized into cells to give a bright dots in the cytoplasm. After 2 h, almost all the probes are translocated from the cell membrane to the endosome-like region. To examine the stability of **R12** in cells, the HeLa cells were stained with 2 μM **R12** for 2 h under 21% O_2 condition, and then the medium was removed and the cells were washed gently with DMEM. Figure 2-20A shows emission spectra of **R12** immediately after washing (0 h) and at 4 h after washing. The sufficient emission signal could be obtained even 4 h after washing, and the normalized spectra are in good agreement (Figure 2-20B), suggesting that long-term monitoring of cellular respiration would be possible.

The cytotoxicity of different concentrations of **R8** and **R12** toward HeLa cells after 2 h incubation was examined using the WST assay (Figure 2-21). Cell viabilities greater

than 70% were obtained at **R8** and **R12** concentrations of 0.5 - 2 μM whereas incubation with 5 μM **R8** or **R12** resulted in markedly decreased cell viability, indicating significant cytotoxicity of **R8** and **R12**. However, cytotoxicity was negligibly small under typical experimental conditions (≤ 2 μM) used for live cell imaging and emission intensity measurements using a microplate reader.

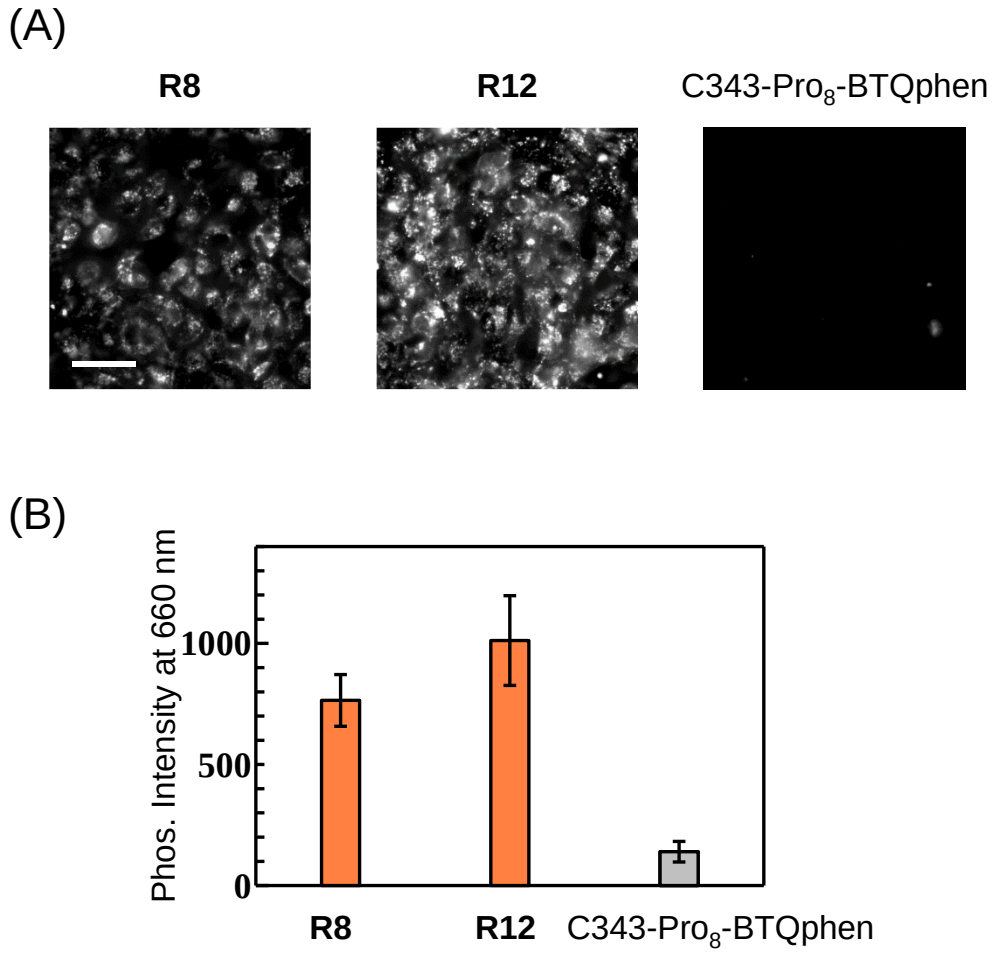

Figure 2-17. (A) Emission microscopic images of HeLa cells incubated with **R8**, **R12**, or C343-Pro_8-BTQphen (2 μM) for 2 h at 37 °C. Scale bar: 50 μm, excitation filter: 400-410 nm, emission filter: >455 nm. (B) Emission intensities of HeLa cells incubated with each ratiometric probe (2 μM) for 2 h at 37 °C. Excited at 500 nm, monitored at 660 nm.

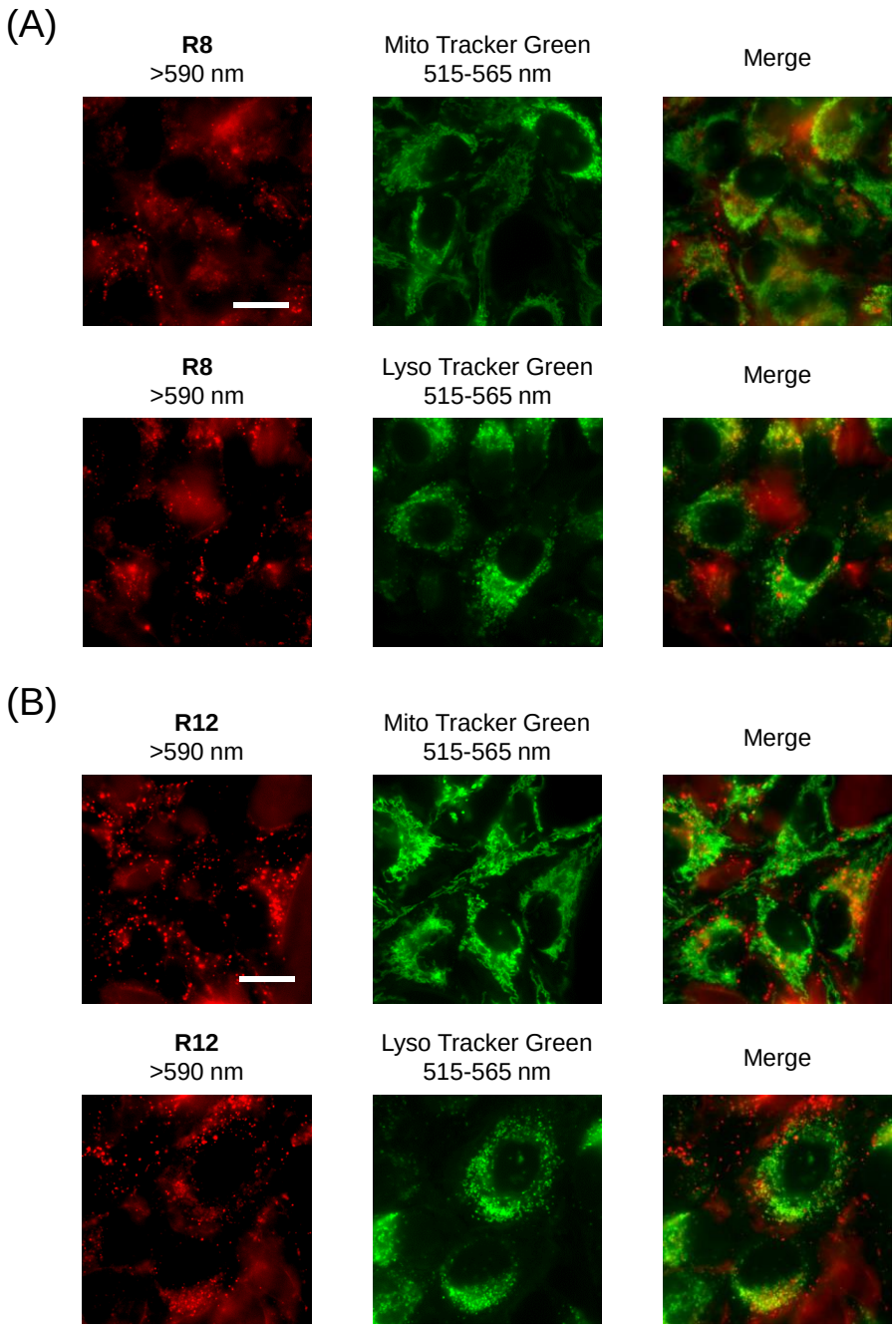

Figure 2-18. Emission images of HeLa cells upon coincubation with the ratiometric probe (A) **R8** or (B) **R12** (1 μM, 2 h) and MitoTracker Green (0.1 μM, 2 h) or LysoTracker Green at 37 °C. Scale bar: 20 μm.

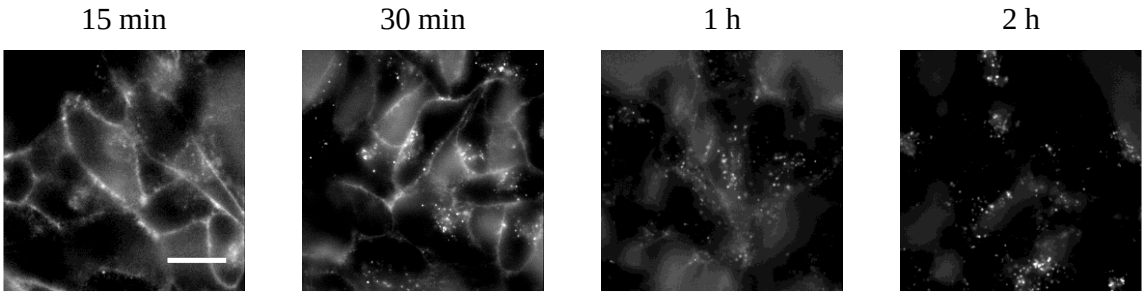

Figure 2-19. Emission microscopic images of HeLa cells incubated with **R12** (2 μM) for different staining time (15 min – 2 h) at 37 °C. Scale bar: 20 μm, excitation filter: 480-550 nm, emission filter: >590 nm.

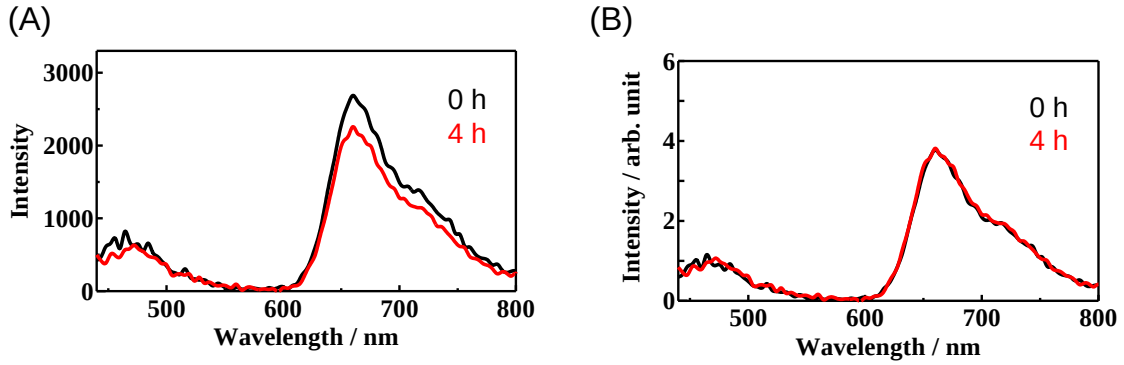

Figure 2-20. (A) Emission spectra of **R12** in HeLa cells at 0 h and 4 h after washing, and (B) their normalized spectra. The cells were incubated with **R12** (2 μM) for 2 h.

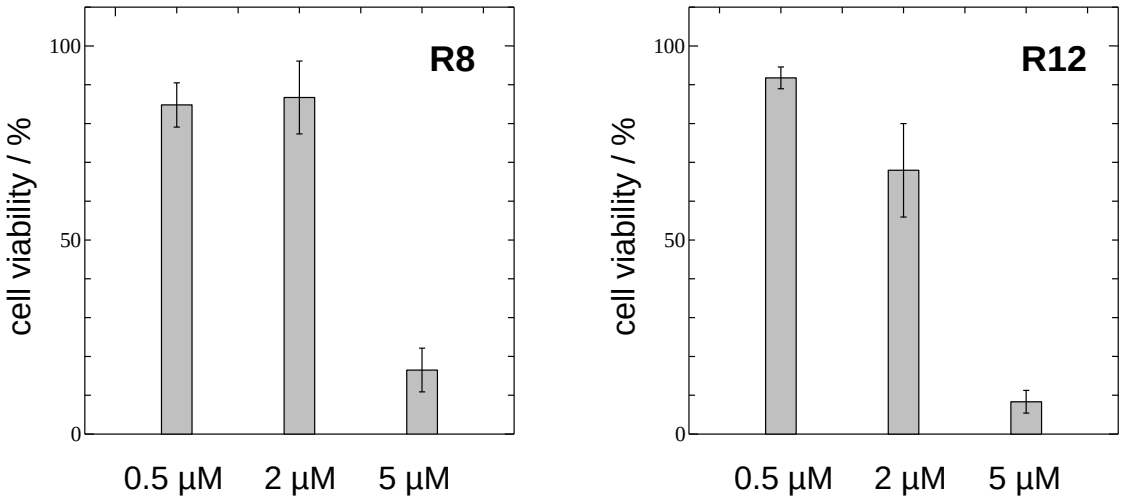

Figure 2-21. Cell viability of HeLa cells incubated with different concentrations of **R8** and **R12** (0.5, 2 and 5 µM) for 2 h.

The oxygen sensitivities of **R8** and **R12** incorporated into Hela cells were investigated, and then calibration curves of probes were constructed using a microplate reader. Both **R8** and **R12** exhibited dual emission, with maxima at 470 and 660 nm originating from the fluorescence of 7DEAC and the phosphorescence of BTQphen (Figure 2-22). The fluorescence intensity remained essentially constant when the oxygen partial pressure was changed from 19 to 160 mmHg, whereas the phosphorescence intensity decreased as the oxygen partial pressure increased. The value of R_I (= I_p/I_f) was calculated using the fluorescence intensity (I_f) at 470 nm and the phosphorescence intensity (I_p) at 660 nm obtained from the emission spectrum. The ratios of the R_I values of **R8** and **R12** under 2.5% (19 mmHg) O_2 to that under 21% (160 mmHg) O_2 (R_I(2.5%) / R_I(21%)) were 1.27 and 1.34, respectively. Furthermore, from the plot of $1/R_I$ against the oxygen partial pressure pO_2, the Stern-Volmer constant (K_{SV}) was determined by the following equation:

$$\frac{1}{R_I} = \frac{1}{R_I^0} + \frac{K_{SV}}{R_I^0} pO_2 \qquad (2\text{-}6)$$

The slope of the straight line and the intercept provided K_{SV} values of $(1.9 \pm 0.1) \times 10^{-3}$ $mmHg^{-1}$ and $(2.2 \pm 0.2) \times 10^{-3}$ $mmHg^{-1}$ for **R8** and **R12**, respectively. These values are much smaller than those obtained in MeCN (0.12 $mmHg^{-1}$) or DMPC membranes (2.8×10^{-2} $mmHg^{-1}$). The observed significant decrease in phosphorescence quenching of the ratiometric probes in cells is probably due to binding of the probe molecules to proteins in organelle membranes [18,48].

The photostability of probes is an important issue in ratiometric measurements because photobleaching of the fluorophore and/or phosphor greatly affects the K_{sv} value. **R8** and **R12** remain stable during long irradiation times, given the almost constant intensities of

7DEAC fluorescence during the calibration experiments (Figure 2-22A). These results suggest that there is negligible photobleaching of **R8** and **R12** in HeLa cells during measurements using a microplate reader.

In order to confirm the reliability of the oxygen partial pressure determined by the ratiometric method, the phosphorescence lifetime measurements of the ratiometric probes in HeLa cells were performed using a time-correlated single-photon counting system. The phosphorescence decay curves of **R8** and **R12** in HeLa cells cultured under 21% and 2.5% O_2 conditions are shown in Figure 2-23. The decay curves of **R8** and **R12** could be fitted to bi-exponential decay functions with the lifetimes τ_1 = 1.22 μs (A_1 = 0.19) and τ_2 = 3.70 μs (A_2 = 0.81), and τ_1 = 1.25 μs (A_1 = 0.28) and τ_2 = 3.79 μs (A_2 = 0.72), respectively, when pO_2 in the incubator was 21% (Table 2-3). The longer lifetime component suggests that part of the probe molecule is bound to proteins in the membrane, suppressing the interaction between probe with oxygen molecules. Intensity-averaged lifetimes $<\tau_p>_{int}$ for **R8** and **R12** was calculated to be 3.23 and 3.08 μs, respectively, under the 21% O_2 condition. The ratios τ(2.5%)/τ(21%) of the phosphorescence lifetimes of **R8** and **R12** in HeLa cells under 2.5% and 21% O_2 were determined to be 1.20 and 1.28, respectively, similar to the values (1.27 and 1.34) obtained by the ratiometric measurements. These results confirmed that the ratiometric O_2 measurements using **R8** and **R12** are applicable to evaluating intracellular O_2 levels.

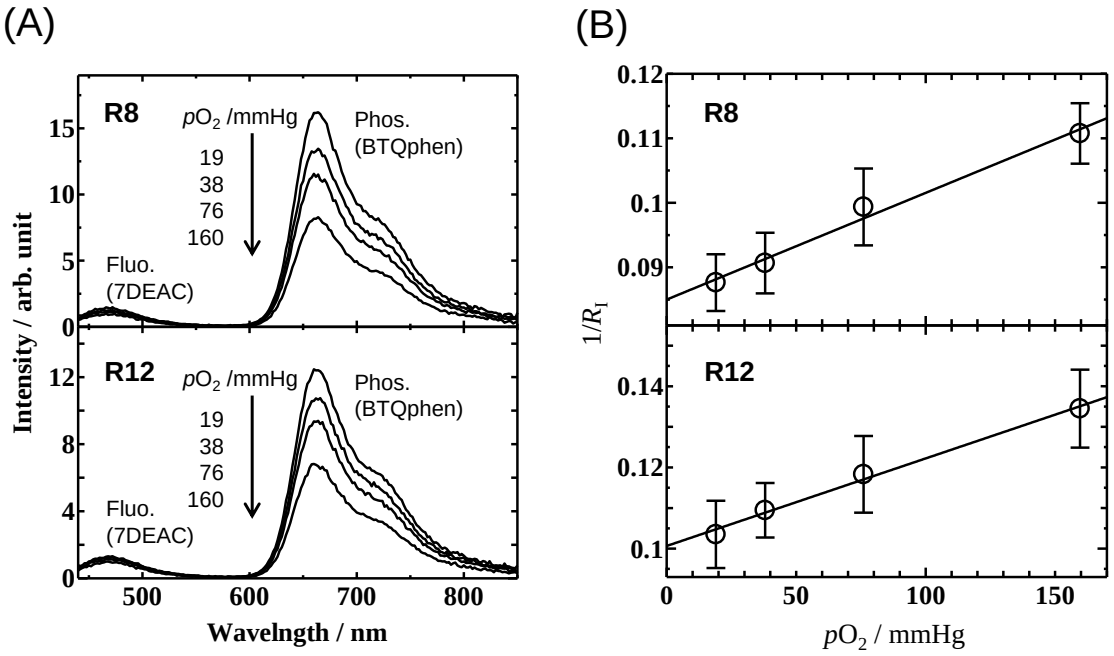

Figure 2-22. (A) Emission spectra of **R8** and **R12** in HeLa cells as a function of pO_2 measured with a microplate reader and (B) plots of $1/R_I$ vs. pO_2.

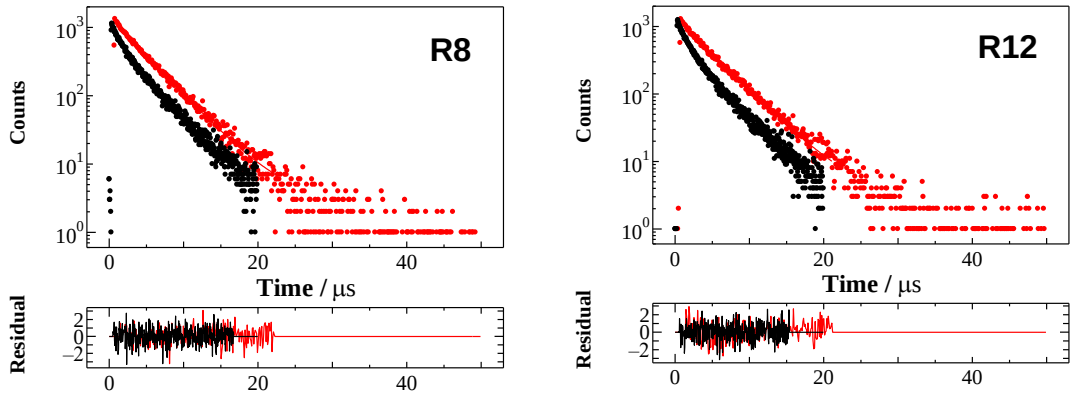

Figure 2-23. Phosphorescence decay curves of HeLa cells incubated with **R8** and **R12** (2 μM) for 2 h at 37 °C. Excited at 488 nm and monitored at 660 nm. red: 2.5% O_2, black: 21% O_2.

Table 2-3. Phosphorescence lifetimes (τ_p(21%) and τ_p(2.5%)) of HeLa cells incubated with **R8** and **R12** (2 μM) for 2 h at 37 °C under 21% and 2.5% O_2 conditions, and the intensity-average lifetime ($<\tau_p(21\%)>_{int}$) under 21 % O_2. Excited at 488nm, monitored at 660 nm.

Compound	τ_p(21%)	$<\tau_p(21\%)>_{int}$	τ_p(2.5%)	$\tau_p(2.5\%)/<\tau_p(21\%)>_{int}$
R8	1.22 (19%)	3.23	3.87	1.20
	3.70 (81%)			
R12	1.25 (28%)	3.08	3.94	1.28
	3.79 (72%)			

2-3-4 Ratiometric imaging of oxygen levels in living cells

Next, visualization of the oxygen levels of monolayer living cells was carried out using our ratiometric probes and a luminescence microscope equipped with a dual view simultaneous-imaging system. Figure 2-24A and B show luminescence microscopic images of HeLa cells incubated with **R12** (2 μM) for 2 h. The fluorescence intensity ($I_{460\text{-}510}$) from 7DEAC and the phosphorescence intensity ($I_{640\text{-}710}$) from BTQphen were measured using a band-pass filter (460-510 nm) and a second band-pass filter (640-710 nm), respectively. The ratiometric image (Figure 2-24C) was obtained as the ratio between the phosphorescence and fluorescence intensities ($I_{640\text{-}710}$/ $I_{460\text{-}510}$). In Figure 2-24C, the intensity ratio ($I_{640\text{-}710}$/ $I_{460\text{-}510}$) of each pixel is shown in pseudo color with 8 scales. In each ratio scale, the emission intensity is displayed with 32 scales. The fluorescence images of **R12** (Figure 2-24A) show almost the same intensity when the O_2 partial pressure is changed from 21% to 2.5% O_2. On the other hand, the phosphorescence intensity is higher under 2.5% O_2 compared to the 21% O_2 condition (Figure 2-24B). The ratiometric image (Figure 2-24C) under the 21% oxygen condition shows a blue-like color, while under the hypoxic condition (2.5 % O_2) the color is predominately orange-like (i.e., larger ratios), showing that the intracellular O_2 levels were lower. The observed heterogeneity in ratiometric readings is probably due to weakness of probe fluorescence which can be affected by autofluorescence of cells.

The usefulness of the developed ratiometric oxygen probes was confirmed by attempting to image the oxygen concentration gradient in monolayer cultured cells using ratiometric measurement. **R12** was added at a final concentration of 2 μM to the medium of HeLa cells growing on a flat bottom dish, then the cells were incubated for 2 h. After washing, a thin coverslip was gently placed on the monolayer cell cultures, as shown in

Figure 2-25A, then after 5 minutes the emission image was observed at the boundary region of the coverslip (Figure 2-25B). The oxygen supply to the top surface of cells in this region is cut off and thus there is likely an oxygen concentration gradient at the edge of the coverslip. The broken line in the ratiometric image shows the boundary of the coverslip. The upper side of the boundary line is outside the coverslip, and the lower side is the area covered by the coverslip [51,52]. The pseudo color of the cells in the ratiometric image changes from blue to red in the direction from the edge of the coverslip to the interior of the covered area, demonstrating that the oxygen level decreases in the direction from the edge to the interior. The ratios against the distance from the boundary of the coverslip were plotted using the data in Figure 2-25 (Figure 2-26A). The obtained ratio values ranged from 4 to 6 in the uncovered area, gradually increased towards the interior of the covered area, and stabilized at about 8 about 250 μm from the coverslip edge. These results demonstrate that the oxygen gradients of monolayer cultured HeLa cells can be determined by ratiometric emission measurements using **R12** (Figure 2-26B).

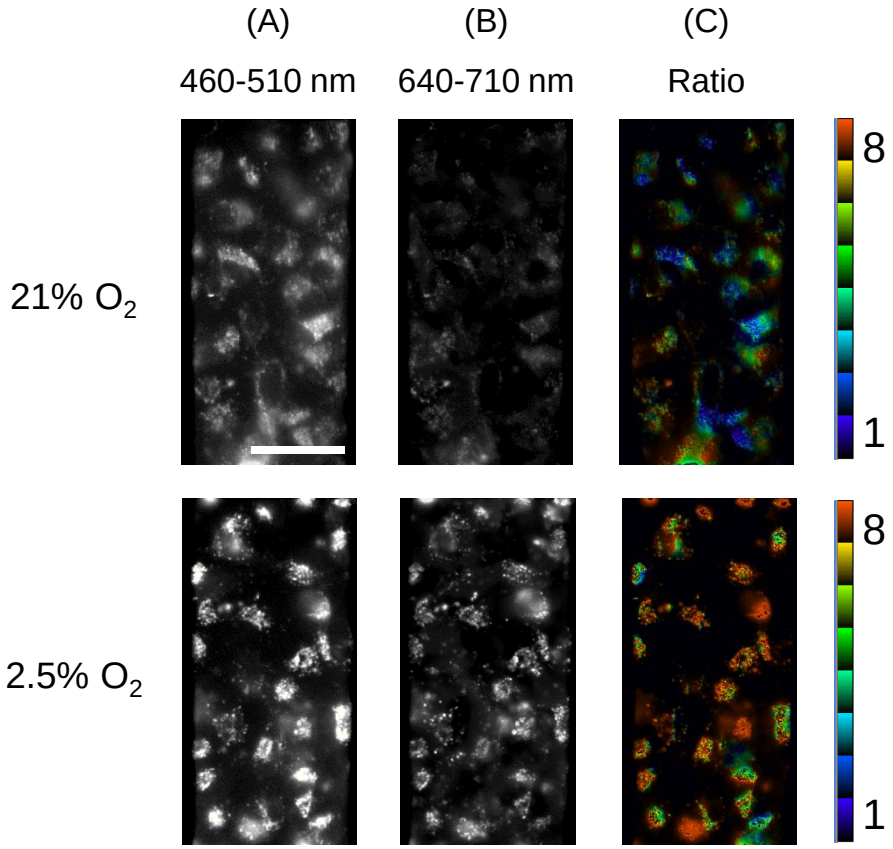

Figure 2-24. Emission microscopic images of HeLa cells incubated with **R12** (2 μM) for 2 h at 37 °C. Scale bar: 50 μm, excitation filter: 400-410 nm, emission filters: 460-510 nm for fluorescence (A) and >610 nm for phosphorescence (B). (C) is the ratio image.

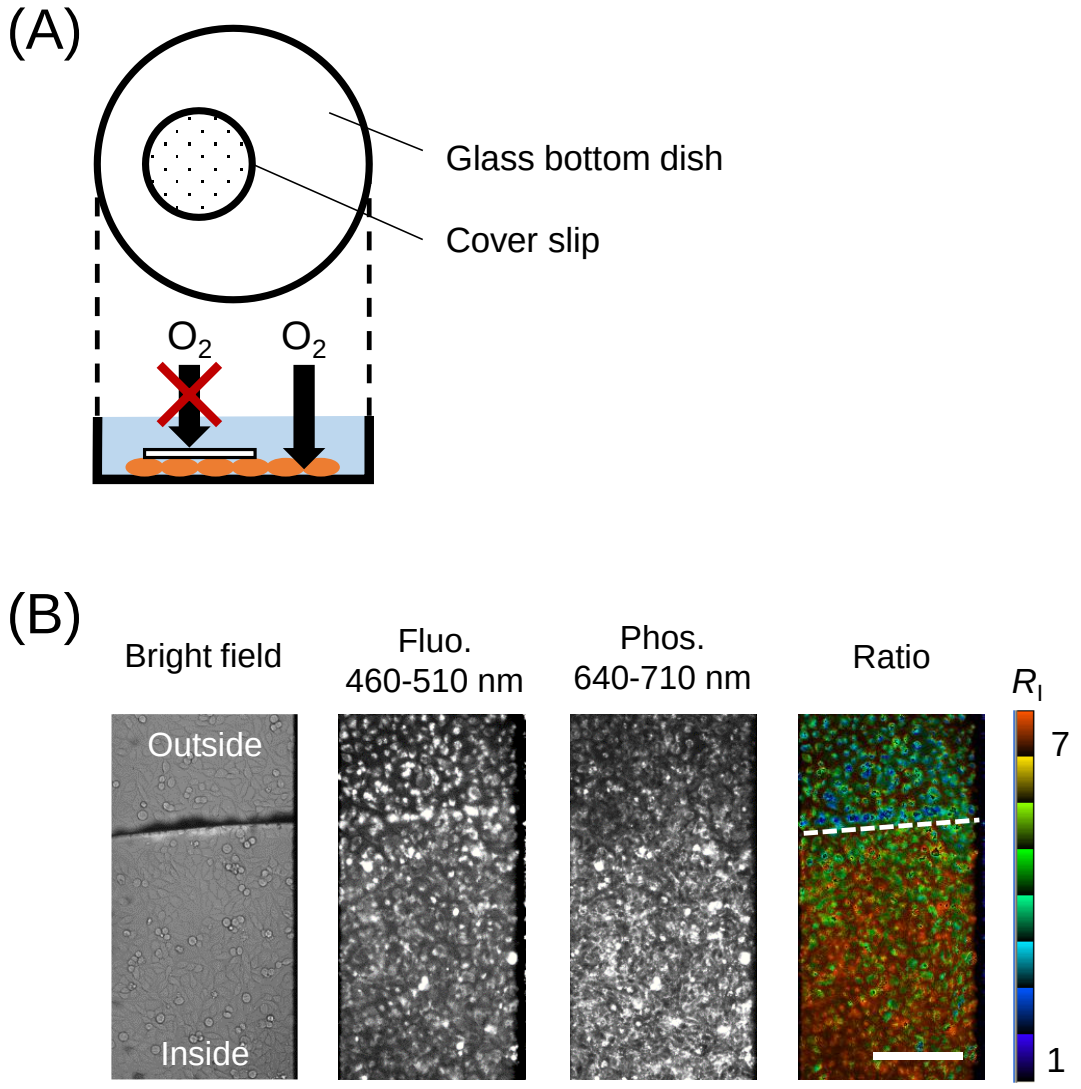

Figure 2-25. (A) Normal and hypoxic monolayer HeLa cells in a glass-bottomed dish. Hypoxic cells were produced by covering with a coverslip. (B) Emission microscopic images of HeLa cells in the vicinity of the coverslip edge. Excitation filter: 400-410 nm, emission filter: 460-510 nm (Fluo.), >610 nm (Phos.). Scale bar: 200 μm.

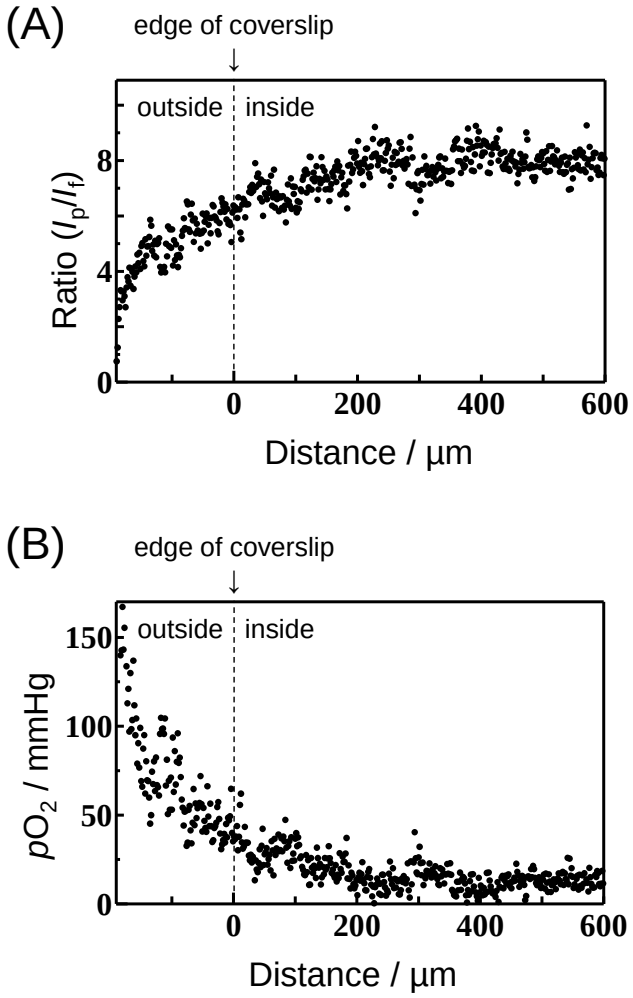

Figure 2-26. Variation of (A) ratio ($R_I = I_p/I_f$) and (B) pO_2 around the edge of the coverslip, calculated using the ratio image shown in Figure 2-24.

2-4 Conclusions

The new ratiometric O_2 probes **R8** and **R12** were designed and synthesized, in which a blue fluorescent 7DEAC molecule and a red phosphorescent BTQphen molecule are connected with an octa- or dodecaarginine peptide linker. The probes showed dual emission bands under 405 nm excitation in MeCN, lipid membrane, and in living cells due to intramolecular energy transfer from 7DEAC to BTQphen in the excited singlet states. The photophysical properties and O_2 sensitivities of **R8** and **R12** were examined in MeCN and in lipid bilayer membrane by emission spectra and lifetime measurements. The phosphorescence quenching rate constants of **R8** and **R12** in DMPC membrane were much smaller than in MeCN due to the reduced diffusion rates of O_2 and the probe molecules in the membrane. Compared to our previously synthesized ratiometric O_2 probe, **R8** and **R12** showed significantly higher cellular uptake efficiencies due to introduction of the oligoarginine linker. The ratiometric images obtained of **R12** internalized in living HeLa cells allowed us to image the O_2 gradient produced by placing a coverslip over a monolayer cell culture.

2-5 Synthetic procedures for ratiometric O_2 probes

7-Diethylaminocoumarin-3-carbocylic acid

7-Diethylaminocoumarin-3-carboxylic acid methyl ester [53] (3.88 g, 14.1 mmol) was dissolved in 40 mL of methanol, and the solution was refluxed. Adding 0.5 M NaOH (40 mL) to the solution provided a yellow solid. After cooling, 2 M HCl aqueous solution was added. An orange solid formed was collected by filtration and washed with aqueous 2 M HCl aqueous and water. The product 7-diethylaminocoumarin-3-carboxylic acid was obtained as an orange solid (2.82 g, 73%).

^{1}H NMR (400 MHz, $CDCl_3$) δ 8.64 (s, 1H), 7.44 (d, 1H, J = 9.0 Hz), 6.70 (dd, 1H, J = 9.0 Hz, 2.4 Hz), 6.52 (d, 1H, J = 2.4 Hz), 3.48 (q, 4H, J = 7.2 Hz), 1.25 (t, 6H, J = 7.2 Hz), ESI-MS (positive) : calcd. for $C_{14}H_{15}NO_4$ ($[M+H]^+$): 261.1, found: 262.2.

BTQphen (reference compound for phosphor)

2-(Benzo[*b*]thiophen-2-yl)quinoline (1.90 g, 7.2 mmol) and $IrCl_3 \cdot 3H_2O$ (1.24 g, 3.5 mmol) were dissolved in 2-ethoxyethanol (90 mL) and distilled water (35 mL) and then the solution was heated at reflux for 15 h. After cooling, the precipitate formed was filtered to give a chloro-briged dimer of BTQ, which was washed thoroughly with methanol and *n*-hexane. *tert*-Butyl 4-(1,10-phenanthrolin-5-yl)piperazine-1-carboxylate (397 mg, 1.1 mmol) and chloro-bridged dimer of BTQ (752 mg, 0.5 mmol,) were dissolved in tetrahydrofuran (50 mL) and methanol (50 mL), then the solution was refluxed at 6 h. After cooling, KPF_6 (376 mg, 2.0 mmol) was added to the solution and stirred at 1h. The solution was evaporated to dryness under reduced pressure. The crude product was purified by aminopropyl-functionalized silica-gel column chromatography

using chloroform as eluent. The product (BTQphen-pipe-Boc) was obtained as red powder (731 mg, 0.60 mmol, 60%).

The deprotection cocktail (TFA/Triisopropylsilane (TIPS) /H_2O 95:2.5:2.5, 1 mL) was added to BTQphen-pipe-Boc (516 mg, 0.42 mmol) in a centrifuge tube. After 2 h at room temperature, a red solid was precipitated by addition of the cool diethyl ether. The precipitate was centrifuged (3500 rpm, 5 min), then diethyl ether was removed by decantation. This operation was repeated twice. The product (BTQphen) was obtained as red powder (444 mg, 0.36 mol, 85%).

^{1}H NMR (400 MHz, DMSO-D6) δ 8.92 (br, 2H), 8.77 (d, *J* = 8.5 Hz, 1H), 8.68 (d, *J* = 5.3 Hz, 1H), 8.56 (d, *J* = 8.5 Hz, 1H), 8.52-8.41 (m, 3H), 8.20 (q, *J* = 8.6 Hz, 2H), 8.08 (dd, *J* = 8.5, 5.3 Hz, 1H), 8.05-7.92 (m, 3H), 7.76 (dd, *J* = 11.3, 8.1 Hz, 2H), 7.59 (s, 1H), 7.20-7.10 (m, 4H), 6.93 (d, *J* = 8.9 Hz, 1H), 6.78-6.60 (m, 5H), 6.21 (dd, *J* = 13.3, 8.2 Hz, 2H), 3.53 (br, 4H), 3.13 (br, 4H), ESI-MS (positive) : calcd. for $C_{50}H_{36}IrN_6S_2$ (M^+): 977.21, found: 977.2.

7DEAC-[R(Pbf)]$_8$-OH

Peptides were synthesized by using a fully automated microwave peptide synthesizer (Biotage Initiator+ Alstra) based on solid-phase synthesis. H-R(Pbf)-2-Chlorotrityl resin (BeadTech, 1.1 g, 0.38 mmol/g loading) was used as a solid support. For the coupling of an amino acid, 0.5 M Fmoc-Arg-OH in DMF, 0.6 M HBTU in DMF, 0.5 M HOBt in DMF and 2.0 M *N*,*N*-diisopropylethylamine (DIPEA) in NMP were added into reaction vial (3 eq., 3 eq., 3 eq. and 6 eq. respectively). The reaction mixture was stirred for 1 h at room temperature. Deprotection of Fmoc group was performed in 2% DBU in DMF for 5 min at room temperature. For complete deprotection, the reaction was carried out again under

the same conditions for 10 minutes. 7 standard cycles of coupling-deprotection were carried out. 7DEAC (110 mg, 0.42 mmol), HATU (190 mg, 0.05 mmol) and DIEA (0.34 mL, 2.0 mmol) were dissolved in DMF (6 mL), and then the solution was added into the reaction vial. The solution was stirred for 24 h at room temperature. After the coupling, the solution was drained, and the resin was rinsed with DMF to remove unreacted 7DEAC and HATU. For cleaving peptide from resin, 1% TFA in DCM (10 mL) was added into the vial, and the solution was stirred for 90 min at room temperature. The reaction mixture is filtered and filtrate evaporated under vacuum. The crude peptide was dissolved in acetonitrile, and distilled water was added. The precipitate was centrifuged (3500 rpm, 5 min), then water was removed by decantation. This operation was repeated twice. Any remaining water was removed from vessel by vacuum freezing and the product (7DEAC-[R(Pbf)]$_8$-OH) was obtained as yellow powder (590 mg, 40%).

ESI-MS(positive): calcd. for $C_{166}H_{239}N_{33}O_{36}S_8$ ($[M+2H]^{2+}$): 1764.3, found: 1764.7.

7DEAC-[R(Pbf)]$_8$-BTQphen

7DEAC-[R(Pbf)]$_8$-OH (353 mg, 0.10 mmol), BTQphen (136 mg, 0.11 mmol), HOBt (30 mg, 0.22 mmol) and HATU (190 mg, 0.5 mmol) were dissolved in anhydrous DMF (2 mL), then DIPEA (0.34 mL, 2.0 mmol) was added. This solution was stirred at room temperature for 24 h under N_2 gas. The distilled water was added into the reaction mixture. The precipitate was centrifuged (3500 rpm, 5 min), then water was removed by decantation. This operation was repeated twice. Any remaining water was removed from vessel by vacuum freezing and the product (7DEAC-[R(Pbf)]$_8$-BTQphen) was obtained as red powder (455 mg, 98%).

ESI-MS(positive): calcd. for $C_{216}H_{273}IrN_{39}O_{35}S_{10}$ ($[M-PF_6+2H]^{3+}$): 1496.3, found 1496.5.

7DEAC-R$_8$-BTQphen

The deprotection cocktail (TFA/TIPS/H_2O 95:2.5:2.5) (1 mL) was added to 7DEAC-[R(Pbf)]$_8$-BTQphen (224 mg, 0.044 mmol) in a centrifuge tube. After 2 h at room temperature, an orange solid was precipitated by addition of the cool diethyl ether. The precipitate was centrifuged (3500 rpm, 5 min), then diethyl ether was removed by decantation. This operation was repeated twice. Diethyl ether was removed by decantation, and then the orange solid was dried in a vacuum desiccator. The crude product was obtained as orange powder (93 mg, 58%). A part of the crude product was purified by using a reverse-phase HPLC system (Shimadzu) and the following condition: column, YMC-Actus Triart C18 (250×20 mm, YMC); eluent, 40-100% acetonitrile aq. containing 0.1% TFA; flow rate, 0.5 mL/min. The main peak fraction was collected and purified water was added. The aqueous solution was dried by vacuum freezing to afford the product (7DEAC-R$_8$-BTQphen) as orange powder (25 mg, 6.8 μmol).

ESI-MS(positive): calcd. for $C_{112}H_{145}IrN_{39}O_{11}S_2$ ($[M-PF_6+H]^{2+}$): 1234.6, found: 1234.5.

MALDI-TOF MS: calcd. for $C_{112}H_{145}IrN_{39}O_{11}S_2$ ($[M-PF^6]^+$): 2469.11, found: 2469.57.

7DEAC-R$_8$-OH (reference compound for fluorophore)

The deprotection cocktail (TFA/TIPS/H_2O 95:2.5:2.5) (1 mL) was added to 7DEAC-[R(Pbf)]$_8$-OH (224 mg, 0.044 mmol) in a centrifuge tube. After 2 h at room temperature, an orange solid was precipitated by addition of the cool diethyl ether. The precipitate was centrifuged (3500 rpm, 5 min), then diethyl ether was removed by decantation. This operation was repeated twice. Diethyl ether was removed by decantation, and then the yellow solid was dried in a vacuum desiccator. A part of the crude product was purified by using a reverse-phase HPLC system (Shimadzu) with the following condition: column,

YMC-Actus Triart C18 (250×20 mm, YMC); eluent, 40%-100% acetonitrile aq. containing 0.1% TFA; flow rate, 0.5 mL/min. The product (7DEAC-R_8-OH) was obtained as yellow powder (15 mg, 9.9 μmol).

ESI-MS(positive): calcd. for $C_{62}H_{111}N_{33}O_{12}$ ($[M+3H]^{3+}$) 504.6, found: 504.5. MALDI-TOF MS: calcd. for $C_{62}H_{111}N_{33}O_{12}$ ($[M+H]^{+}$) 1509.91, found: 1511.89.

7DEAC-[R(Pbf)]$_{12}$-OH

Peptides were synthesized by using a fully automated microwave peptide synthesizer (Biotage Initiator+ Alstra) based on solid-phase synthesis. H-R(Pbf)-2-Chlorotrityl resin (BeadTech, 1.03 g, 0.31 mmol/g loading) was used as a solid support. For the coupling of an amino acid, 0.5 M Fmoc-Arg-OH in DMF, 0.6 M HBTU in DMF, 0.5 M HOBt in DMF and 2.0 M *N*,*N*-diisopropylethylamine (DIPEA) in NMP were added into reaction vial (3 eq., 3 eq., 3 eq. and 6 eq. respectively). The reaction mixture was stirred for 1 h at room temperature. Deprotection of Fmoc group was performed in 2% DBU in DMF for 5 min at room temperature. For complete deprotection, the reaction was carried out again under the same conditions for 10 minutes. 11 standard cycles of coupling-deprotection were carried out. 7DEAC (110 mg, 0.42 mmol), HATU (190 mg, 0.05 mmol) and DIEA (0.34 mL, 2.0 mmol) were dissolved in DMF (6 mL), and then the solution was added into the reaction vial. The solution was stirred for 24 h at room temperature. After the coupling, the solution was drained, and the resin was rinsed with DMF to remove unreacted 7DEAC and HATU. For cleaving peptide from resin, 1% TFA in DCM (10 mL) was added into the vial, and the solution was stirred for 90 min at room temperature. The reaction mixture is filtered and the filtrate was evaporated under vacuum. The crude peptide was dissolved in acetonitrile, and distilled water was added. The precipitate was

centrifuged (3500 rpm, 5 min), then water was removed by decantation. This operation was repeated twice. All remaining water was removed from vessel by vacuum freezing and the product (7DEAC-[R(Pbf)]$_{12}$-OH) was obtained as yellow powder (1.00 g, 63%).
ESI-MS(positive): calcd. for $C_{242}H_{351}N_{49}O_{52}S_{12}$ ($[M+3H]^{3+}$): 1720.8, found: 1721.4.

7DEAC-[R(Pbf)]$_{12}$-BTQphen

7DEAC-[R(Pbf)]$_{12}$-OH (276 mg, 0.05 mmol), BTQphen (56 mg, 0.05 mmol) and HATU (190 mg, 0.5 mmol) were dissolved in anhydrous DMF (2 mL), then DIPEA (0.34 mL, 2.0 mmol) was added. This solution was stirred at room temperature for 24 h under N_2 gas. The distilled water was added into the reaction mixture. The precipitate was centrifuged (3500 rpm, 5 min), then water was removed by decantation. This operation was repeated twice. All remaining water was removed from vessel by vacuum freezing and the product (7DEAC-[R(Pbf)]$_{12}$-BTQphen) was obtained as red powder (332 mg, 106%).
ESI-MS(positive): calcd. for $C_{292}H_{385}IrN_{55}O_{51}S_{14}$ ($[M^{-}PF_6^{+}3H]^{4+}$): 1530.6, found 1531.0

7DEAC-R$_{12}$-OH (reference compound for fluorophore)

The deprotection cocktail (TFA/TIPS/H_2O 95:2.5:2.5) (1 mL) was added to 7DEAC-[R(Pbf)]$_{12}$-OH (197 mg, 0.038 mmol) in a centrifuge tube. After 2 h at room temperature, an orange solid was precipitated by addition of the cool diethyl ether. The precipitate was centrifuged (3500 rpm, 5 min), then diethyl ether was removed by decantation. This operation was repeated twice. Diethyl ether was removed by decantation, and then the yellow solid was dried in a vacuum desiccator. A part of the crude product was purified by using a reverse-phase HPLC system (Shimadzu) with the following condition: column,

YMC-Actus Triart C18 (250×20 mm, YMC); eluent, 40%-100% acetonitrile aq. containing 0.1% TFA; flow rate, 0.5 mL/min. The product (7DEAC-R_8-OH) was obtained as yellow powder (15 mg, 7.0 μmol).

ESI-MS(positive): calcd. for $C_{86}H_{159}N_{49}O_{16}$ ($[M+3H]^{3+}$) 712.3, found: 712.4. MALDI-TOF MS: calcd. for $C_{86}H_{159}N_{49}O_{16}$ ($[M-PF_6+H]^{+}$) 2134.31, found: 2135.00.

7DEAC-R_{12}-BTQphen

The deprotection cocktail (TFA/TIPS/H_2O 95:2.5:2.5) (1 mL) was added to 7DEAC-$[R(Pbf)]_{12}$-BTQphen (303 mg, 0.048 mmol) in a vessel. After being stirred for 2 h at room temperature, an orange solid was precipitated by addition of the cool diethyl ether. The precipitate was centrifuged (3500 rpm, 5 min), then diethyl ether was removed. This operation was repeated twice. Diethyl ether was removed, and then the orange solid was dried in a desiccator. A part of the crude product was purified by using a reverse-phase HPLC system (Shimadzu) with the following condition: column, YMC-Actus Triart C18 (250×20 mm, YMC); eluent, 40-100% acetonitrile aq. containing 0.1% TFA; flow rate, 0.5 mL/min. The main peak fraction was collected and purified water was added. The aqueous solution was dried by vacuum freezing to afford the product (7DEAC-R_{12}-BTQphen) as orange powder (20.5 mg, 4.5 μmol).

ESI-MS(positive): calcd. for $C_{136}H_{193}IrN_{55}O_{15}S_2$ ($[M-PF_6+2H]^{3+}$): 1032.2, found: 1032.1. MALDI-TOF MS: calcd. for $C_{136}H_{193}IrN_{55}O_{15}S_2$ ($[M-PF_6]^{+}$) 3093.51, found: 3092.86.

References

[1] M. D. Brand and D. G. Nicholls, *Biochem. J.*, **2011**, *437*, 297–312.

[2] G. L. Semenza, *Cell*, **2012**, *148*, 399–408.

[3] P. V Prasad, R. R. Edelman and F. H. Epstein, *Circulation*, **1996**, *94*, 3271–3275.

[4] T. Kawakami, I. Mimura, K. Shoji, T. Tanaka and M. Nangaku, *Kidney Int. Suppl.*, **2014**, *4*, 107–112.

[5] J. M. Vanderkooi, G. Maniara, J. Green and F. Wilson, *J. Biol. Chem.*, **1987**, *262*, 5476–5482.

[6] W. L. Rumsey, J. M. Vanderkooi and D. F. Wilson, *Science*, **1988**, *241*, 1649–1651.

[7] D. B. Papkovsky and R. I. Dmitriev, *Chem. Soc. Rev.*, **2013**, *42*, 8700–8732.

[8] X. Wang and O. S. Wolfbeis, *Chem. Soc. Rev.*, **2014**, *43*, 3666–3761.

[9] E. Roussakis, Z. Li, A. J. Nichols and C. L. Evans, *Angew. Chemie. Int. Ed.*, **2015**, *54*, 8340–8362.

[10] T. Yoshihara, Y. Hirakawa, M. Hosaka, M. Nangaku and S. Tobita, *J. Photochem. Photobiol. C Photochem. Rev.*, **2017**, *30*, 71–95.

[11] J. Liu, W. Bu and J. Shi, *Chem. Rev.*, **2017**, *117*, 6160–6224.

[12] T. V. Esipova, M. J. P. Barrett, E. Erlebach, A. E. Masunov, B. Weber and S. A. Vinogradov, *Cell Metab.*, **2019**, *29*, 1–19.

[13] E. Roussakis, J. A. Spencer, C. P. Lin and S. A. Vinogradov, *Anal. Chem.*, **2014**, *86*, 5937–5945.

[14] J. A. Spencer, F. Ferraro, E. Roussakis, A. Klein, J. Wu, J. M. Runnels, W. Zaher, L. J. Mortensen, C. Alt, R. Turcotte, R. Yusuf, D. Côté, S. A. Vinogradov, D. T. Scadden and C. P. Lin, *Nature*, **2014**, *508*, 269–273.

[15] I. A. Okkelman, T. Foley, D. B. Papkovsky and R. I. Dmitriev, *Biomaterials*, **2017**, *146*, 86–96.

[16] D. Sud and M.-A. Mycek, *J. Biomed. Opt.*, **2009**, *14*, 020506.

[17] A. Martin, A. Byrne, C. S. Burke, R. J. Forster and T. E. Keyes, *J. Am. Chem. Soc.*, **2014**, *136*, 15300–15309.

[18] T. Yoshihara, M. Hosaka, M. Terata, K. Ichikawa, S. Murayama, A. Tanaka, M. Mori, H. Itabashi, T. Takeuchi and S. Tobita, *Anal. Chem.*, **2015**, *87*, 2710–2717.

[19] Y. Hirakawa, T. Yoshihara, M. Kamiya, I. Mimura, D. Fujikura, T. Masuda, R. Kikuchi, I. Takahashi, Y. Urano, S. Tobita and M. Nangaku, *Sci. Rep.*, **2015**, *5*, 1–7.

[20] S. Tobita and T. Yoshihara, *Curr. Opin. Chem. Biol.*, **2016**, *33*, 39–45.

[21] J. R. Shewring, A. J. Cankut, L. K. McKenzie, B. J. Crowston, S. W. Botchway, J. A. Weinstein, E. Edwards and M. D. Ward, *Inorg. Chem.*, **2017**, *56*, 15259–15270.

[22] Y. Hirakawa, K. Mizukami, T. Yoshihara, I. Takahashi, P. Khulan, T. Honda, I. Mimura, T. Tanaka, S. Tobita and M. Nangaku, *Kidney Int.*, **2018**, *93*, 1483–1489.

[23] H. Xu, J. W. Aylott, R. Kopelman, T. J. Miller and M. A. Philbert, *Anal. Chem.*, **2001**, *73*, 4124–4133.

[24] Y. E. L. Koo, Y. Cao, R. Kopelman, S. M. Koo, M. Brasuel and M. A. Philbert, *Anal. Chem.*, **2004**, *76*, 2498–2505.

[25] C. Sci, X. Wang, H. H. Gorris, J. A. Stolwijk, R. J. Meier, D. B. M. Groegel, J. Wegener and O. S. Wolfbeis, *Chem. Sci.*, **2011**, *2*, 901–906.

[26] A. V. Kondrashina, R. I. Dmitriev, S. M. Borisov, I. Klimant, I. O'Brien, Y. M. Nolan, A. V. Zhdanov and D. B. Papkovsky, *Adv. Funct. Mater.*, **2012**, *22*, 4931–4939.

[27] R. I. Dmitriev, S. M. Borisov, H. Düssmann, S. Sun, B. J. Müller, J. Prehn, V. P. Baklaushev, I. Klimant and D. B. Papkovsky, *ACS Nano*, **2015**, *9*, 5275–5288.

[28] Q. Zhao, X. Zhou, T. Cao, K. Y. Zhang, L. Yang, S. Liu, H. Liang, H. Yang, F. Li and W. Huang, *Chem. Sci.*, **2015**, *6*, 1825–1831.

[29] S. Lu, W. Xu, J. Zhang, Y. Chen, L. Xie, Q. Yao, Y. Jiang, Y. Wang and X. Chen, *Biosens. Bioelectron.*, **2016**, *86*, 176–184.

[30] Q. Zhao, T. Pan, G. Xiang, Z. Mei, J. Jiang, G. Li, X. Zou, M. Chen, D. Sun, S. Jiang and Y. Tian, *Sensors Actuators, B Chem.*, **2018**, *273*, 242–252.

[31] H. Düssmann, S. Perez-Alvarez, U. Anilkumar, D. B. Papkovsky and J. H. Prehn, *Cell Death Dis.*, **2017**, *8*, e2853.

[32] T. Yoshihara, Y. Yamaguchi, M. Hosaka, T. Takeuchi and S. Tobita, *Angew. Chem. Int. Ed. Ed.*, **2012**, *51*, 4148–4151.

[33] T. Yoshihara, S. Murayama and S. Tobita, *Sensors*, **2015**, *15*, 13503–13521.

[34] D. Hara, H. Komatsu, A. Son, S. I. Nishimoto and K. Tanabe, *Bioconjug. Chem.*, **2015**, *26*, 645–649.

[35] K. Y. Zhang, P. Gao, G. Sun, T. Zhang, X. Li, S. Liu, Q. Zhao, K. K.-W. Lo and W. Huang, *J. Am. Chem. Soc.*, **2018**, *140*, 7827–7834.

[36] H. Bian, X. Song, N. Li, H. Man and Y. Xiao, *J. Mater. Chem. B*, **2018**, *6*, 1699–1705.

[37] S. Futaki, T. Suzuki, W. Ohashi, T. Yagami, S. Tanaka, K. Ueda and Y. Sugiura, *J. Biol. Chem.*, **2001**, *276*, 5836–5840.

[38] T. Yoshihara, H. Shimada, H. Shizuka and S. Tobita, *Phys. Chem. Chem. Phys.*, **2001**, *3*, 4972–4978.

[39] K. Suzuki, A. Kobayashi, S. Kaneko, K. Takehira, T. Yoshihara, H. Ishida, Y. Shiina, S. Oishi and S. Tobita, *Phys. Chem. Chem. Phys.*, **2009**, *11*, 9850–9860.

[40] S. Batzri and E. D. Korn, *Biochim. Biophys. Acta - Biomembr.*, **1973**, *298*, 1015–1019.

[41] H. Yersin, *Highly Efficient OLEDs with Phosphorescent Matrerials*, Wiley-VCH, Weinheim, 2008.

[42] A. Endo, K. Suzuki, T. Yoshihara, S. Tobita, M. Yahiro and C. Adachi, *Chem. Phys. Lett.*, **2008**, *460*, 155–157.

[43] T. Murase, T. Yoshihara and S. Tobita, *Bull. Chem. Soc. Jpn.*, **2013**, *519*, 510–519.

[44] R. Battino, F. D. Evans and W. F. Danforth, *J. Am. Oil Chem. Soc.*, **1968**, *45*, 830–833.

[45] R. I. Dmitriev, H. M. Ropiak, G. V. Ponomarev, D. V. Yashunsky and D. B. Papkovsky, *Bioconjug. Chem.*, **2011**, *22*, 2507–2518.

[46] C. Dolan, R. D. Moriarty, E. Lestini, M. Devocelle, R. J. Forster and T. E. Keyes, *J. Inorg. Biochem.*, **2013**, *119*, 65–74.

[47] T. Murase, T. Yoshihara and S. Tobita, *Chem. Lett.*, **2012**, *41*, 262–263.

[48] T. Yoshihara, S. Murayama, T. Masuda, T. Kikuchi, K. Yoshida, M. Hosaka and S. Tobita, *J. Photochem. Photobiol. A Chem.*, **2015**, *299*, 172–182.

[49] K. Koren, R. I. Dmitriev, S. M. Borisov, D. B. Papkovsky and I. Klimant, *ChemBioChem*, **2012**, *13*, 1184–1190.

[50] Y. Choi, J. R. McCarthy, R. Weissleder and C. H. Tung, *ChemMedChem*, **2006**, *1*, 458–463.

[51] E. Takahashi and M. Sato, *Am. J. Physiol. Cell Physiol.*, **2010**, *299*, C1318–C1323.

[52] H. Akiyama, I. Takahashi, Y. Shimoda, R. Mukai, T. Yoshihara and S. Tobita, *Photochem. Photobiol. Sci.*, **2018**, *17*, 846–853.

[53] T. Berthelot, J. C. Talbot, G. Laïn, G. Déleris and L. Latxague, *J. Pept. Sci.*, **2005**, *11*, 153–160.

Chapter 3

Phosphorescent Ir(III) Complexes with Arginine Peptide for Microvascular Imaging

3-1 Introduction

Blood vessels form a network throughout the body, carrying blood that delivers oxygen and nutrients to tissues and removing CO_2 and waste products. Disruption of the vascular system is closely associated with various diseases. For example, in cancer and diabetic retinopathy, abnormal angiogenesis results in an immature and heterogeneous vascular network [1]. Therefore, the visualization of vascular networks in tissues is highly important for understanding vascular diseases.

Many imaging techniques, such as magnetic resonance imaging (MRI) [2], computed tomography (CT) [3,4], positron emission tomography (PET) [5], photoacoustic imaging [6] and optical imaging [7] have been used to visualize the network of blood vessels in tissues and bodies. Fluorescence imaging based on confocal laser scanning microscopy and two-photon microscopy [8,9] offers several advantages over these other techniques, including high spatial resolution, good sensitivity, and the possibility of multicolor imaging of blood vessels and tissue cells, although the penetration depth in tissues is limited and the field-of-view is small. To overcome these issues, various second near-infrared (NIR-II, 1100-1700 nm) compounds [10], and a light-sheet microscope [11], have recently been developed.

To visualize the network of blood vessels based on fluorescence imaging, many fluorescent vasculature probes have been developed using biocompatible polymers, proteins, and nanoparticles [12–14]. Fluorescent dextrans, in which fluorescent dyes such as coumarin [15], fluorescein [16], or rhodamine derivatives [17] are covalently bonded to dextran with a molecular weight of 70 kDa or more, are widely used as blood vessel imaging reagents. These probes have a large molecular weight, similar to that of serum albumin, and thus circulate in the bloodstream for a long time without being filtered by

the glomeruli in the kidneys. Another approach is to conjugate a fluorophore to *Lycopersicon esculentum* (tomato) lectin [18,19], which has selective affinity to *N*-acetyl-D-glucosamine, and to a fluorescent antibody [20] with affinity to CD31, a typical endothelial marker. This approach allows the visualization of blood vessels by the binding of tagged lectin and antibody to vascular endothelial cells. Although these fluorescent probes allow visualization of the vascular network in tissues, it is often difficult to clearly distinguish between the autofluorescence of tissue cells and probe signals. Furthermore, fluorescent dextrans have much larger molecular weights than small-molecule probes and thus a larger amount (by mass) must be administered to visualize the vascular network in tissues.

The optical oxygen probes based on Ir(III) complexes have been developing for *in vivo* oxygen measurements [21]. The oxygen status of tissue cells is maintained by the balance of oxygen supply by the blood and its consumption in cells. Thus, imaging the vascular network is important for understanding oxygen distribution throughout tissues. The hydrophilic Ir(III) complexes bearing a biocompatible hydrophilic unit, polyethylene glycol were recently developed for intravascular O_2 imaging in living tissues [22]. However, these complexes are transferred to the urinary space within 1 hour of administration to mice by filtration by the glomeruli in the kidneys. Vascular imaging probes that stain vessel walls are required for long observation periods. During our previous work, on the development of a ratiometric oxygen probe [23], it was found that probes incorporating oligoarginine peptides administered intravenously to mice selectively stain the vascular endothelium, likely due to binding of the oligoarginine peptide to proteoglycans on the surface of vascular endothelial cells [24,25].

In this chapter, hydrophilic Ir(III) complexes conjugated with arginine peptides of different lengths (BTQ-R_n (n = 4, 8, 12, 16), Figure 3-1) were synthesized for *in vivo* vascular imaging. The usefulness of BTQ-R_n as new vascular imaging probes was demonstrated by comparing the luminescence microscopic images of several organs and tumor tissues with those obtained using FITC-tomato lectin, often used as a vascular endothelial imaging reagent as mentioned earlier. Furthermore, to reveal the utility of these newly-developed phosphorescent vascular probes, confocal luminescence (fluorescence and phosphorescence) lifetime imaging experiments were performed.

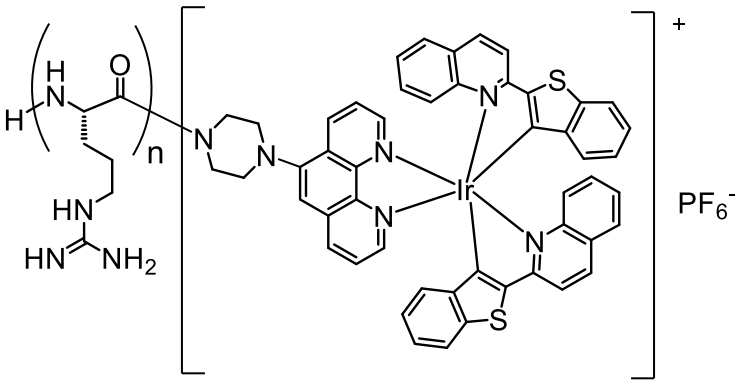

BTQ-R_n (n = 4, 8, 12, 16)

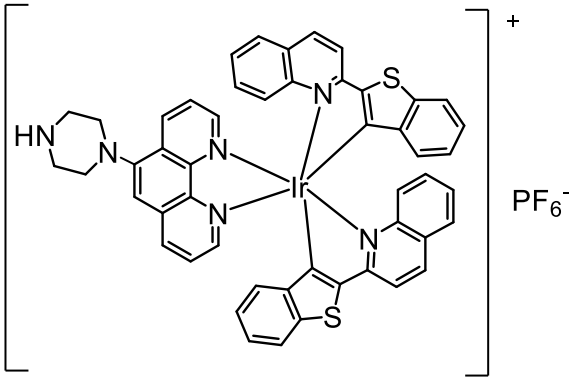

BTQphen

Figure 3-1. Chemical structures of BTQ-R_n (n = 4, 8, 12, 16) and BTQphen.

3-2 Experimental Section

3-2-1 Materials

BTQphen and BTQ-R_n (n = 4, 8, 12, 16) were synthesized and identified according to the methods described in section 3-5. All reagents and solvents used in syntheses were purchased from BeadTech, Watanabe Chemical Industries, Peptide Institute, Tokyo Chemical Industries, Wako Pure Chemical Industries, or Kanto Chemical, and were used without further purification. ^{1}H-NMR spectra were recorded with a JNM-ECS400 (JEOL) at 400 MHz. ^{1}H-NMR chemical shifts were referenced to tetramethylsilane. ESI-MS and MALDI-TOF-MS measurements were carried out on an API 2000 (Applied Biosystems) and an AXIMA performance (Shimadzu) mass spectrophotometers.

MeCN (fluorometric grade, Kanto Chemical), tris(hydroxymethyl)aminomethane (Tris, Sigma-Aldrich) and FBS (Thermo Fisher Scientific) were used as received. FITC-lectin (Vector Laboratories) was purchased from Funakoshi.

3-2-2 Absorption and emission spectra

Absorption and emission spectra were recorded on a UV-Vis spectrophotometer (Ubest V-550, JASCO) and a photonic multichannel analyzer PMA-12 (C11027-01, Hamamatsu Photonics) equipped with a monochromatized Xe arc lamp, respectively. The emission spectra were fully corrected for spectral sensitivity.

3-2-3 Phosphorescence lifetimes and phosphorescence quantum yields

Phosphorescence lifetimes were measured with a time-correlated single-photon counting fluorimeter (Quantaurus-Tau C11367G, Hamamatsu Photonics). A laser diode (M12488-35, Hamamatsu Photonics; 481 nm, pulse width 70 ps) was used as the

excitation light source. The temperature of the sample solution was controlled by circulating water through a jacket cuvette holder from a temperature controlled bath (RTE7, Neslab). Phosphorescence quantum yields were determined on an absolute photoluminescence quantum yield measurement system (C9920-02, Hamamatsu Photonics) consisting of a Xe arc lamp, a monochromator, an integrating sphere, and a multichannel detector [26].

3-2-4 Cell lines and culture

Alpha mouse liver 12 (AML12) cells were kindly gifted by Prof. T. Inagaki of the Laboratory of Epigenetics and Metabolism, IMCR, Gunma University. Human colorectal carcinoma (HCT-116) cells were purchased from the American Type Culture Collection. AML12 cells were cultured in Dulbecco's modified Eagle's medium: nutrient mixture F-12 (DMEM/F12, Thermo Fisher Scientific). HCT-116 cells were cultured in McCoy's 5A medium. These media were supplemented with 10% fetal bovine serum (FBS, Thermo Fisher Scientific), penicillin (50 units/mL, Thermo Fisher Scientific) and streptomycin (50 μg/mL, Thermo Fisher Scientific). All cells were grown at 37 °C under a 5% CO_2 atmosphere.

3-2-5 Cell viability assay

AML12 cells (2×10^4 cells/well) were seeded into a 96-well flat bottom plate (Greiner) and allowed to adhere for 24 h. A stock solution of BTQ-R_{12} (1 mM) in DMSO was diluted with DMEM/F12 containing 10% fetal bovine serum, penicillin (50 units/mL) and streptomycin (50 μg/mL). The cells were incubated with the probe for 24 h at 37 °C under a 5% CO_2 atmosphere. The medium was removed and the cells were washed gently with

DMEM/F12, then the medium was replaced with DMEM/F12 without phenol red. Cell Counting Kit-8 reagent (CCK-8, Dojindo) was added to each well and incubation was continued for 2 h. The absorbance at 450 nm of each well referenced at 650 nm was recorded using a microplate reader (Infinite 200 PRO, TECAN). Cell viability (% of control) was evaluated as $(A_{sample} - A_{blank}) / (A_{control} - A_{blank}) \times 100$, where A_{sample} is the absorbance of cells exposed to the probe, $A_{control}$ is the absorbance of cells without probe, and A_{blank} is the absorbance of wells without cells [27].

3-2-6 Animals

All protocols for animal experiments were approved by the Ethical Committee on Animal Experiments of Gunma University (18-018), and all animal experiments were conducted under the institutional guidelines. seven- to nine-week-old Balb/c male mice (CLEA Japan) were used in this study. Tumor transplants were established in Seven-week-old male athymic Balb/c nude mice (nu/nu) (CLEA Japan) by subcutaneous injection of suspension of HCT-116 cells (5×10^6 cells in 150 μL PBS:Matrigel (1:1 v/v)). Experiments with tumor-bearing mice were performed two weeks after the injection of tumor cells. Fatty liver model mice were generated by feeding six-week-old Balb/c male mice (CLEA Japan) with a choline-deficient, L-amino acid-defined, high-fat diet (CDAHFD, A06071302, Research Diets) consisting of 60 kcal% fat and 0.1% methionine for two weeks [28].

3-2-7 *In vivo* phosphorescence intensity and lifetime imaging

A stock solution of BTQphen (1 mM) was prepared by dissolving in saline:DMSO (9:1 v/v). Stock solutions of BTQ-R_n (1 mM) and FITC-dextran (1mg/mL) were prepared by

dissolving in saline. A stock solution of PC6S (0.5 mM) was prepared by dissolving in saline:DMSO (9:1 v/v) containing 10 wt% BSA. Mice were anaesthetized by intraperitoneal injection of mixed anesthetic (ketamine: 100 mg/kg, xylazine: 10 mg/kg in saline). Stock solutions of BTQphen (1 mM, 100 μL), BTQ-R_n (1 mM, 100 μL), FITC-lectin (1 mg/mL, 50 μL), and FITC-dextran (1 mg/mL, 100 μL) were injected into the tail vein under anesthesia. For dual color imaging experiments, a stock solution of PC6S (0.5 mM, 100 μL) was injected into the tail vein under anesthesia, and 10 min later BTQ-R_{12} solution (1 mM, 100 μL) was injected into the tail vein. The kidney or other tissue was exposed by flank or median incision, then the mouse was turned with its exposed tissue on a cover glass chamber (Iwaki). Luminescence intensity and lifetime images were recorded on an inverted fluorescence microscope (IX73, Olympus) equipped with a confocal scanning system (DCS-120, Becker & Hickl). The excitation light source was a picosecond diode laser (BDL-SMC, wavelength: 488 nm, pulse width: 40−90 ps, repetition rate: 20 MHz, Becker & Hickl). Emission was detected with a hybrid detector module (HPM-100-40, Becker & Hickl)[29]. Emission decay curves were analyzed using SPCImage data analysis software (Becker & Hickl) to obtain emission intensity, lifetime images, and gated image.

3-3 Results and Discussion

3-3-1 Photophysical properties and cellular uptake of BTQ-R_n

Ir(III) complexes BTQ-R_n (n = 4, 8, 12, 16) with different lengths of arginine peptides in the ligand (Figure 3-1) were obtained by chemical synthesis, including solid-phase synthesis of the peptides. The synthetic details and characterization of BTQ-R_n are described in 3-5. Firstly, the spectral and photophysical properties of the synthesized BTQ-R_n (n = 4, 8, 12, 16) were examined in MeCN and Tris-HCl buffer (pH 7.0) and compared them to the parent complex BTQphen. Figures 3-2 shows the absorption and emission spectra of BTQphen and BTQ-R_n in MeCN. All the complexes exhibit very similar absorption and emission spectra. The first absorption band of BTQ-R_{12} (a representative BTQ-R_n), which has a molar absorption coefficient of 7,600 mol^{-1} dm^3 cm^{-1} at 496 nm, can be assigned to the singlet metal-to-ligand charge transfer (^{1}MLCT) transition [30]. Emissions appear in the red to near-infrared region, with the maximum at around 660 nm, and show a very large Stokes shift. The emission decay profiles follow single-exponential functions, with lifetimes of 5.7 μs for BTQphen and 5.9 μs for BTQ-R_{12} in deaerated MeCN, and 0.28 μs for BTQphen and BTQ-R_{12} in aerated MeCN (Table 3-1). The extremely long lifetimes in deaerated solution and significant quenching by dissolved oxygen indicate that emission is due to phosphorescence. The spectral properties of BTQphen and all the BTQ-R_n complexes are very similar (Figure 3-2), indicating that the oligoarginine moiety has little effect on the electronic properties of these complexes. Furthermore, as shown in Table 3-1, the phosphorescence quantum yields (Φ_p^0 and Φ_p) and lifetimes (τ_p^0 and τ_p) of BTQ-R_n in deaerated and aerated MeCN are very close to those of BTQphen. In Tris-HCl buffer (pH 7.0), BTQphen forms aggregates due to its extremely low water solubility, whereas BTQ-R_n shows high

solubility in water and has absorption and emission spectra similar to those in MeCN (Figure 3-3). The phosphorescence decay profiles of BTQ-R_n in aerated and deaerated Tris-HCl buffer (pH 7.0) (Figure 3-4) follow single-exponential decay functions, supporting the absence of aggregate formation in water. The Φ_p^0 and τ_p^0 values of BTQ-R_n in buffer are reduced compared to those in MeCN (Table 3-1), whereas Φ_p and τ_p are increased because the solubility of oxygen in water is significantly lower than that in MeCN [31].

The interactions of BTQ-R_n complexes with albumin were then investigated by their phosphorescence decay properties in fetal bovine serum (FBS). The binding of Ir(III) complexes to albumin prolongs the emission lifetime as compared to in the absence of albumin because quenching by dissolved O_2 is suppressed by the surrounding amino acid residues [27]. The phosphorescence decay curves of BTQ-R_n in FBS deviated from single-exponential decay and could be analyzed by double-exponential decay functions with lifetimes of 1.4–1.7 μs and 4.0–4.4 μs at 37 °C (Figure 3-5, Table 3-2). Both components give much longer lifetimes in FBS than in water (0.70–0.74 μs). BTQphen dissolved in FBS showed a phosphorescence decay profile similar to those of BTQ-R_n, indicating that BTQphen was incorporated into albumin. These results suggest that the hydrophobic BTQ moiety of BTQ-R_n interacts with a binding site on albumin, with BTQ-R_n thus binding to two different domains in albumin. Vascular imaging in mice typically involves administering probe molecules intravenously and thus BTQ-R_n is expected to be transported in the blood while bound to albumin.

Hydrophobic Ir(III) complexes with an appropriate cationic charge show high cellular uptake efficiency, whereas cell uptake is greatly reduced by introducing polyethylene glycol (PEG) into the ligand to increase hydrophilicity [22,32]. Oligoarginine is a

representative water-soluble cell-penetrating peptide and functions as a carrier for transporting membrane-impermeable molecules to target cells [33–35]. Hence, oligoarginine in the ligand may aid the uptake of BTQ-R_n into cells. Indeed, emission microscope images of mouse hepatocyte cells (AML12 cells) incubated with 2.0 μM BTQ-R_n for 2 h showed that BTQ-R_n is taken up into cells and probably accumulates in endosomes (Figure 3-6). The cytotoxicity of BTQ-R_{12} to AML12 cells was evaluated with the WST assay (incubation time: 24 h in the presence of BTQ-R_{12}). No cytotoxicity was observed up to 10 μM (Figure 3-7), demonstrating that BTQ-R_n has relatively low cytotoxicity.

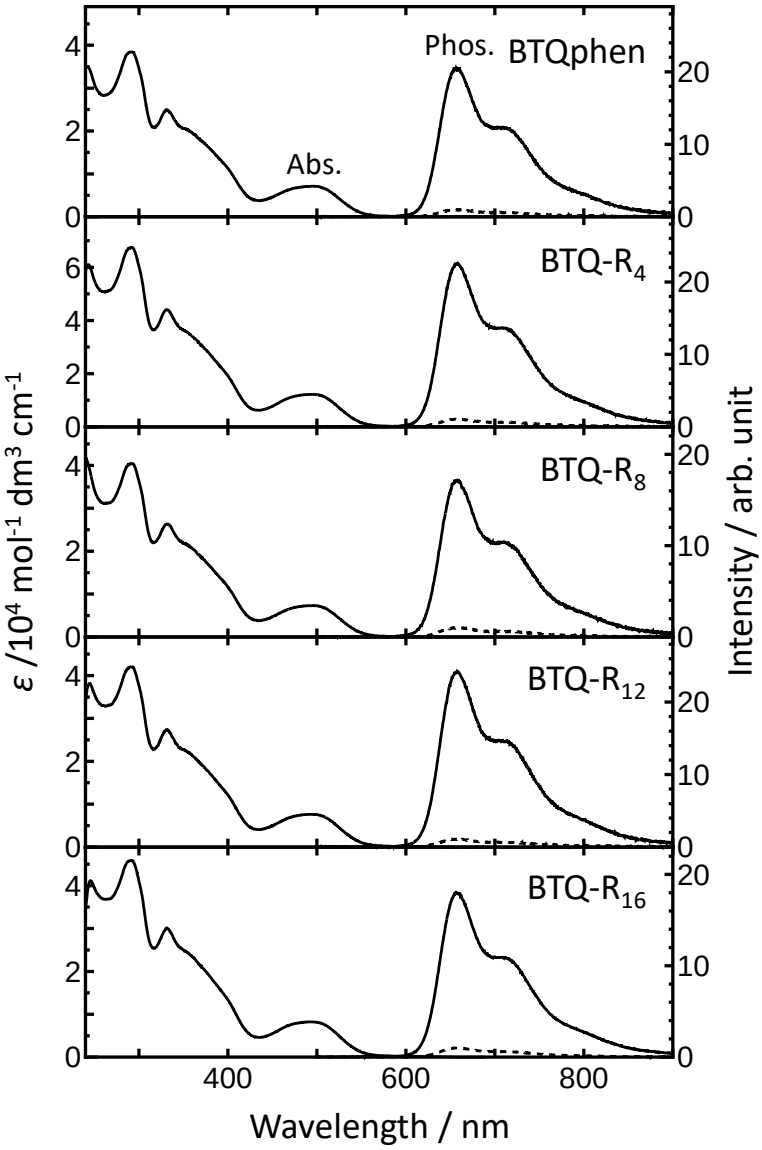

Figure 3-2. Absorption and phosphorescence spectra of BTQphen and BTQ-R_n (n = 4, 8, 12, 16) in MeCN containing 1% DMSO. Absorption spectra and phosphorescence spectra were measured at room temperatre and 37 °C, respectively. The phosphorescence spectra were taken in both deaerated (solid line) and aerated (dashed line) solutions.

Table 3-1. Phosphorescence quantum yield and lifetime of BTQphen and BTQ-R_n (n = 4, 8, 12, 16) in MeCN and Tris-HCl buffer (pH 7.0).

Compound	Φ_p^{0} a)	Φ_p a)	τ_p^0/μs b)	τ_p/μs b)
BTQphen	0.32	0.015	5.7	0.28
BTQ-R_4	0.30	0.013	5.9	0.28
	(0.23) [a]	(0.061)	(3.5)	(0.70)
BTQ-R_8	0.30	0.012	5.7	0.28
	(0.20)	(0.046)	(3.5)	(0.74)
BTQ-R_{12}	0.29	0.016	5.9	0.28
	(0.20)	(0.051)	(3.5)	(0.73)
BTQ-R_{16}	0.29	0.017	5.8	0.30
	(0.20)	(0.050)	(3.5)	(0.74)

a) at room temperature. b) at 37 °C. c) in parentheses are in Tris-HCl buffer (pH 7.0). ϕ_p^0 and τ_p^0 denote the phosphorescence quantum yield and lifetime taken for degassed solutions, ϕ_p and τ_p stands for the phosphorescence quantum yield and lifetime taken for aerated solutions.

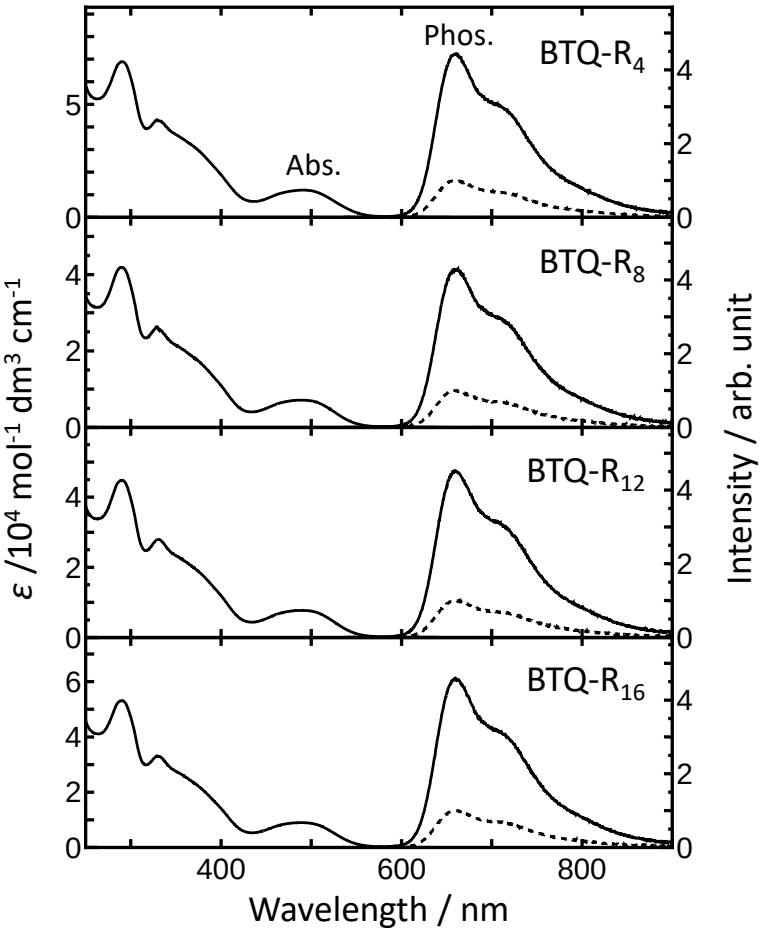

Figure 3-3. Absorption and phosphorescence spectra of BTQ-R_n (n = 4, 8, 12, 16) in Tris-HCl buffer (pH 7.0) containing 1%DMSO. Absorption spectra and phosphorescence spectra were measured at room temperature and 37 °C, respectively. The phosphorescence spectra were taken in both deaerated (solid line) and aerated (dashed line) solutions.

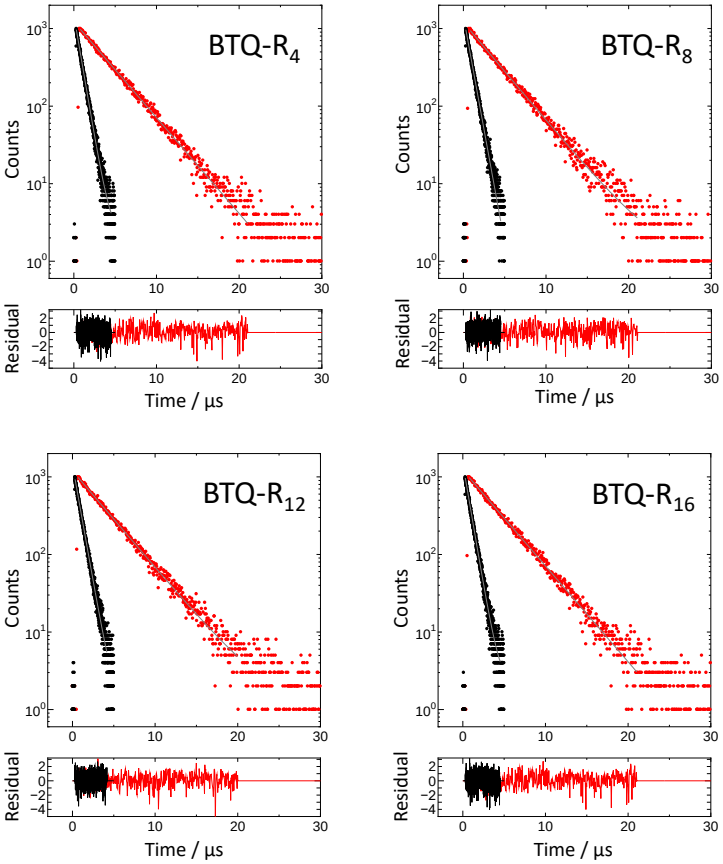

Figure 3-4. Phosphorescence decay curves of BTQ-R_n (n = 4, 8, 12, 16) in Tris-HCl buffer (pH 7.0) containing 1%DMSO at 37 °C. Excited at 488 nm and monitored at 660 nm. Black: aerated, red: deaerated.

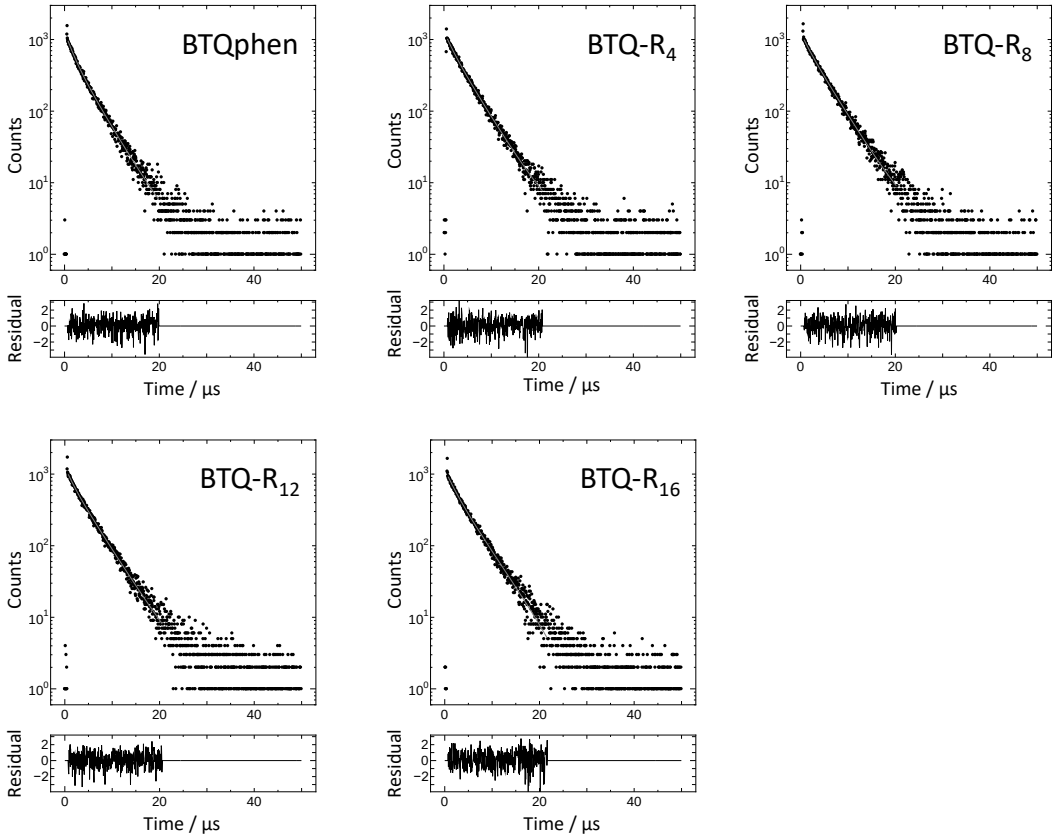

Figure 3-5. Phosphorescence decay curves of BTQphen and BTQ-R_n (n = 4, 8, 12, 16) in FBS containing 1% DMSO at 37 °C. Excited at 488 nm and monitored at 660 nm.

Table 3-2. Phosphorescence lifetimes of BTQphen and BTQ-R_n (n = 4, 8, 12, 16) in FBS containing 1% DMSO at 37 °C. Excited at 488 nm and monitored at 660 nm.

Compound	τ_1/μs	τ_2/μs
BTQphen	1.65 (41%)	4.05 (59%)
BTQ-R_4	1.45 (23%)	4.03 (77%)
BTQ-R_8	1.58 (25%)	4.19 (75%)
BTQ-R_{12}	1.56 (27%)	4.31 (73%)
BTQ-R_{16}	1.57 (24%)	4.23 (76%)

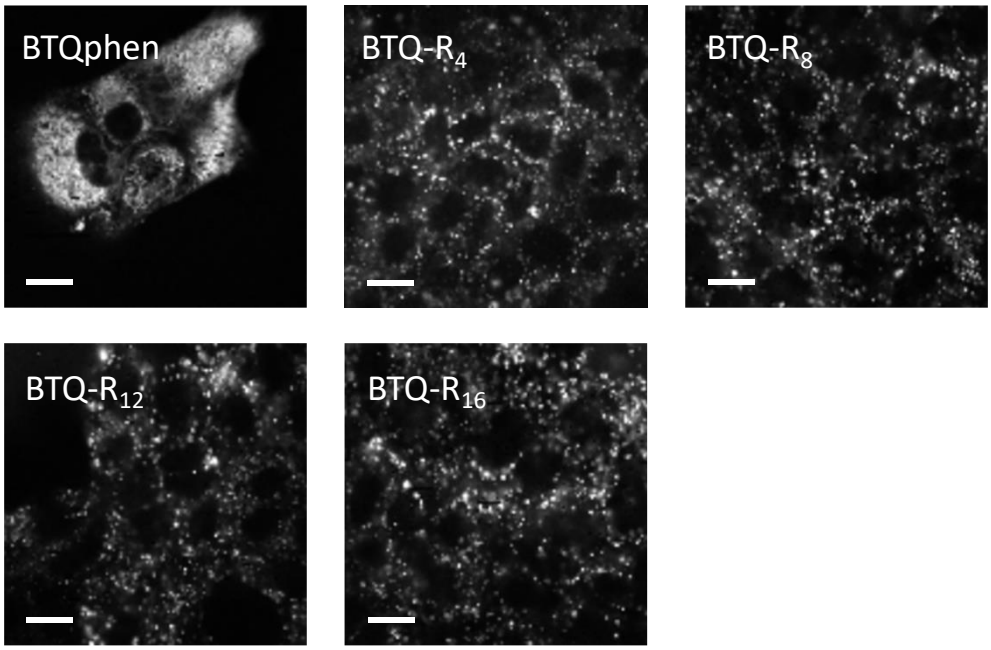

Figure 3-6. Phosphorescence intensity image of AML12 cells incubated with BTQphen and BTQ-R_n (n = 4, 8, 12, 16) (2 μM) for 2 h at 37℃. λ_{exc}: 488 nm, λ_{em}: >590 nm. Scale bar: 20 μm.

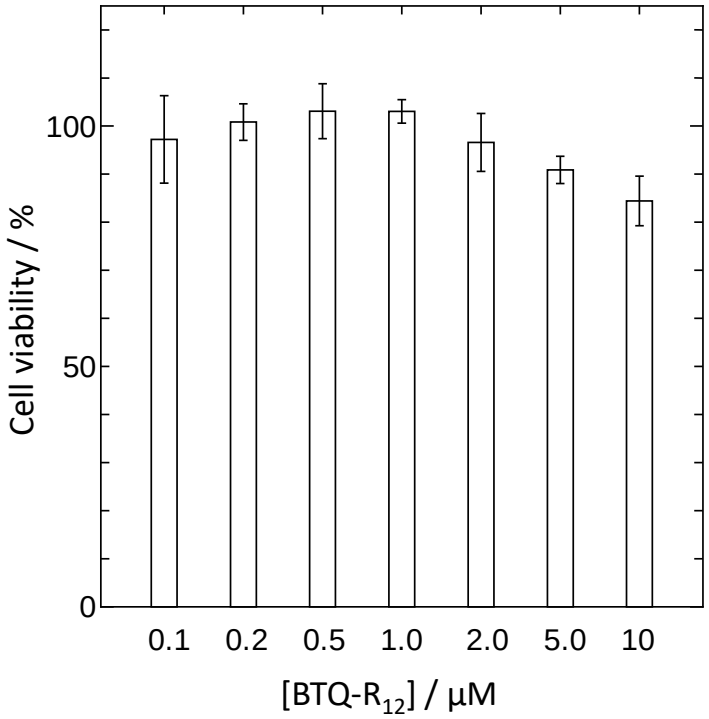

Figure 3-7. Cell viability of AML12 cells incubated with different concentrations of BTQ-R_{12} for 24 h. Error bars stand for SD (n = 6).

3-3-2 *In vivo* imaging of mouse renal vessels using BTQ-R_n

To evaluate the performance of BTQ-R_n as a vascular imaging probe, the solution of BTQ-R_n or BTQphen (100 nmol in 100 μL saline) was injected to mice from tail vein under anesthesia, then exposed the kidney by flank incision and obtained luminescence intensity images of the renal cortex. Similarly, FITC-lectin, known to bind to the vascular endothelium [18], was administered to mice, and fluorescence images of the renal cortex were compared with the phosphorescence images obtained using BTQ-R_n or BTQphen (Figure 3-8). All images taken approximately 1 h after probe administration clearly visualized the microstructure of renal cortex tissue [29], but the localizations of the probes appeared to be different. Specifically, BTQphen localized in tubular cells rather than in capillaries and exhibited phosphorescence almost exclusively from inside the cells. This is consistent with the properties of cationic Ir(III) complexes with an *o*-phenanthroline ligand, i.e., being efficiently taken up into cells and accumulating in mitochondria [27,36]. BTQ-R_4, which has the shortest arginine chain, also shows migration from the intravascular to the intracellular space, although the intracellular location appears to be different from that of BTQphen. In contrast, other BTQ-R_n compounds (n = 8, 12, 16) with longer arginine chains selectively image the endothelium of renal capillaries, similar to FITC-lectin. These results indicate that eight or more arginine residues are required to selectively stain the vascular endothelium using BTQ-R_n. The emission images of BTQ-R_n (n = 8, 12, 16) in Figure 3-8 were acquired using an excitation laser intensity equal to or lower than that used for FITC-lectin, although the detection wavelength was different (510–560 nm for FITC-lectin and >590 nm for BTQ-R_n). Even three hours after probe administration, clear capillary images were obtained with undiminished brightness (Figure 3-9A). This was in contrast to the short retention of fluorescent dextran with a

molecular weight of 70 kDa that dissolve in blood plasma and circulate in the bloodstream (Figure 3-9B).

The usefulness of BTQ-R_n was further investigate using BTQ-R_{12}. First, colocalization analyses to compare the stained areas of FITC-lectin and BTQ-R_{12} in the renal cortex were performed (Figure 3-10A). Emission intensity images of renal cortex obtained by simultaneous administration of BTQ-R_{12} and FITC-lectin are shown in the pseudo colors red and green, respectively, and their overlay image is shown on the right. The emission image obtained following BTQ-R_{12} administration (Figure 3-10A, left) comprises both long-lived phosphorescence and short-lived fluorescence components. As can be seen from the overlay image, BTQ-R_{12} and FITC-lectin exhibit emission from the vascular endothelium, demonstrating similar localization within capillaries. This suggests that BTQ-R_{12}, like FITC, specifically binds to endothelial cells in blood vessels. Figure 3-10A shows that emission originates not only from the capillaries but also inside the tubular cells and is observed as bright speckles. To clarify the origin of emission from the cells, luminescent lifetime images of renal cortex using BTQ-R_{12} and FITC-lectin were obtained based on fluorescence or phosphorescence lifetime imaging microscopy (FLIM/PLIM) (Figure 3-10B). It should be noted here that the color scales for lifetime are significantly different between PLIM images obtained using BTQ-R_{12} and FLIM images obtained using FITC-lectin. The distribution histogram of the emission lifetime in the renal FLIM image obtained using FITC-lectin (Figure 3-10C) indicates that the FLIM image obtained by staining with FITC-lectin comprises at least two different components with average lifetimes of around 0.8 ns and 1.6 ns. The short and long lifetime components can be assigned to autofluorescence by the renal cortex and the fluorescence of FITC-lectin, respectively, given that (1) the lifetime distribution of control

images without FITC-lectin (Figure 3-10C, right) approximate the distribution of the shorter lifetime component of FITC-lectin, and (2) the fluorescence lifetime (3.68 ns) of FITC-lectin in saline solution is longer than that of the shorter lifetime component. It is important to note here that it is difficult to remove the contribution of autofluorescence in FITC-lectin-based images because of the close proximity of the emission wavelengths of autofluorescence and FITC-lectin, and it is difficult to remove autofluorescence with a filter. In contrast, with BTQ-R_{12}, the autofluorescence component can be removed due to the large difference in lifetime between autofluorescence and BTQ-R_{12} phosphorescence (Figure 3-11). Figure 3-11C shows the accumulation of phosphorescence due to repeated irradiation with pulsed laser light and the subsequent phosphorescence decay profile when the laser is turned off. During the accumulation of phosphorescence, the fluorescence decays rapidly after each pulsed excitation. The image shown in Figure 3-11A was obtained by observing the emission over the entire time domain, and that in Figure 3-11B is a gated image in which only the phosphorescence component was observed after the laser pulse was turned off. As can be seen from Figure 3-11B, autofluorescence is absent and only the capillaries of the renal cortex are clearly imaged. The removal of autofluorescence by using a time-gated emission detection method is an important advantage of phosphorescent probes [37].

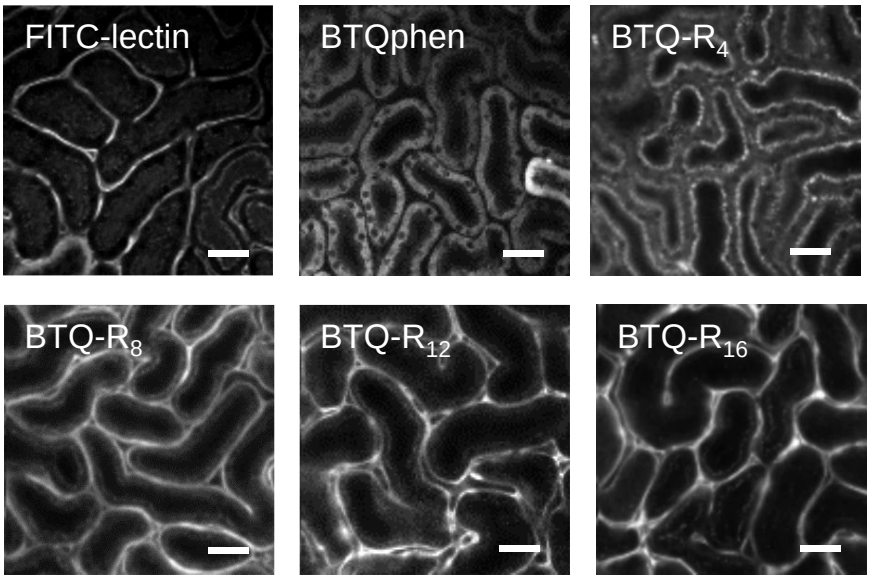

Figure 3-8. *In vivo* luminescence intensity images of mouse kidney after intravenous injection of FITC-lectin (1 mg/mL, 50 μL), BTQphen (100 nmol), and BTQ-R_n (n = 4, 8, 12, 16) (100 nmol). λ_{exc}: 488 nm, λ_{em}: >590 nm (BTQ-R_{12}), 510-560 nm (FITC-lectin). Scale bar 50 μm.

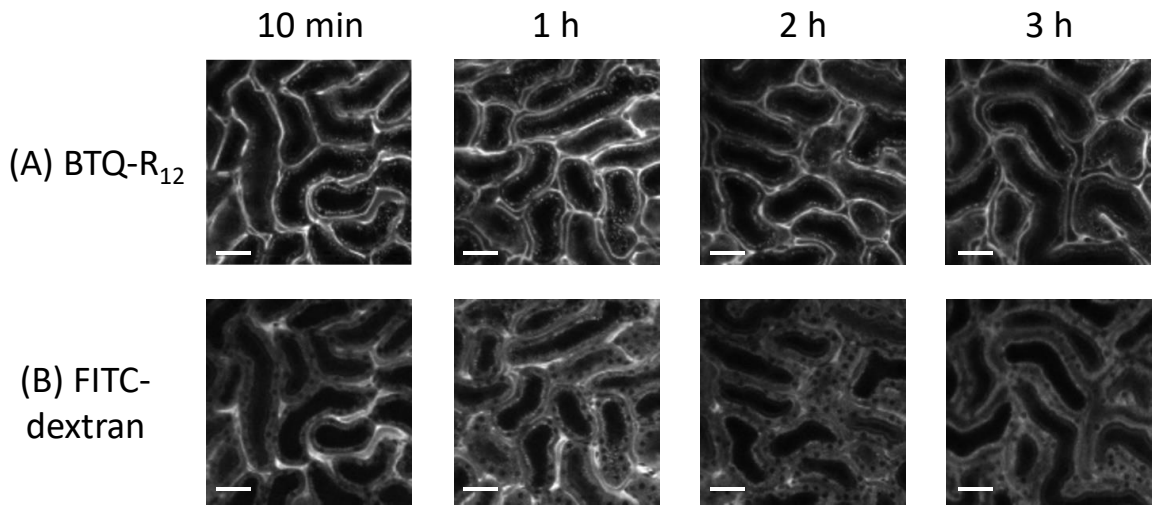

Figure 3-9. Emission intensity images of kidney observed at 10 min, 1, 2, and 3 h after intravenous injection of BTQ-R_{12} (100 nmol) (A) and FITC-dextran (70 kDa) (1 mg/ml, 100μl) (B). λ_{exc}: 488 nm, λ_{em}: >620 nm (BTQ-R_{12}), 510-560 nm (FITC-dextran). Scale bar 50 μm.

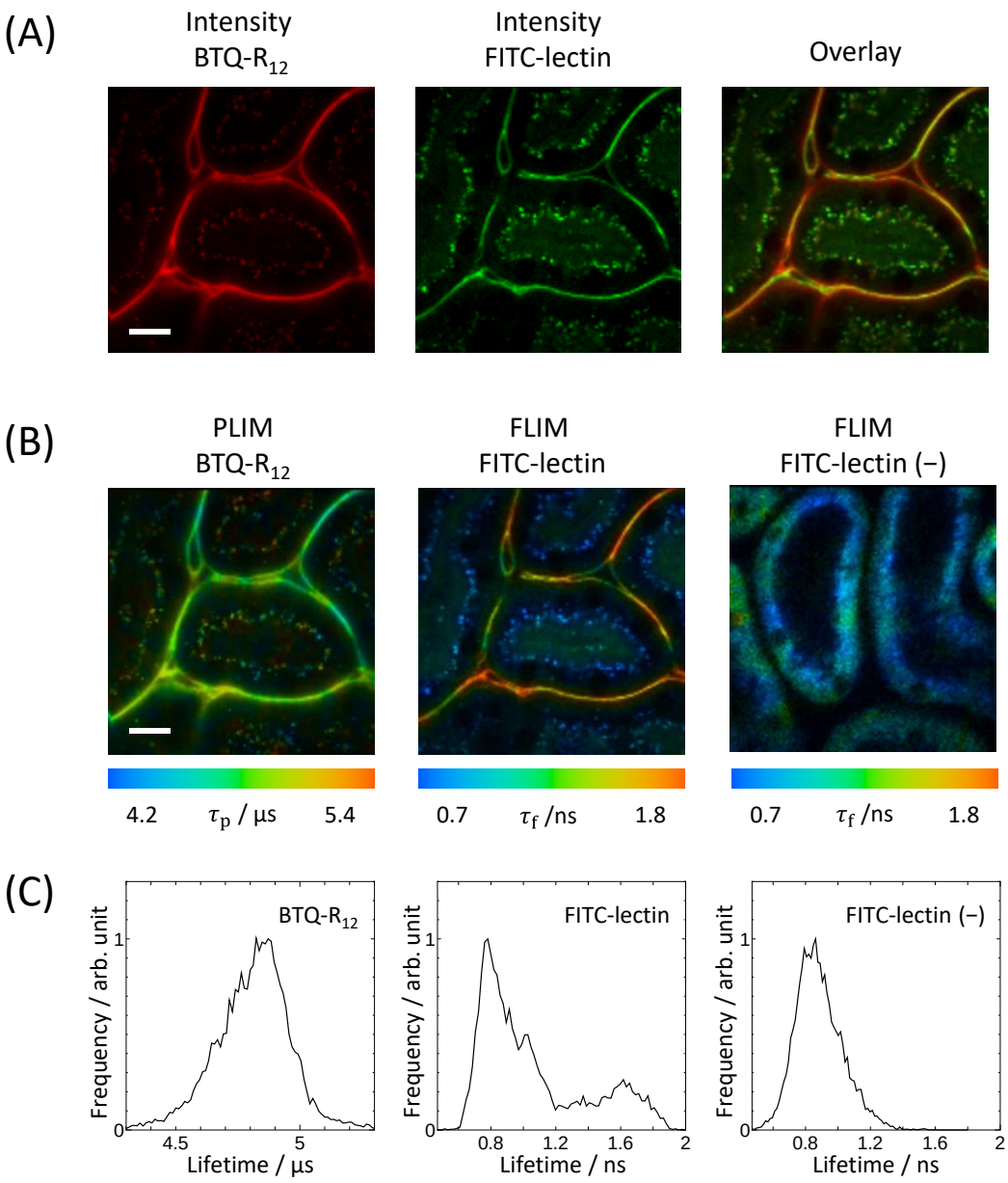

Figure 3-10. Luminescence intensity images (A) and PLIM or FLIM images (B) of mouse kidney at 1.5 h after intravenous injection of BTQ-R_{12} (100 nmol) and FITC-lectin (1 mg/ml, 50 μL). The right panel in A is the overlay image. A FLIM image of unstained renal cortex is shown in the right panel in B. λ_{exc}: 488 nm, λ_{em}: >590 nm (BTQ-R_{12}), 510-560 nm (FITC-lectin). Scale bar 20 μm. (C) Distribution histograms of the luminescence lifetimes for the PLIM and FLIM images in (B).

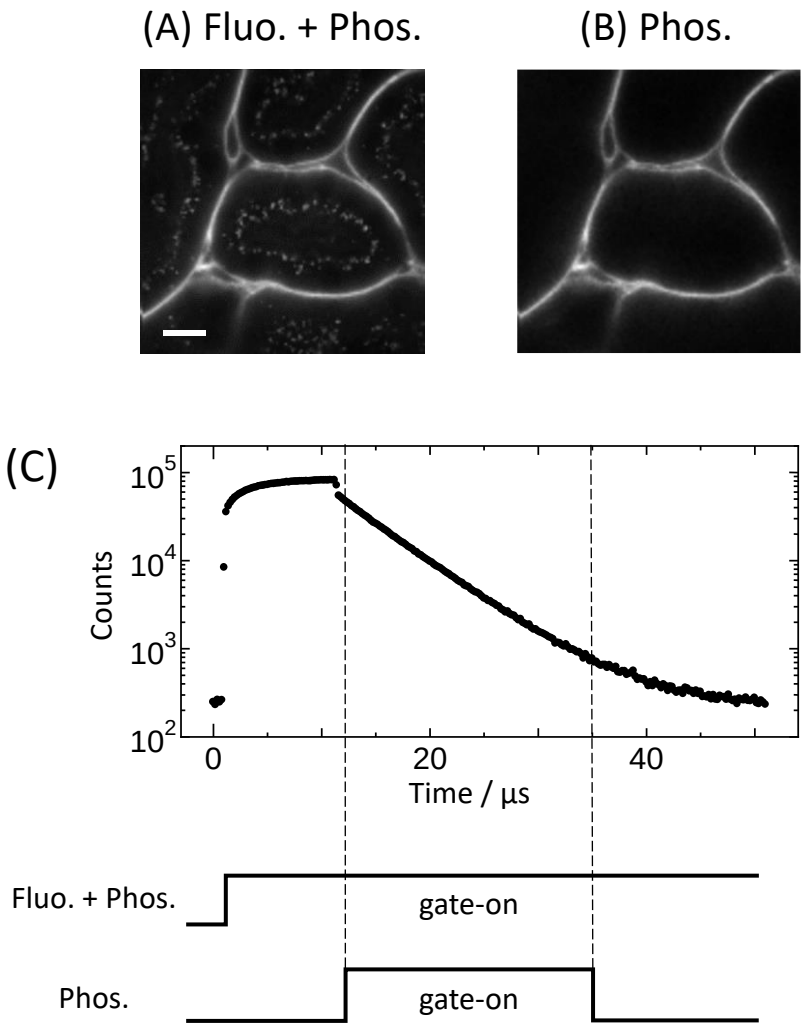

Figure 3-11. Elimination of autofluorescence from kidney using the time gating method. (A) Luminescence intensity image of BTQ-R_{12} including tissue autofluorescence and (B) its gated image. Scale bar 20 μm. (C) Luminescence decay curve of the total pixels in image A. The schematic shows the time domains of A and B. The dashed lines show the start and end of the time gate. Gate: 12-35 μs.

3-2-3 Visualization of blood vessels in normal and pathological tissues

The confocal microscope images obtained using our PLIM system are limited to a depth of approximately 30 μm from the renal surface. Glomerular images could therefore not be obtained and so PLIM images on mouse kidney sections following the administration of BTQ-R_{12} (Figures 3-12) were measured. As can be seen from the high magnification image of a kidney section in Figure 3-12B, BTQ-R_{12} can be used to image the fine vascular network of the glomeruli. The administration of BTQ-R_{12} allows *in vivo* and *ex vivo* imaging of the microvasculature in a variety of organs and tissues, including pancreas, liver, small intestine, adrenal gland, hypodermal tissue, bone marrow, lung and heart (Figure 3-13).

Next, *in vivo* vascular imaging of tumor tissues were attempted by intravenously administrating BTQ-R_{12} to tumor-bearing mice. Figure 3-14 shows phosphorescence intensity images of a solid tumor that grew for two weeks after transplanting HCT-116 cells (5×10^6 cells) subcutaneously into the lower thigh of mice. The images were taken after removing the skin covering the tumor, placing the exposed tumor on a thin glass plate on a microscope stage, and irradiating the surface with excitation laser light from below. The phosphorescence intensity images of different regions of the same tumor at different magnifications show large blood vessels and a large number of small neovasculatures branching from them. It is clear from Figures 3-14 that the vascular structure of the tumor tissue is extremely heterogeneous, in contrast to the structure of the sinusoids in the liver, which are arranged in interconnecting polygonal networks.

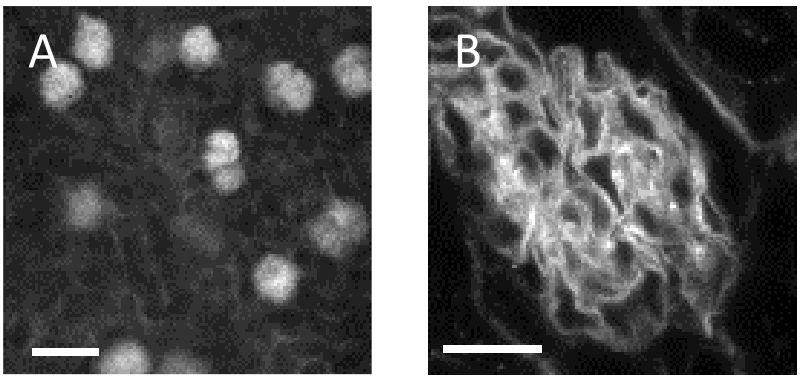

Figure 3-12. Phosphorescence intensity images of kidney (A) and glomerulus (B) in living mice administrated BTQ-R_{12} (100 nmol) via the tail vein under anesthesia. λ_{exc}: 488 nm, λ_{em}: >590 nm. Scale bar: 100 μm in (A), 20 μm in (B).

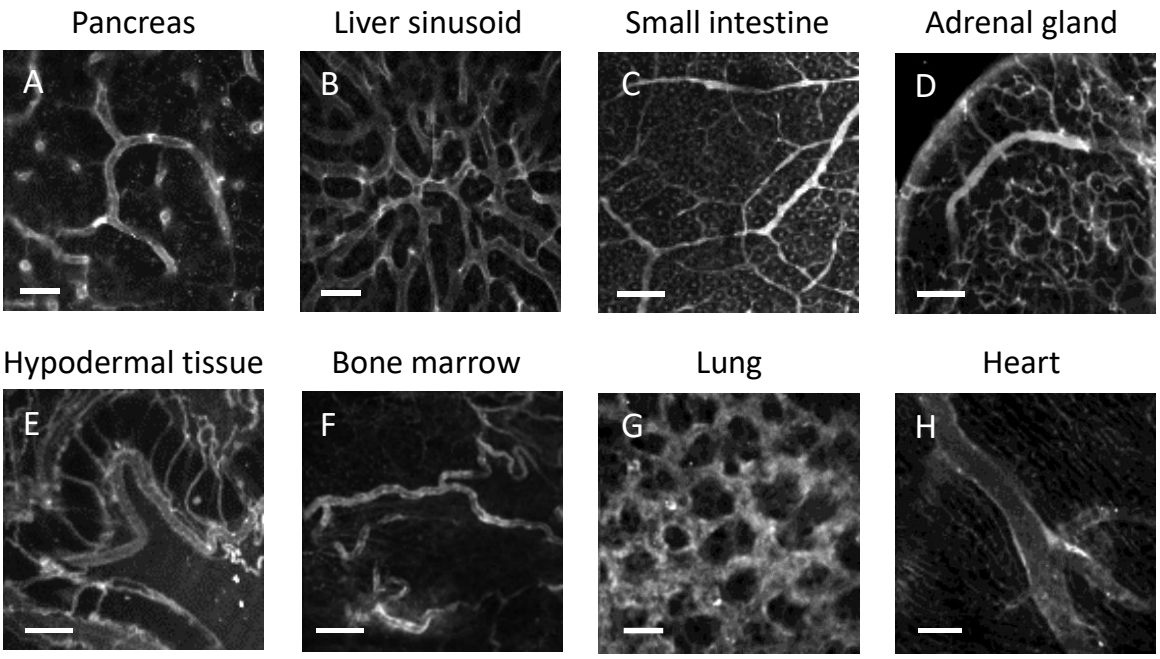

Figure 3-13. Phosphorescence intensity images of pancreas (A), liver sinusoids (B), small intestine (C), adrenal gland (D), hypodermal tissue (E), bone marrow (F), lung (G), and heart (H) in living mice administrated BTQ-R_{12} (100 nmol) via the tail vein under anesthesia. λ_{exc}: 488 nm, λ_{em}: >590 nm. Scale bar: 50 μm in (A), 50 μm in (B), 200 μm in (C), 200 μm in (D), 200 μm in (E), 100 μm in (F), 50 μm in (G), and 100 μm in (H).

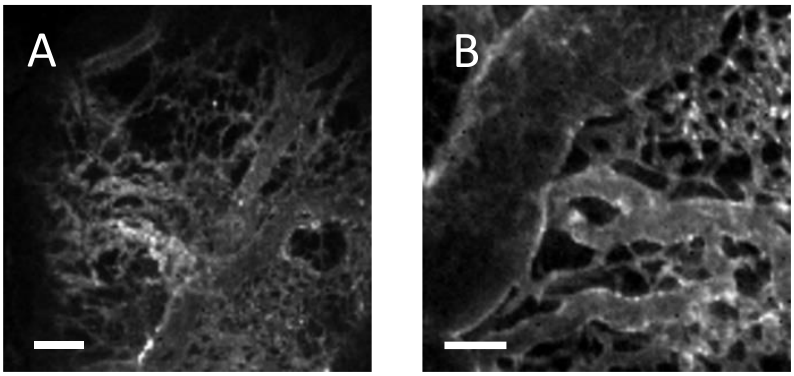

Figure 3-14. Phosphorescence intensity images of tumor vascular networks in living mice administrated BTQ-R_{12} (100 nmol) via the tail vein under anesthesia. λ_{exc}: 488 nm, λ_{em}: >590 nm. Scale bar: 500 μm in (A) and 100 μm in (B).

The liver is a highly vascular organ and receives approximately 30% of resting cardiac output. The liver is composed of a fundamental structural unit called hepatic lobule with a hexagonal shape (Figure 3-15). In the hepatic portal system, the liver receives blood both from the hepatic portal vein and the hepatic arteries, and the blood mixes in the sinusoids. The sinusoids are uniformly distributed throughout the entire liver volume and constitute the hepatic microcirculation. The onset and progression of liver diseases are expected to cause changes in the network structure of the sinusoid [38]. Here, to obtain luminescence microscope images of the liver of mice fed a high-fat diet for two weeks, BTQ-R_{12} was used as an intravascular probe. The organization of the sinusoid network of the fatty liver was visualized compared with that of healthy mice. The mice fed a high-fat diet for two weeks are expected to have fatty livers due to lipid accumulation. Lipid droplets (LDs) are formed as diseases such as nonalcoholic fatty liver disease (NAFLD) and nonalcoholic steatohepatitis (NASH) progress [39–41] and thus the green fluorescent LD-specific probe PC6S [42] was co-administered to the mice. Figure 3-16 shows phosphorescence and fluorescence intensity images of liver sinusoids of living mice fed a normal diet and a high-fat diet. The LD-specific probe PC6S accumulates in the endoplasmic reticulum (ER) and more selectively in LDs in cells [42]. Figure 3-16A shows that PC6S is taken up into hepatocytes and likely accumulates in LDs and the ER. Overlay of the sinusoid image (red) obtained using BTQ-R_{12} and the hepatocytes image (green) obtained using PC6S clearly visualizes the entire microstructure of the hepatic tissue. In contrast, many LDs are apparent in the liver of mice fed a high-fat diet, and as a result the sinusoidal structure is significantly distorted (Figure 3-16B).

These results demonstrate that BTQ-R_{12} is useful for selectively staining the vascular endothelium of various organs as well as tumors, and for investigating their vascular

structure and dynamics *in vivo*. Judging from the extremely long phosphorescence lifetime of BTQ-R_{12} within kidney capillaries (Figure 3-10) compared to that in aerated solution, BTQ-R_{12} is likely taken up by vascular endothelial cells where its interaction with oxygen is suppressed, although BTQ-R_{12} may be bound to the vascular endothelium while bound to albumin. Further research is required to clarify how BTQ-R_{12} binds to the vascular endothelium following intravenous administration to mice.

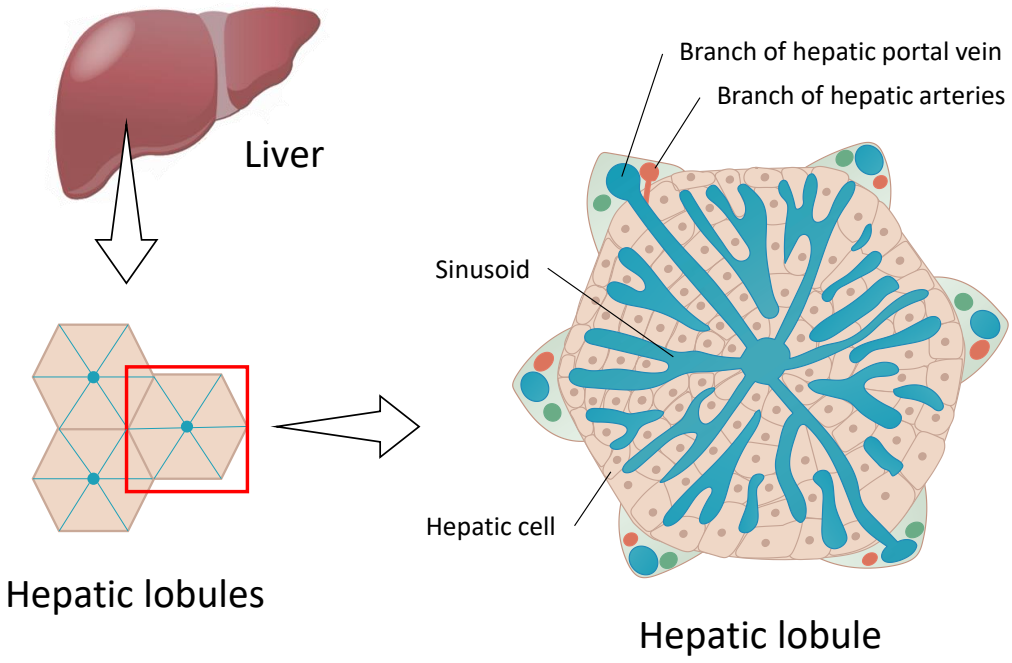

Figure 3-15. Schematic views of the hepatic lobule.

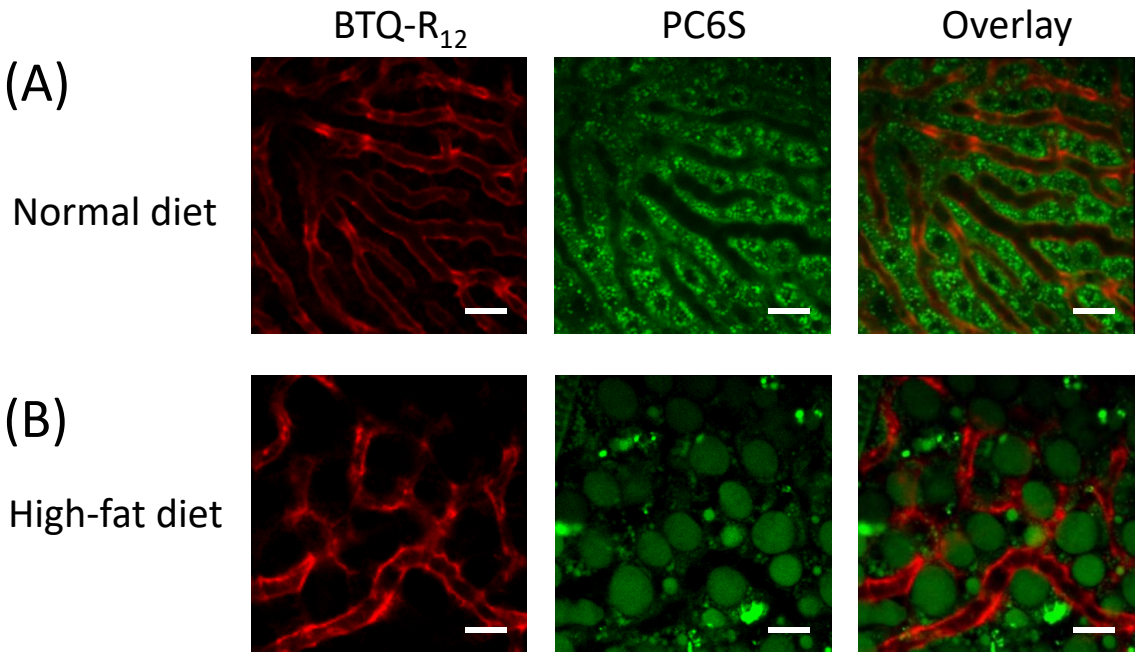

Figure 3-16. Phosphorescence and fluorescence intensity images of sinusoids (BTQ-R_{12}, 100 nmol) and hepatic lipid droplets (PC6S, 50 nmol) in the liver of mice fed a normal diet (A) or high-fat diet (B) for two weeks. λ_{exc}: 488 nm, λ_{em}: >620 nm (BTQ-R_{12}), 510-560 nm (PC6S). Scale bar: 50 μm.

3-4 Conclusions

The deep-red phosphorescent vascular imaging probes BTQ-R_n (n = 8, 12, 16), in which a Ir(III) complex is connected with an oligoarginine peptide, were designed and synthesized by conventional chemical synthesis. The blood vessels of various tissues and tumors in mice could be visualized using a confocal luminescence microscope following the intravenous administration of BTQ-R_{12}. The long luminescence lifetime of BTQ-R_{12} coupled with gated measurements allowed visualization of the vascular structure of organs without interference from autofluorescence. BTQ-R_{12} allowed long-term *in vivo* vascular network imaging because it selectively binds to vascular endothelial cells. Furthermore, dual color imaging of normal and fatty liver in living mice using BTQ-R_{12} and the green fluorescent lipid droplet probe PC6S showed distortion of the sinusoid network in mice fed a high-fat diet for two weeks. These results demonstrated that BTQ-R_{12}, combined with a confocal luminescence microscope, can be useful for imaging blood vessels in normal and pathological tissues.

3-5 Synthetic procedures for BTQ-R_n (n = 4, 8, 12, 16)

Boc-[R(Pbf)]$_n$-OH (n = 4, 8, 12, 16)

Peptides were synthesized by using a fully automated microwave peptide synthesizer (Biotage Initiator+ Alstra) based on solid-phase synthesis. H-R(Pbf)-2-Chlorotrityl resin (BeadTech, 0.38 mmol/g loading) was used as a solid support. For the coupling of an amino acid, 0.5 M Fmoc-[R(Pbf)]-OH in DMF, 0.5 M Boc-[R(Pbf)]-OH in DMF, 0.6 M HBTU in DMF, 0.5 M HOBt in DMF and 2.0 M *N*,*N*-diisopropylethylamine (DIPEA) in NMP were added into reaction vial (3 eq., 3 eq., 3 eq. and 6 eq. respectively). The reaction mixture was stirred for 1 h at room temperature. Deprotection of Fmoc group was performed in 2% DBU in DMF for 5 min at room temperature. For complete deprotection, the reaction was carried out again under the same conditions for 10 minutes. After the peptide elongation, for cleaving peptide from resin, 1% TFA in DCM (10 mL) was added into the vial, and the solution was stirred for 90 min at room temperature. The reaction mixture was filtered and filtrate was evaporated under vacuum. The crude peptide was dissolved in acetonitrile, and distilled water was added. This peptide solutions were lyophilized.

BTQ-R_4

Boc-[R(Pbf)]$_4$-OH (116 mg, 0.065 mmol), BTQphen (63 mg, 0.051 mmol), and HATU (41 mg, 0.10 mmol) were dissolved in anhydrous DMF (1 mL), then DIPEA (0.17 mL, 2.0 mmol) was added. This solution was stirred at room temperature for 24 h under N_2 gas. The distilled water was added into the reaction mixture. The precipitate was centrifuged (3500 rpm, 5 min), then water was removed by decantation. This operation was repeated twice. Any remaining water was removed from vessel by vacuum freezing

and the product (BTQ-[R(Pbf)]$_4$-Boc) was obtained as red powder. The deprotection cocktail (TFA/TIPS/H_2O 95:2.5:2.5) (1 mL) was added to BTQ-[R(Pbf)]$_4$-Boc (279 mg, 0.10 mmol) in a centrifuge tube. After 2 h at room temperature, an orange solid was precipitated by addition of the cool diethyl ether. The precipitate was centrifuged (3500 rpm, 5 min), then diethyl ether was removed by decantation. This operation was repeated twice. Diethyl ether was removed by decantation, and then the orange solid was dried in a vacuum desiccator. The crude product was obtained as orange powder (82 mg, 40%). A part of the crude product was purified by using SNAP Ultra C18 (Biotage); eluent, 30-100% acetonitrile aq. containing 0.1% TFA. The main peak fraction was collected and purified water was added. The aqueous solution was lyophilized to afford the product (BTQ-R_4) as orange powder.

ESI-MS (positive): calcd. for $C_{74}H_{84}IrN_{22}O_4S_2$ ($[M+2H]^{2+}$): 534.8, found: 534.8

MALDI-TOF MS: calcd. for $C_{74}H_{84}IrN_{22}O_4S_2^+$: 1601.9, found: 1601.2

BTQ-R$_8$

Boc-[R(Pbf)]$_4$-OH (209 mg, 0.062 mmol), BTQphen (62 mg, 0.050 mmol), and HATU (40 mg, 0.11 mmol) were dissolved in anhydrous DMF (1 mL), then DIPEA (0.17 mL, 1.0 mmol) was added. This solution was stirred at room temperature for 24 h under N_2 gas. The distilled water was added into the reaction mixture. The precipitate was centrifuged (3500 rpm, 5 min), then water was removed by decantation. This operation was repeated twice. Any remaining water was removed from vessel by vacuum freezing and the product (BTQ-[R(Pbf)]$_8$-Boc) was obtained as red powder. The deprotection cocktail (TFA/TIPS/H_2O 95:2.5:2.5) (1 mL) was added to BTQ-[R(Pbf)]$_8$-Boc（110 mg, 0.026 mmol）in a centrifuge tube. After 2 h at room temperature, an orange solid was precipitated by

addition of the cool diethyl ether. The precipitate was centrifuged (3500 rpm, 5 min), then diethyl ether was removed by decantation. This operation was repeated twice. Diethyl ether was removed by decantation, and then the orange solid was dried in a vacuum desiccator. The crude product was obtained as orange powder (72 mg, 85%). A part of the crude product was purified by using reversed phase flash column chromatography (Biotage) and the following condition: column, SNAP Ultra C18 (Biotage); eluent, 30-100% acetonitrile aq. containing 0.1% TFA. The main fraction was collected and purified water was added. The aqueous solution was lyophilized to afford the product (BTQ-R_4) as orange powder.

ESI-MS (positive): calcd. for $C_{98}H_{132}IrN_{38}O_8S_2$ ($[M+3H]^{3+}$): 743.0, found: 742.6

MALDI-TOF MS: calcd. for $C_{98}H_{132}IrN_{38}O_8S_2^+$: 2226.6, found: 2224.8

BTQ-R_{12}

Boc-$[R(Pbf)]_{12}$-OH（321 mg，0.064 mmol），BTQphen (62 mg，0.050 mmol), and HATU (40 mg，0.11 mmol) were dissolved in anhydrous DMF (1 mL), then DIPEA (0.17 mL, 1.0 mmol) was added. This solution was stirred at room temperature for 24 h under N_2 gas. The distilled water was added into the reaction mixture. The precipitate was centrifuged (3500 rpm, 5 min), then water was removed by decantation. This operation was repeated twice. Any remaining water was removed from vessel by vacuum freezing and the product (BTQ-$[R(Pbf)]_{12}$-Boc) was obtained as red powder. The deprotection cocktail (TFA/TIPS/H_2O 95:2.5:2.5) (1 mL) was added to BTQ-$[R(Pbf)]_{12}$-Boc（151 mg，0.026 mmol）in a centrifuge tube. After 2 h at room temperature, an orange solid was precipitated by addition of the cool diethyl ether. The precipitate was centrifuged (3500 rpm, 5 min), then diethyl ether was removed by decantation. This operation was repeated twice. Diethyl

ether was removed by decantation, and then the orange solid was dried in a vacuum desiccator. The crude product was obtained as orange powder (93 mg, 81%). A part of the crude product was purified by using reversed phase flash column chromatography (Biotage) and the following condition: column, SNAP Ultra C18 (Biotage); eluent, 30-100% acetonitrile aq. containing 0.1% TFA. The main fraction was collected and purified water was added. The aqueous solution was lyophilized to afford the product (BTQ-R_{12}) as orange powder.

ESI-MS (positive): calcd. for $C_{122}H_{180}IrN_{54}O_{12}S_2$ ($[M+4H]^{4+}$): 713.6, found: 713.

MALDI-TOF MS: calcd. for $C_{122}H_{180}IrN_{54}O_{12}S_2^+$: 2851.4, found: 2846.8

BTQ-R_{16}

Boc-[R(Pbf)]$_{16}$-OH (183 mg, 0.028 mmol), BTQphen (37 mg, 0.030 mmol), and HATU (35 mg, 0.09 mmol) were dissolved in anhydrous DMF (1 mL), then DIPEA (0.17 mL, 1.0 mmol) was added. This solution was stirred at room temperature for 24 h under N_2 gas. The distilled water was added into the reaction mixture. The precipitate was centrifuged (3500 rpm, 5 min), then water was removed by decantation. This operation was repeated twice. Any remaining water was removed from vessel by vacuum freezing and the product (BTQ-[R(Pbf)]$_{16}$-Boc) was obtained as red powder. The deprotection cocktail (TFA/TIPS/H_2O 95:2.5:2.5) (1 mL) was added to BTQ-[R(Pbf)]$_{12}$-Boc (186 mg, 0.024 mmol) in a centrifuge tube. After 2 h at room temperature, an orange solid was precipitated by addition of the cool diethyl ether. The precipitate was centrifuged (3500 rpm, 5 min), then diethyl ether was removed by decantation. This operation was repeated twice. Diethyl ether was removed by decantation, and then the orange solid was dried in a vacuum desiccator. The crude product was obtained as orange powder (73 mg, 87%). A

part of the crude product was purified by using reversed phase flash column chromatography (Biotage) and the following condition: column, SNAP Ultra C18 (Biotage); eluent, 30-100% acetonitrile aq. containing 0.1% TFA. The main fraction was collected and purified water was added. The aqueous solution was lyophilized to afford the product (BTQ-R_{12}) as orange powder.

ESI-MS (positive): calcd. for $C_{146}H_{228}IrN_{70}O_{16}S_2$ ($[M+4H]^{4+}$): 869.7, found: 869.6.

MALDI-TOF MS: $C_{146}H_{228}IrN_{70}O_{16}S_2^+$: 3474.8, found: 3473.7

References

[1] P. Carmeliet, *Int. J. Biochem.*, **1993**, *25*, 1344.

[2] J. Klohs, C. Baltes, F. Princz-Kranz, D. Ratering, R. M. Nitsch, I. Knuesel and M. Rudin, *J. Neurosci.*, **2012**, *32*, 1705–1713.

[3] B. Vandeghinste, B. Trachet, M. Renard, C. Casteleyn, S. Staelens, B. Loeys, P. Segers and S. Vandenberghe, *Mol. Imaging Biol.*, **2011**, *13*, 78–86.

[4] J. Epah, K. Pálfi, F. L. Dienst, P. F. Malacarne, R. Bremer, M. Salamon, S. Kumar, H. Jo, C. Schürmann and R. P. Brandes, *Theranostics*, **2018**, *8*, 2117–2133.

[5] M. E. Lobatto, T. Binderup, P. M. Robson, L. F. P. Giesen, C. Calcagno, J. Witjes, F. Fay, S. Baxter, C. H. Wessel, M. Eldib, J. Bini, S. D. Carlin, E. S. G. Stroes, G. Storm, A. Kjaer, J. S. Lewis, T. Reiner, Z. A. Fayad, W. J. M. Mulder and C. Pérez-Medina, *Bioconjug. Chem.*, **2020**, *31*, 360–368.

[6] S. Jeon, J. Kim, D. Lee, J. W. Baik and C. Kim, *Photoacoustics*, **2019**, *15*, 100141.

[7] K. Karrobi, A. Tank, S. Tabassum, V. Pera and D. Roblyer, *J. Biophotonics*, **2019**, *12*, 1–13.

[8] A. Y. Shih, J. D. Driscoll, P. J. Drew, N. Nishimura, C. B. Schaffer and D. Kleinfeld, *J. Cereb. Blood Flow Metab.*, **2012**, *32*, 1277–1309.

[9] A. Konno, N. Matsumoto, Y. Tomono and S. Okazaki, *Sci. Rep.*, **2020**, *10*, 1–15.

[10] H. Wan, J. Yue, S. Zhu, T. Uno, X. Zhang, Q. Yang, K. Yu, G. Hong, J. Wang, L. Li, Z. Ma, H. Gao, Y. Zhong, J. Su, A. L. Antaris, Y. Xia, J. Luo, Y. Liang and H. Dai, *Nat. Commun.*, **2018**, *9*, 1171.

[11] A. Klingberg, A. Hasenberg, I. Ludwig-Portugall, A. Medyukhina, L. Männ, A. Brenzel, D. R. Engel, M. T. Figge, C. Kurts and M. Gunzer, *J. Am. Soc. Nephrol.*, **2017**, *28*, 452–459.

[12] Y. Guo, H. Yuan, N. M. Claudio, S. Kura, N. Shakerdge, T. R. Mempel, B. J. Bacskai and L. Josephson, *PLoS One*, **2014**, *9*, e95406.

[13] D. Ding, C. C. Goh, G. Feng, Z. Zhao, J. Liu, R. Liu, N. Tomczak, J. Geng, B. Z. Tang, L. G. Ng and B. Liu, *Adv. Mater.*, **2013**, *25*, 6083–6088.

[14] D. J. Koo, J. Choi, M. Ahn, B. H. Ahn, D. H. Min and S. Y. Kim, *Bioconjug. Chem.*, **2020**, *31*, 1784–1794.

[15] S. H. Lee, Y. H. Choe, R. H. Kang, Y. R. Kim, N. H. Kim, S. Kang, Y. Kim, S. Park, Y. M. Hyun and D. Kim, *Bioorg. Chem.*, **2019**, *89*, 103019.

[16] M. R. Dreher, W. Liu, C. R. Michelich, M. W. Dewhirst, F. Yuan and A. Chilkoti, *J. Natl. Cancer Inst.*, **2006**, *98*, 335–344.

[17] J. K. Jung, I. Toma, A. Sipos, F. McCulloch and J. Peti-Peterdi, *Am. J. Physiol. - Ren. Physiol.*, **2006**, *291*, 495–502.

[18] R. T. Robertson, S. T. Levine, S. M. Haynes, P. Gutierrez, J. L. Baratta, Z. Tan and K. J. Longmuir, *Histochem. Cell Biol.*, **2015**, *143*, 225–234.

[19] C. Nguyen, S. Bascaramurty, B. Kuzio, L. Gregorash, V. Kupriyanov and O. Jilkina, *J. Biophotonics*, **2012**, *5*, 754–767.

[20] P. Baluk and D. M. McDonald, *Ann. N. Y. Acad. Sci.*, 2008, **1131**, 1–12.

[21] S. Tobita and T. Yoshihara, *Curr. Opin. Chem. Biol.*, **2016**, *33*, 39–45.

[22] T. Yoshihara, Y. Hirakawa, M. Nangaku and S. Tobita, Hydrophilic Ir(III) complexes for in vitro and in vivo oxygen imaging. In *RSC Detection Science: Quenched-Phosphorescence Detection of Molecular Oxygen: Applications in Life Sciences, Chap.4*, Royal Society of Chemistry, 2018, pp. 71–90.

[23] M. Yasukagawa, K. Yamada, S. Tobita and T. Yoshihara, *J. Photochem. Photobiol. A Chem.*, **2019**, *383*, 111983.

[24] I. Nakase, H. Hirose, G. Tanaka, A. Tadokoro, S. Kobayashi, T. Takeuchi and S. Futaki, *Mol. Ther.*, **2009**, *17*, 1868–1876.

[25] I. Nakase, Y. Konishi, M. Ueda, H. Saji and S. Futaki, *J. Control. Release*, **2012**, *159*, 181–188.

[26] K. Suzuki, A. Kobayashi, S. Kaneko, K. Takehira, T. Yoshihara, H. Ishida, Y. Shiina, S. Oishi and S. Tobita, *Phys. Chem. Chem. Phys.*, **2009**, *11*, 9850–9860.

[27] T. Yoshihara, S. Murayama, T. Masuda, T. Kikuchi, K. Yoshida, M. Hosaka and S. Tobita, *J. Photochem. Photobiol. A Chem.*, **2015**, *299*, 172–182.

[28] M. Matsumoto, N. Hada, Y. Sakamaki, A. Uno, T. Shiga, C. Tanaka, T. Ito, A. Katsume and M. Sudoh, *Int. J. Exp. Pathol.*, **2013**, *94*, 93–103.

[29] Y. Hirakawa, K. Mizukami, T. Yoshihara, I. Takahashi, P. Khulan, T. Honda, I. Mimura, T. Tanaka, S. Tobita and M. Nangaku, *Kidney Int.*, **2018**, *93*, 1483–1489.

[30] H. Yersin, *Highly Efficient OLEDs with Phosphorescent Matrerials*, Wiley-VCH, Weinheim, 2008.

[31] M. Montalti, A. Credi, L. Prodi and M. T. Gandolfi, *Handbook of Photochemistry*, CRC-Taylor & Francis, THIRD EDITION, 2006.

[32] T. Yoshihara, M. Hosaka, M. Terata, K. Ichikawa, S. Murayama, A. Tanaka, M. Mori, H. Itabashi, T. Takeuchi and S. Tobita, *Anal. Chem.*, **2015**, *87*, 2710–2717.

[33] S. Futaki, T. Suzuki, W. Ohashi, T. Yagami, S. Tanaka, K. Ueda and Y. Sugiura, *J. Biol. Chem.*, **2001**, *276*, 5836–5840.

[34] R. I. Dmitriev, H. M. Ropiak, G. V. Ponomarev, D. V. Yashunsky and D. B. Papkovsky, *Bioconjug. Chem.*, **2011**, *22*, 2507–2518.

[35] C. Dolan, R. D. Moriarty, E. Lestini, M. Devocelle, R. J. Forster and T. E. Keyes, *J. Inorg. Biochem.*, **2013**, *119*, 65–74.

[36] B. Wang, Y. Liang, H. Dong, T. Tan, B. Zhan, J. Cheng, K. K. W. Lo, Y. W. Lam and S. H. Cheng, *ChemBioChem*, **2012**, *13*, 2729–2737.

[37] S. W. Botchway, M. Charnley, J. W. Haycock, A. W. Parker, D. L. Rochester, J. A. Weinstein and J. A. G. Williams, *Proc. Natl. Acad. Sci. U. S. A.*, **2008**, *105*, 16071–16076.

[38] S. Coulon, F. Heindryckx, A. Geerts, C. Van Steenkiste, I. Colle and H. Van Vlierberghe, *Liver Int.*, **2011**, *31*, 146–162.

[39] D. H. Ipsen, J. Lykkesfeldt and P. Tveden-Nyborg, *Cell. Mol. Life Sci.*, **2018**, *75*, 3313–3327.

[40] H. Tilg and A. R. Moschen, *Hepatology*, **2010**, *52*, 1836–1846.

[41] C. P. Day and O. F. W. James, *Gastroenterology*, **1998**, *114*, 842–845.

[42] T. Yoshihara, R. Maruyama, S. Shiozaki, K. Yamamoto, S. Kato, Y. Nakamura and S. Tobita, *Anal. Chem.*, **2020**, *92*, 4996–5003.

Chapter 4

Summary

In this thesis, the phosphorescent probes based on Ir(III) complexes containing arginine peptides were synthesized and applied to sense and visualize intracellular oxygen levels and *in vivo* vascular network by using luminescence microscopic techniques. The present study can be summarized as follows:

In chapter 2, the ratiometric oxygen probes 7DEAC-R_8-BTQphen (**R8**) and 7DEAC-R_{12}-BTQphen (**R12**) with oligoarginine linker were designed and synthesized for intracellular oxygen sensing. The probes showed dual emission bands from fluorescent 7DEAC and phosphorescent BTQphen in solution, lipid membrane, and living cells. The photorelaxation processes of **R8** and **R12** in acetonitrile were evaluated by measurements of emission spectra, quantum yields, and lifetimes. The singlet-singlet energy transfer efficiencies (Φ_{SET}) were estimated to be 61% for **R8** and 45% for **R12**. The Φ_{SET} values decreased with an increase of the distance between 7DEAC and BTQphen chromophores, indicating that the energy transfer efficiency can be controlled by adjusting the length of the linker connecting two chromophores. The validities of oxygen concentrations derived from the ratiometric measurement using **R8** and **R12** were verified in solution and lipid membrane by phosphorescence lifetime measurements. The cellular uptake efficiencies of **R8** and **R12** were 5.5 and 7.2 times higher than that of C343-Pro_8-BTQphen with an oligoproline linker. It demonstrates that the introduction of the oligoarginine peptide can significantly enhance the cellular uptake efficiencies of the ratiometric probes. High cell penetration efficiencies of these probes allowed the use of intracellular oxygen sensing. The ratiometric measurements using **R12** enabled imaging of the oxygen gradient produced by placing coverslip onto a HeLa cell monolayer.

In chapter 3, Ir(III) complexes BTQ-R_n (n =4, 8, 12, 16) containing different lengths of arginine peptides were synthesized. The usefulness of these probes as a vascular

imaging probe was examined by comparing FITC (tomato) lectin, which has an affinity to vascular endothelium. It was revealed BTQ-R_n compounds (n = 8, 12, 16) selectively stain the vascular endothelial cells similar to FITC-lectin by luminescence microscope measurements of the renal cortex. These vasculature probes can be chemically synthesized, unlike fluorescent lectins or antibodies commonly used to stain blood vessels. The long phosphorescence lifetime allows visualization of the vascular structure without interferences from tissue autofluorescence using time-gated measurements. Furthermore, visualization of vascular networks in pathological tissues such as tumor was demonstrated using BTQ-R_{12}. Dual color imaging of hepatic tissues of living mice fed a high-fat diet using BTQ-R_{12} and the lipid droplet-specific probe PC6S revealed small and large lipid droplets in the hepatocytes, causing distortion of the sinusoidal structure. These results demonstrate that BTQ-R_{12} can be useful for imaging vascular structure in normal and pathological tissues *in vivo*.

Understanding the roles of molecular oxygen in living organisms requires further probe development. Therefore, as future works, it is desired to design suitable O_2 probes and carry out the ratiometric O_2 measurement in 3D cultured tissues and living organs. It would be effective to replacing the blue fluorophore of the ratiometric probes (in chapter 2) with a fluorophore that shows a long-wavelength emission and high brightness to overcome strong autofluorescence of tissue. Furthermore, improvement O_2 sensitivity of the probes is required for *in vivo* O_2 imaging. In chapter 3, the quantification of *in vivo* oxygen levels was challenging to perform because of the low oxygen sensitivity of this probe in vascular endothelium in contrast to solutions. It is considered the cause of that is a depression of the oxygen quenching by interaction with biological substances such as

proteins in tissue cells. Therefore, it is desired to reveal the probe localization in detail, whether in vascular endothelial cells or on the surface of endothelial cells.